

Effects of Therapeutic Concentrations of Tubulin-binding Drugs on Microtubule Dynamics

by

Seth Michael McCubbin

A dissertation submitted in partial fulfillment
of the requirements for the degree of
Doctor of Philosophy
(Biomedical Engineering)
in The University of Michigan
2016

Doctoral Committee:

Professor David S. Sept, Chair
Assistant Professor Ajit P. Joglekar
Professor Andrew J. Putnam
Professor Kristen J. Verhey

© Seth Michael McCubbin 2016

All Rights Reserved

To my father
and in memory of
my mother
and my Aunt Esther

ACKNOWLEDGEMENTS

I would like to express my sincere gratitude to the many people who have supported me and my work. First, I want to thank my late adviser, Alan Hunt, for his guidance and efforts in helping me to establish a compelling research project. I also want to thank my adviser, David Sept, who took me on as his student part way through my graduate career. His encouragement and endless optimism have motivated me to achieve more than I initially thought possible.

I want to thank former members of the Alan Hunt Lab, especially Blake Charlebois, whose patience and mentorship helped me to develop many of the skills necessary to conduct my research. I would also like to acknowledge my collaborators at the David Odde Lab at the University of Minnesota for all of their support and insightful discussions.

Finally, I thank my friends and family for all they have done to support me in this endeavor.

TABLE OF CONTENTS

DEDICATION	ii
ACKNOWLEDGEMENTS	iii
LIST OF FIGURES	vii
LIST OF TABLES	ix
ABSTRACT	x
CHAPTER	
I. Introduction	1
1.1 Mitosis	4
1.2 GTP-Cap Hypothesis	6
1.3 Growth models	9
1.3.1 Oosawa 1D Model	10
1.3.2 VanBuren et al. 2D Model	11
1.3.3 2D growth simulations by Gardner et al.	14
1.4 Microtubule-targeting drugs	17
1.4.1 Drug Toxicity, Resistance, and Synergy	21
1.5 Tubulin Structure and Interactions	24
1.5.1 The Taxoid Binding Site	26
1.5.2 The Peloruside/Laulimalide Binding Site	27
1.5.3 The Colchicine Binding Site	28
1.5.4 The Vinca Domain	29
II. Studies of Microtubule Growth in the Presence of the Chemotherapeutic Agent Paclitaxel	31
2.1 Effects of Paclitaxel on Microtubule Growth Determined Using DIC and TIRF Microscopy	31

2.1.1	Determination of Relevant Paclitaxel Concentrations Using DIC Microscopy	32
2.1.2	Resolution Improvements using TIRF Microscopy	38
2.2	Single-channel TIRF Microscope Design	47
2.3	Collection of Additional Growth Data Using Prepared Tubulin	51
2.4	Discussion	56
III.	Effects of Microtubule-targeting drugs on Microtubule Dynamics	58
3.1	Results	60
3.1.1	Microtubule Growth Rate Model	60
3.1.2	Colchicine and Vinblastine Stabilize Microtubules by Suppressing the Kinetic Rate Constants	65
3.1.3	Paclitaxel and Peloruside A Stabilize Microtubules without Altering the Kinetic Rates	69
3.1.4	Microtubule Protofilament Taper Lengths Are Gamma-distributed	72
3.1.5	Microtubule Rigidity	76
3.2	Discussion	79
IV.	Estimation of Flutax-2 Kinetics Using TIRF-FRAP	81
4.1	Total Internal Reflection Fluorescence Recovery After Photo-bleaching (TIR-FRAP)	83
4.2	Microtubule-Flutax-2 Exchange Kinetics	84
4.2.1	Methods	85
4.2.2	Results	87
4.3	TIR-FRAP Diffusion Model	88
4.4	Model and Experimental Results	91
4.4.1	Flutax Isodesmic Polymerization Model	93
4.4.2	Characterization of Flutax-2 Surface Binding	96
4.4.3	Expanded TIR-FRAP Diffusion and Surface Reaction Model	102
4.5	Future Studies of Microtubule-Flutax-2 Kinetics	106
V.	Materials and Methods	107
5.1	Materials	107
5.2	Buffer conditions	107
5.3	Tubulin purification	108
5.4	Tubulin labeling	108
5.5	GMPCPP-stabilized microtubule seeds	109
5.6	Experimental sample chambers	110
5.7	TIRF microscopy	110

5.8 Growth data analysis	111
VI. Conclusions and Future Work	113
BIBLIOGRAPHY	115

LIST OF FIGURES

Figure

1.1	Microtubule schematic	2
1.2	Dynamic instability diagram	3
1.3	Properties of microtubule growth	3
1.4	Phases of mitosis	5
1.5	Effects of paclitaxel on the mitotic spindle	6
1.6	Oosawa polymerization model	11
1.7	Illustration showing lateral interactions of tubulin dimers at the microtubule tip	12
1.8	Structure of paclitaxel	18
1.9	Structure of peloruside A	19
1.10	Structure of vinblastine	20
1.11	Structure of colchicine	21
1.12	Structure of tubulin	24
1.13	Tubulin drug binding sites	25
1.14	The paclitaxel binding site	26
1.15	The peloruside/laulimalide binding site	27
1.16	Peloruside/laulimalide intradimer interactions	28
1.17	The colchicine binding site	29
1.18	The vinca domain	30
2.1	Sample microtubule length traces and kymographs	43
2.2	Box plots of microtubule growth parameters	44
2.3	Images of tubulin SDS-PAGE gels	47
2.4	Single-color TIRF microscope design	50
2.5	Increment variance versus frame integration time	52
2.6	Sample microtubule length traces and kymographs from new data set	53
2.7	Box plots of microtubule growth parameters	55
3.1	Microtubule increment variance versus time interval	61
3.2	Microtubule growth rate model predictions	64
3.3	Sample length traces for microtubules grown with 7.5 μ M tubulin and various drugs	66
3.4	Effects of microtubule-targeting drugs on the tubulin on and off rates	68
3.5	Box plots of microtubule protofilament lengths	73

3.6	Estimates of gamma distribution step and scale parameters using microtubule tip structure data	75
3.7	Microtubule bending mode analysis coordinate system	77
4.1	Fluorescence recovery after photobleaching	83
4.2	TIR-FRAP experiment and analysis	86
4.3	TIR-FRAP microtubule and background recovery rates	88
4.4	TIR-FRAP model geometry	90
4.5	Observed TIR-FRAP recovery constants of Flutax-2 in buffer	92
4.6	Flutax-2 isodesmic model	95
4.7	Flutax-2 monomer fraction versus Flutax-2 concentration	97
4.8	Flutax surface interactions	99
4.9	Phalloidin-OG488 TIR-FRAP control experiment	100
4.10	Effects of cover slip treatment on flutax surface interactions	101
4.11	Effects of antifade concentration on Flutax-2 surface interactions	102
4.12	Proposed Flutax-2 surface binding and self-quenching diagram	103
4.13	TIR-FRAP simulations with surface interactions and fluorophore self-quenching	105

LIST OF TABLES

Table

2.1	Microtubule growth parameters	46
2.2	Microtubule growth parameters using HiLyte 488 tubulin, labeled in-lab	54
3.1	Growth Model Parameters	63
3.2	Model estimates of microtubule growth parameters	68
3.3	Microtubule growth parameters estimated from increment variance .	71

ABSTRACT

Effects of Therapeutic Concentrations of Tubulin-binding Drugs on Microtubule Dynamics

by

Seth McCubbin

Chair: David Sept

Microtubules are dynamic structures that are formed by the polymerization of $\alpha\beta$ -tubulin heterodimers into long, hollow tubes. They mediate a number of critical processes, including mitosis, intracellular transport, and cell migration. During mitosis, microtubules form into a complex structure known as the spindle apparatus, which orchestrates the segregation of chromosomes into daughter cells. This process depends on an intrinsic feature of microtubules called dynamic instability, where microtubules abruptly switch between phases of sustained growth and rapid shortening. This allows microtubules to quickly probe the intracellular volume to locate and couple to chromosomes before synchronous division. Any aberrant function of this delicate process, if not detected and resolved by a mitotic spindle checkpoint, can lead to aneuploidy and tumorigenesis.

Microtubule-targeting drugs are commonly used as chemotherapeutic agents, given their ability to disrupt native microtubule dynamics, which prevents cell division. These drugs have been used to successfully treat a range of cancers; however, their use is associated with a number of debilitating side effects, and in some cases, acquired

drug resistance. The detailed mechanisms of action of microtubule-binding drugs are not well understood, and therefore, the development of efficacious drugs with lower collateral toxicity is slow.

In this work I investigated the effects of four microtubule-binding drugs, which each target distinct sites on the tubulin subunit. First, I adapted previously established methods to determine how the kinetic rates of tubulin exchange from microtubules are affected by microtubule-binding drugs. I found that the drugs colchicine and vinblastine potently suppress the kinetic rates, while paclitaxel and peloruside A have little effect, even though they are able to completely suppress dynamic instability. Furthermore, I related these effects to changes in the microtubule tip structure and explored methods for measuring changes in microtubule rigidity. Finally, experimental data and modeling show that the fluorescent paclitaxel-site probe Flutax-2 undergoes surface interactions, which can lead to non-monotonic self-quenching effects. Moreover, Flutax-2 aggregates in solution, leading to a substantial reduction in the monomeric, microtubule-binding form.

CHAPTER I

Introduction

Microtubules are rigid, filamentous polymers that play a critical role in many cellular processes, including mitosis, intracellular transport, and cell motility. They adopt structural configurations within cells that can rapidly change in order to fill these roles (*Desai and Mitchison, 1997*). Microtubules are formed by the polymerization of $\alpha\beta$ tubulin dimers into long, hollow tubes. Tubulin dimers bind head-to-tail to create protofilaments, 13 of which associate laterally to form a microtubule. Once a critical mass of tubulin dimers associate, a microtubule is nucleated, and it can elongate via binding of additional tubulin dimers. The asymmetric organization of tubulin dimers results in a structural polarity, with fast microtubule growth occurring at the microtubule plus end, where β subunits are exposed (Figure 1.1).

Both the α - and β -tubulin subunits bind GTP, which is permanently locked inside the α -tubulin subunit, but can be hydrolyzed and exchanged in β -tubulin. Generally, only dimers with a β -tubulin subunit bound with GTP can polymerize into a microtubule, since, when bound with GTP the dimer maintains a relatively straight conformation that facilitates polymerization (hereinafter GTP- and GDP-tubulin will refer to the nucleotide state of the β subunit). Sometime after incorporation of a dimer into the polymer, tubulin's intrinsic GTPase activity hydrolyses GTP to GDP. This event is thought to change the preferred conformation of the dimer from straight to

kinked; however, often by this point the growing microtubule has been capped with additional GTP-tubulin dimers. Thus, according to current models of microtubule growth (see Figure 1.2), the GDP-tubulin dimers are locked in a straight conformation by the surrounding microtubule lattice and GTP-tubulin cap, and energy is stored in the polymer as mechanical strain (*Erickson and O'Brien, 1992*).

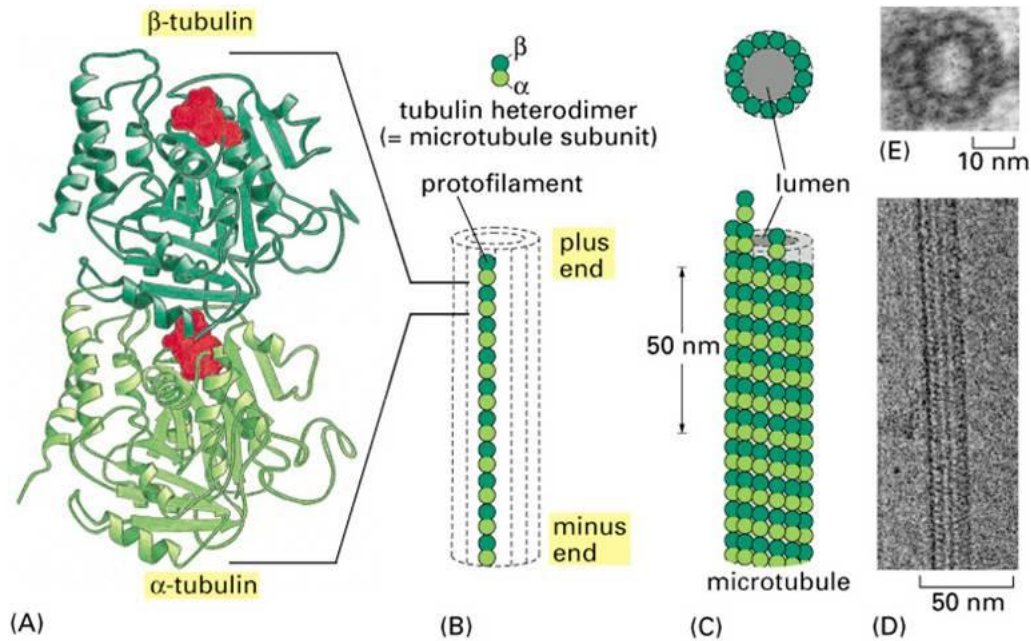


Figure 16–6. Molecular Biology of the Cell, 4th Edition.

Figure 1.1: Microtubule schematic. Protofilaments are assembled from chains of $\alpha\beta$ -tubulin subunits, which are associated laterally to form microtubules (*Bruce Alberts and Walter, 2002*).

In instances where GTP hydrolysis outpaces addition of GTP dimers at the end of the microtubule, the GDP-tubulin core is exposed, and strain energy is released, causing the protofilaments curl outward from the microtubule axis. These events lead to rapid disassembly of the microtubule. The transition to disassembly is known as a catastrophe, and recovery of growth is termed a rescue. The stochastic switching between extended periods of slow growth and rapid shortening is known as dynamic instability (see Figure 1.3), and it is an important functional characteristic of microtubule dynamics (*Mitchison and Kirschner, 1984*).

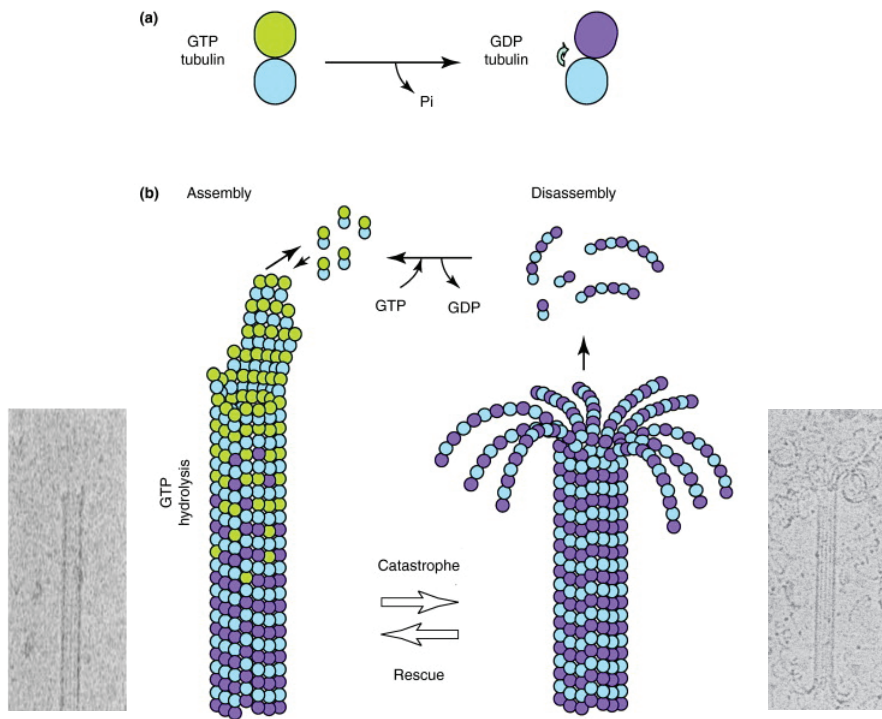


Figure 1.2: Dynamic instability diagram. (a) Tubulin subunits bind GTP, which can be hydrolyzed to GDP after incorporation of the subunit into a microtubule. Tubulin bound to GTP has a relatively straight conformation, while GDP-tubulin is slightly bent. (b) A GTP-tubulin “cap” is thought to stabilize assembled subunits that have already hydrolyzed their bound nucleotides. Loss of this cap exposes the labile GDP-tubulin core, which leads to disassembly (*Al-Bassam and Chang, 2011*). Cryo-EM images from *Mandelkow et al. (1991)*.

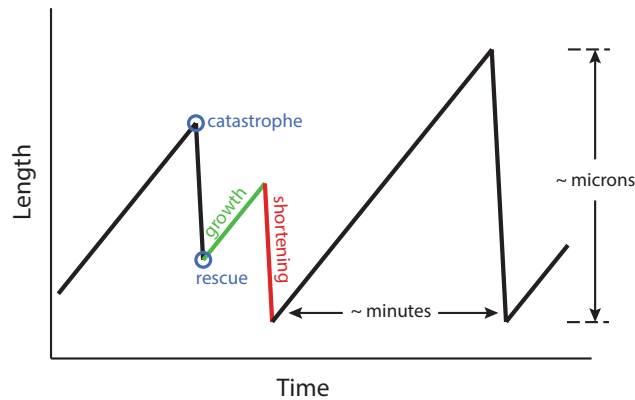


Figure 1.3: Properties of microtubule growth. Microtubules switch between phases of slow growth and rapid shortening. A transition from growth to shortening is called a “catastrophe”, and a transition back to growth is called a “rescue”.

1.1 Mitosis

In the cell, precise control of microtubule dynamics is necessary for creating cytoskeletal structures that support cellular processes. During mitosis (Figure 1.4), a cell's genetic material is duplicated with perfect fidelity as pairs of sister chromatids, which are segregated into daughter cells. This process is orchestrated by the mitotic spindle apparatus, a structure comprising microtubules, centrosomes, kinetochores, and other microtubule-associated proteins. During interphase microtubule dynamics are relatively slow but increase up to 100-fold during mitosis (*Mollinedo and Gajate, 2003*). At the start of mitosis, microtubules prepare for a complete remodeling of the cell by undergoing rapid disassembly, followed by growth in large numbers from the centrosomes, which are located at opposite ends of the cell. The highly dynamic microtubules undergo phases of growth and shortening as they probe the intracellular space to locate and mechanically couple to chromosome-linked kinetochores. Since growing microtubule ends are not able to directly target diffusing kinetochores, they must go through repeated rounds of polymerization and depolymerization until one is eventually found. Once bound, the associated microtubules become stabilized, and other microtubules emanating from the opposite side of the cell eventually bind the kinetochore on the opposing side of the same chromosome. After a chromosome becomes simultaneously attached to microtubules from both sides of the cell, forces exerted by the spindle system tug it and the other chromosomes to the spindle equator, which is equidistant from the spindle poles. In vertebrate cells, chromosomes at the spindle equator oscillate back and forth, awaiting the mitotic checkpoint, which directs the system to pull the sister chromatids toward their respective poles before completing the final phase of cell division (*Cooper Geoffrey, 2000; Bruce Alberts and Walter, 2002*).

Mitosis is an extremely delicate, highly-regulated process, and therefore, any aberrant function in the spindle mechanism can cause the cell to halt division. The spindle

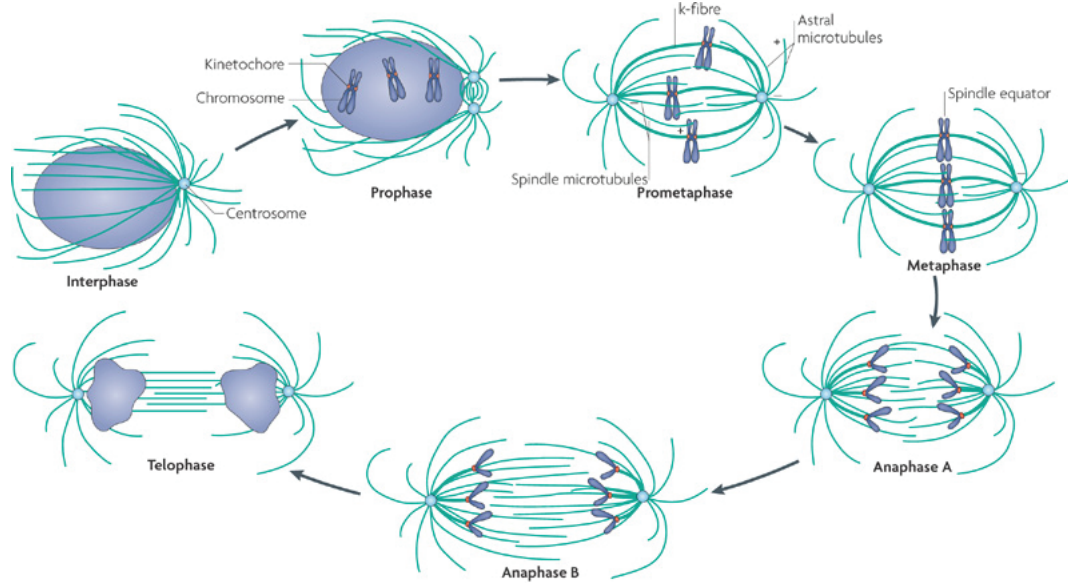


Figure 1.4: Phases of mitosis (*Walczak et al., 2010*).

assembly checkpoint monitors the spindle structure to ensure bivalent chromosome attachment to microtubules. Defects in the system are detected by the kinetochores (among other protein groups), which, while unattached release messenger chemicals to delay cell cycle progression. Mutations in the spindle assembly checkpoint that cause premature initiation of chromosome segregation can lead to aneuploidy and subsequently, tumorigenesis. A properly functioning checkpoint system, however, will sense prolonged spindle malfunction and signal the cell to exit mitosis and initiate apoptosis.

Antimitotic drugs, which suppress dynamic instability, can alter spindle morphology in a number of ways, for example, by creating mono- or multipolar spindles, as seen in Figure 1.5. The mitotic spindle apparatus is highly sensitive to such defects and will block cells from completing mitosis (*May and Hardwick, 2006*).

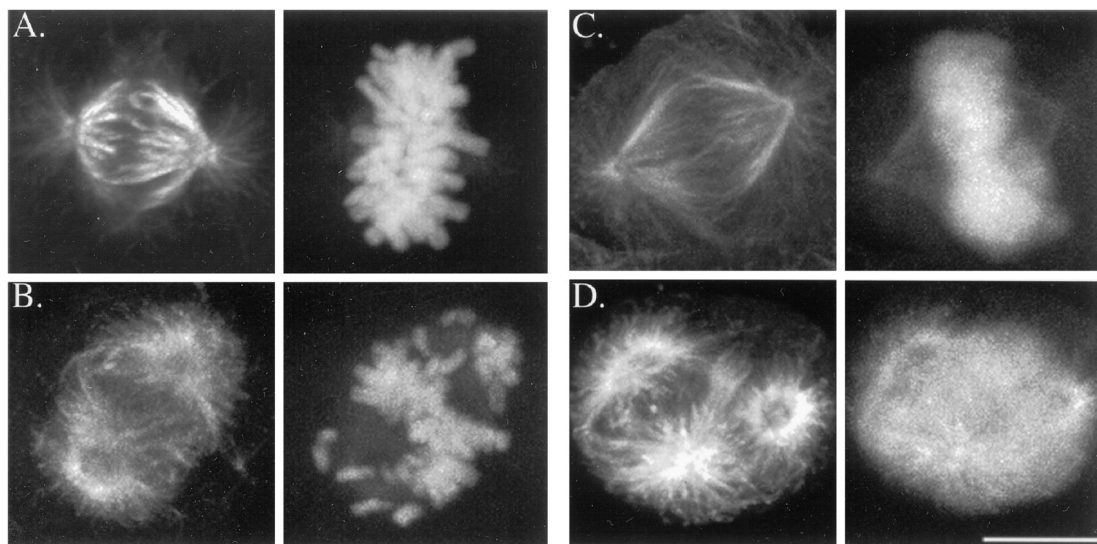


Figure 1.5: Effects of paclitaxel on the mitotic spindle. Microtubules undergoing mitosis in A-498 kidney cells (A, B) and Caov-3 ovary cells (C, D). The top and bottom rows show cells in the absence or presence of paclitaxel, respectively. Images from *Yvon et al.* (1999).

1.2 GTP-Cap Hypothesis

While the mechanistic details of dynamic instability are unknown, the GTP-cap hypothesis has become the predominant theory used to explain this phenomenon. Dynamic instability is thought to depend on a stabilizing “GTP-cap” (Figure 1.2). This hypothesis is based on the observation of curved protofilaments at the ends of shrinking microtubules as well as curled tubulin oligomers in nearby solution (*Chrétien et al.*, 1995; *Mandelkow et al.*, 1991). Once the GTP-cap is lost, either by hydrolysis or dissociation, the exposed core of GDP-tubulin subunits assume their preferred, curved conformation, leading to outward curling of the protofilaments as lateral interactions between protofilaments are lost. Consistent with this theory, studies have shown that by replacing GTP with the non-hydrolyzable analogue GMPCPP, microtubules no longer undergo rapid shortening (*Hyman et al.*, 1992, 1995). However, the GTP-cap theory is complicated by results from microtubule severing experiments, where long microtubules were cut at their midsection by an ultraviolet beam (*Walker*

et al., 1989) or by a glass needle (*Tran et al.*, 1997). The conventional GTP-cap hypothesis would predict rapid shortening of the newly created plus and minus ends; however, experimentally it was found that while the new plus ends rapidly shortened, the new minus ends tended to grow (*Odde et al.*, 1995).

The GTP-cap size has been estimated experimentally using various techniques. *Voter et al.* (1991) and *Walker et al.* (1991) each performed tubulin dilution experiments and measured the lag time between dilution and the onset of rapid disassembly. Using previous estimates of tubulin hydrolysis and kinetic dissociation rates, they correlated the lag time to the number of dimers comprising the GTP-cap. *Voter et al.* (1991) and *Walker et al.* (1991) estimated plus end cap sizes of < 40 and ≤ 200 subunits, respectively. Their kinetic rate estimates, however, were based on the Oosawa 1D polymerization model (*Oosawa*, 1970; *Walker et al.*, 1988), which does not accurately predict the kinetic rates of multi-filament polymers (*Gardner et al.*, 2011a).

Drechsel and Kirschner (1994) estimated the minimum cap size necessary to stabilize microtubules using a GMPCPP cap assay. First, they grew dim fluorescein extensions off of bright fluorescein seeds. They then diluted the microtubules into $1 \mu\text{M}$ GMPCPP rhodamine-labeled tubulin and collected samples at various time points. Microtubule samples were diluted into buffer for 3 minutes and then fixed. The cap sizes were estimated using calibrated intensity measurements to examine microtubules that were able to survive short dilution times. They concluded that a minimum of 40 GTP-tubulin subunits are necessary to stabilize microtubules against dilution.

The GTP-cap size has also been estimated *in vivo* using the plus-end tip tracker EB1, which detects the nucleotide state of tubulin (*Zanic et al.*, 2009; *Maurer et al.*, 2012). *Seetapun et al.* (2012) measured the number of fluorescent EB1 dimers bound to the growing microtubule plus ends and estimated a GTP-cap size of ~ 750 tubulin

subunits. The authors speculated that the disparity between *in vitro* and *in vivo* estimates is explained, in some cases, by differences in growth rates of *in vivo* and *in vitro* microtubules; however, they also believed that estimates of very small cap sizes (≤ 40 subunits) were inaccurate (*Caplow and Shanks, 1996*).

Finally, in recent work researchers selected a recombinant antibody (hMB11) that recognizes GTP-tubulin (*Dimitrov et al., 2008*). They used immunofluorescence to show that the antibody binds to the ends of growing microtubules *in vivo*, indicating the presence of a GTP-tubulin cap. They also found that hMB11 stained entire microtubules when they were grown in the presence of the non-hydrolyzable GTP analog GMPCPP. While the actual GTP-tubulin cap size was not estimated, this work has established an alternative method for doing so.

Many models have been developed to describe the GTP-cap and its relation to dynamic instability. Early models were typically based on the assumption of independent protofilament growth, where lateral interactions between adjacent protofilaments were assumed to negligibly effect hydrolysis rates. *Coupled hydrolysis* is an early single-protofilament model where hydrolysis of a GTP-subunit occurs after another dimer binds above it. This means that the GTP-cap is always a single layer deep and that catastrophe can only occur by dissociation of end GTP-subunits. A second model is *vectorial hydrolysis* where hydrolysis can only occur in GTP-tubulin subunits that are in contact with GDP-tubulin. A third is *random hydrolysis* where each GTP-tubulin dimer in the microtubule has the same probability of undergoing hydrolysis. Each of these models has variants, and there also exist mixed hydrolysis models, which combine the assumptions of previously defined models. While each of these models is able to predict experimentally observed GTP-cap sizes for a subset of growth conditions, none is robust enough to accurately describe GTP-cap size and other microtubule growth parameters over a wide range of tubulin concentrations (*Walker et al., 1988; Bowne-Anderson et al., 2013*).

Multiple-protofilament models consider interactions between protofilaments such that the binding or hydrolysis of one subunit can affect binding or hydrolysis of another subunit located in a different protofilament. Notably, *VanBuren et al.* (2002) developed a microtubule growth model which incorporated lateral and longitudinal bond energies to estimate the subunit on and off rates. Hydrolysis was considered using a coupled-random mixed hydrolysis model, where hydrolysis occurred randomly within the lattice, but could not occur at the end dimers of each protofilament. Their model predicted experimentally determined GTP-cap sizes of ~ 55 subunits over a range of tubulin concentrations, as determined by dilution experiments (*Voter et al.*, 1991; *Walker et al.*, 1991; *Drechsel and Kirschner*, 1994); however, microtubule growth lifetimes followed a steeper dependence on GTP-tubulin compared to experimental data.

Recently, *Bowne-Anderson et al.* (2013) developed a multiple-protofilament coupled-random hydrolysis model based on work by *Gardner et al.* (2011b), who found that microtubule growth lifetimes can be modeled by the accrual of permanent destabilizing events. These events were not explicitly defined but could be individual defects in that lattice structure, or permanent loss of the GTP-cap on a given protofilament (e.g. where subsequent additions of GTP-tubulin are unstable or undergo immediate hydrolysis). They assumed that each protofilament could only destabilize once, and destabilization of 3 out of 13 protofilaments would cause a catastrophe. Because their model defined both a stabilizing cap and a GTP-cap, the former of which was only two subunits deep, direct comparisons with experimental values cannot be made.

1.3 Growth models

Microtubule kinetic models have long been used to understand how experimental parameters, such as tubulin concentration and drug conditions, affect various microtubule growth parameters, including the growth and shortening rates, and catas-

trophe and rescue frequencies. As our understanding of microtubule dynamics has improved, models have evolved from those using simple, linear systems based on first order kinetics to more comprehensive versions, which include the multidimensional interactions between individual tubulin dimers. A robust model is necessary for interpreting experimental observations—which are limited in resolution—and also in making predictions to guide future experiments.

1.3.1 Oosawa 1D Model

The classic 1D polymerization model by *Oosawa* (1970) describes the elongation rate of a linear polymer, which grows by the addition or loss of individual subunits. Assuming no spontaneous nucleation and no mass action effects (i.e. low concentration of nuclei relative to monomer) Oosawa showed that:

$$-\frac{dc_1}{dt} = \frac{dc_p}{dt} = k_+c_1 - k_- \quad (1.1)$$

where c_1 is the monomer concentration, c_p is the polymer concentration, and k_+ and k_- are the kinetic constants for binding and unbinding of the monomer to and from the end of the polymer, respectively. Here the association rate is proportional to the monomer concentration and the dissociation rate is constant. Adapting this model to describe length changes of a single microtubule protofilament:

$$v_{g,PF} = \alpha_{PF} (k_{on,PF} [\text{tubulin}] - k_{off,PF}) \quad (1.2)$$

where $v_{g,PF}$ is the growth rate of each protofilament in nm/s, $\alpha_{PF} = 8$ nm is the length of a tubulin dimer, $[\text{tubulin}]$ is the concentration of free tubulin dimers, and $k_{on,PF}$ and $k_{off,PF}$ are the kinetic association and dissociation rates for each protofilament, respectively. Because all addition and loss events are assumed to be kinetically equivalent, a similar equation can be written for the growth rate of a multiprotofilament

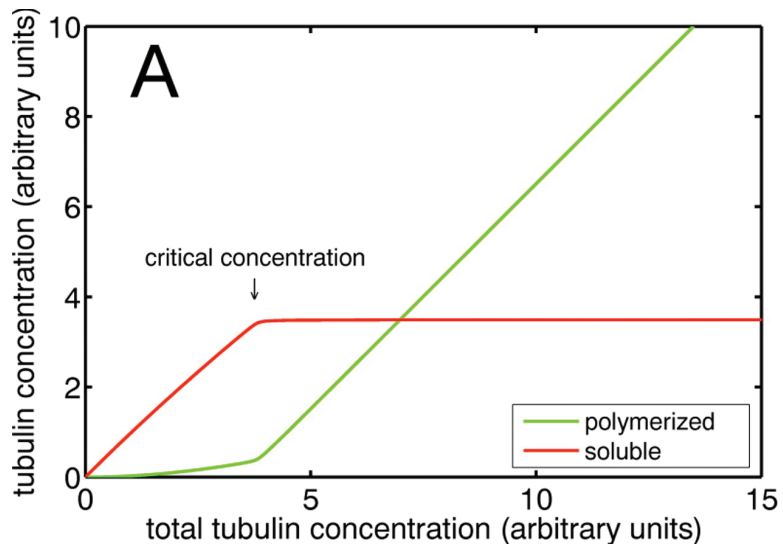


Figure 1.6: Oosawa polymerization model. Nucleation and growth of microtubules do not occur until a critical concentration ($[C_c]$) is reached, where the on rate of tubulin is equal to the off rate (*Oosawa*, 1970). In this illustrative plot (*Gregoretti et al.*, 2006), the soluble tubulin concentration is assumed to be much greater than the number of nucleated microtubules, such that all soluble tubulin in excess of C_c is incorporated into polymer.

microtubule:

$$v_{g,MT} = \alpha_{MT} (k_{on,MT} [\text{tubulin}] - k_{off,MT}) \quad (1.3)$$

where $\alpha_{MT} = \frac{8\text{nm}}{13}$ is the average length change resulting from the addition of a single tubulin dimer to a 13-protofilament microtubule. Figure 1.6 shows the expected behavior of the model described by Equation 1.3. Because $k_{off,MT}$ is constant, nucleation and growth will not occur until a critical concentration ($[C_c]$) is reached, where $k_{on,MT} [C_c] = k_{off,MT}$.

By fitting experimental data to Equation 1.3, the resulting slope and intercept values will yield $k_{on,MT}$ and $k_{off,MT}$, respectively.

1.3.2 VanBuren et al. 2D Model

The 1D model predicts a constant tubulin off rate, and therefore, when applied to multifilament polymers, such as microtubules, it assumes that the association and

dissociation rates are equal for all protofilaments. This means that lateral bond energies are considered negligible, yet the rigid microtubule structure necessitates an appreciable amount of lateral energy to prevent individual protofilaments from dissociating from one another. Hill theorized that multi-stranded polymers have rate constants that vary across filaments, that depend not only on the monomer concentration, but also on polymer end structure (*Hill*, 1987). That is, there is a change over time in the number of lateral neighbors interacting with subunits at the polymer end, leading to fluctuating rate constants (see Figure 1.7).

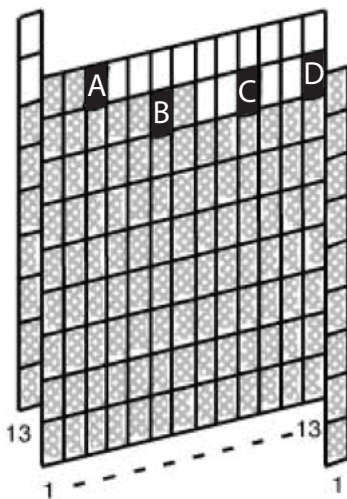


Figure 1.7: Illustration showing lateral interactions of tubulin dimers at the microtubule tip. In this diagram of an unrolled microtubule, end dimers each have a single longitudinal interaction with dimers below them, but can be stabilized by varying degrees of lateral interaction. Dimers A, B, C, and D are laterally stabilized by 1, 2, 0, and $\frac{1}{2}$ dimers, respectively, which, as hypothesized by *Hill* (1987) can lead to tubulin off rates that differ across protofilaments. Image from *VanBuren et al.* (2002).

VanBuren et al. (2002) developed a model of microtubule assembly that considered both lateral and longitudinal tubulin interactions. Using previously published association and net growth rate estimates, they ran Monte Carlo simulations of 13-protofilament microtubules over a range of tubulin concentrations to screen for probable values of lateral (ΔG_{Lat}) and longitudinal (ΔG_{Long}) bond energies. In their model the longitudinal bond energy included the entropic cost of dimer immobiliza-

tion (ΔG_S) and is denoted as ΔG_{Long}^* ($\Delta G_{Long}^* = \Delta G_{Long} + \Delta G_S$). For each time step in the simulation they considered:

1. one possible association event to each protofilament end
2. one possible dissociation event for each dimer in the lattice
3. possible hydrolysis of each unhydrolyzed (GTP-tubulin) dimer below the end-most dimer of every protofilament, using an assigned hydrolysis rate constant

The association rates for each protofilament were set to be equal and remain constant. This value was assigned as $k_+ = 4 \mu\text{M}^{-1}\text{s}^{-1}$ using previous experimental estimates by others (*Erickson, 1989; Bayley et al., 1990; Martin et al., 1993*). For dissociation events, if a buried dimer dissociated, then all above dimers in the same protofilament also dissociated. The change in energy for a dissociation event is then the sum of energies for all of the above lateral bonds (ΔG_{Lat}) plus ΔG_{Lat} and ΔG_{Long}^* for the dimer under consideration. The dissociation rate was computed using the above sum (ΔG) and equation (1.4), where k_B is Boltzmann's constant, T is the temperature of the reaction (K), and k_+ and k_- are the association and dissociation rates, respectively.

$$\Delta G = -k_B T \ln \left(\frac{k_+}{k_-} [\text{GTP-tubulin}] \right) \quad (1.4)$$

For each iteration an execution time was calculated for each of the possible events using equation (1.5):

$$t_i = \frac{-\ln(R_i)}{k_i} \quad (1.5)$$

where t is the execution time, i is the index of each possible event, k is the rate constant of the event, and R is a uniformly distributed random number from 0 to 1. The event with the shortest execution time was chosen and implemented before starting the next iteration.

VanBuren et al. plotted contour lines of bond energies at experimentally observed growth rates. Doing so over a range of tubulin concentrations allowed them to determine a single pair of ΔG_{Lat} and ΔG_{Long}^* values. The model predicted a lateral bond energy of -3.2 to $-5.7 k_B T$ and a longitudinal bond energy of -18.5 to $-27.8 k_B T$, after subtracting estimates of ΔG_S by *Erickson* (1989). With these parameters the model was able to reproduce growth and shortening rates as well as catastrophe and rescue frequencies, over a range of tubulin concentrations.

1.3.3 2D growth simulations by Gardner et al.

Gardner et al. (2011a) used high resolution experimental data to make comparisons of the 1D and 2D growth models. The 1D model predicts a subunit on-rate that scales with the free tubulin concentration ($k_{on}^* = k_{on} [\text{tubulin}]$; where k_{on}^* is the subunit on-rate and k_{on} is the association rate constant) and a constant off-rate (k_{off}). The net length change ΔL over time Δt is then $\Delta L = k_{on} [\text{tubulin}] - k_{off}$. This indicates that for increasing tubulin concentrations the probability of large shortening events should decrease because the on-rate increases while the off-rate remains constant.

To test this experimentally, *Gardner et al.* used total internal reflection fluorescence (TIRF) microscopy to image microtubules grown with GMPCPP-tubulin. GMPCPP is a non-hydrolyzable GTP analog that was used to eliminate potentially confounding hydrolysis effects. They analyzed shortening events of < -32 nm (approximately 4 subunit lengths) and found that higher free tubulin concentrations resulted in an increase in the frequency of those shortening events, suggesting that the subunit off-rate increases with [GMPCPP-tubulin]. These measurements were repeated at higher resolution using laser tweezers (spatiotemporal resolution of < 3.5 nm and 10 Hz) to analyze length changes of < -8 nm. After ruling out the possibility of oligomer addition (*Kerssemakers et al.*, 2006) they concluded that increased

[GMPCPP-tubulin] led to an increase in the frequency of shortening events, which is inconsistent with the 1D model.

Next, Gardner et al. sought to determine whether an increased dissociation rate at higher tubulin concentrations was linked to a less stable microtubule tip configuration. Using the 2D model, which accounts for lateral subunit interactions, and thus variable off-rates, they predicted higher off-rates with increasing [tubulin]. Furthermore, the model showed that net microtubule assembly resulted from large, competitive on- and off- rates, which both increased with higher [tubulin]. They hypothesized that this was caused by a shift toward less stable tip configurations, where end subunits are, on average, stabilized by fewer lateral neighbors. Given this premise, the average dissociation rate for the entire microtubule tip can be calculated by

$$k_{off,MT} \approx f_2 k_{off,PF}^{(2)} + f_1 k_{off,PF}^{(1)} + f_0 k_{off,PF}^{(0)} \quad (1.6)$$

where f_2 , f_1 , and f_0 are the probabilities of tip subunits with two, one, and zero lateral neighbors, respectively, and $k_{off,PF}^{(2)}$, $k_{off,PF}^{(1)}$, $k_{off,PF}^{(0)}$ are the respective dissociation rate constants. Analysis of the 2D simulation results showed that for increasing [tubulin], zero-neighbor subunits remained approximately constant, single-neighbor subunits increased, and two-neighbor subunits decreased. These results indicate a shift toward a less stable tip structure at higher tubulin concentrations, and a tubulin off-rate that is indirectly dependent on the on-rate.

Both the 1D and 2D models as well as numerous *in vitro* studies predict a linear relationship between the microtubule net growth rate and tubulin concentration. However, the 2D model predicts an association rate constant of approximately $52 \mu\text{M}^{-1}\text{s}^{-1}$, which is an order of magnitude higher than that predicted by the 1D model. This higher value is in agreement with theoretical values obtained from previous diffusion-limited protein interaction studies (*Northrup and Erickson, 1992; Pollard,*

1986).

To compare the 2D model results with experimentally obtained rate constants *Gardner et al.* fit experimental growth increment data using a diffusion-with-drift model, described by the following equation

$$\langle \Delta L^2 \rangle = v_g^2 \Delta t^2 + 2D_p \Delta t + \sigma^2 \quad (1.7)$$

where ΔL is the microtubule length change over a time step Δt , v_g is the net growth rate, σ^2 is the experimental measurement noise, and D_p is the effective diffusion coefficient, which captures the underlying rates of subunit addition and loss. They fit experimental data and data generated from both models to Equation 1.7 and found similar values of D_p for the experimental and 2D model data. However, D_p from the 1D model was an order of magnitude lower, indicating that experimentally-observed microtubule growth variability is consistent with the 2D model but not the 1D model.

The subunit on ($k_{on,MT}^*$) and off ($k_{off,MT}$) rates were then estimated by relating the mean squared growth increments due to diffusion

$$\langle \Delta l_D^2 \rangle = 2D_p \Delta t \quad (1.8)$$

with the growth rate variance due to diffusion (*Oosawa, 1970; Skellam, 1945*),

$$\langle \Delta l_D^2 \rangle = \alpha_{MT}^2 (k_{on,MT} [\text{tubulin}] + k_{off,MT}) \Delta t \quad (1.9)$$

and Equation 1.3. Combining the above equations for a given tubulin concentration yields estimates of $k_{on,MT}^*$ and $k_{off,MT}$

$$k_{on,MT}^* = \frac{D_p}{\alpha_{MT}^2} + \frac{v_g}{2\alpha_{MT}} \quad (1.10)$$

$$k_{off,MT} = \frac{D_p}{\alpha_{MT}^2} - \frac{v_g}{2 \alpha_{MT}} \quad (1.11)$$

Kinetic rates were found to be similar to those predicted by the 2D model (at 1.5 μM tubulin $k_{on}^* \approx 77 \text{ s}^{-1}$ and $k_{off} \approx 75 \text{ s}^{-1}$).

Finally, *Gardner et al.* estimated the microtubule tip taper lengths at different tubulin concentrations. This was done by fitting the error function along the microtubule axis at the tip. The drop in fluorescence intensity from the microtubule to the background yields the tip position as well as the standard deviation of protofilament lengths, σ_{tip} . Relatively small values of σ_{tip} indicate a “blunt” microtubule with protofilaments that are approximately equal in length, while tips with a large σ_{tip} have more tapered protofilaments. They found that microtubule tips become more tapered at higher tubulin concentrations, in agreement with previous work (*Chrétien et al.*, 1995).

1.4 Microtubule-targeting drugs

Microtubule-targeting drugs are a class of drugs that inhibit microtubule dynamics. Many of these drugs are naturally occurring toxins isolated from marine and botanical sources (*Amador et al.*, 2003), and were likely evolved as defense mechanisms. Microtubules are an effective target for these toxins, since (1) tubulin is highly conserved and found in all eukaryotic cells, and (2) microtubules play a vital role in cell division and migration.

At high concentrations microtubule-targeting drugs can promote either microtubule assembly or disassembly, allowing particular drugs to be classified as microtubule stabilizers or destabilizers, respectively. At lower, clinically-relevant concentrations, the effects of these drugs are more subtle; their effect on equilibrium polymer mass becomes negligible, and their activities tend to converge toward microtubule ki-

netic stabilization, where the rates of subunit addition and loss are heavily suppressed (Derry *et al.*, 1995; Jordan and Wilson, 2004; Dumontet and Jordan, 2010). Such an effect makes these agents particularly useful as chemotherapy drugs, since disruption of normal microtubule function leads to improper chromosome attachment during mitosis. This causes delays in the cell cycle, which activates programmed cell death.

Microtubule-targeting drugs have been used clinically for many decades, and while it has been known that they target microtubules, we still have a poor understanding of exactly *how* they affect microtubule dynamics. A thorough knowledge of their mechanisms of action is critical in the development of novel drugs that are better tolerated by patients. A first step is to understand how these drugs affect microtubule dynamics *in vitro* before studying their function in the context of the vastly more complex cell.

Paclitaxel

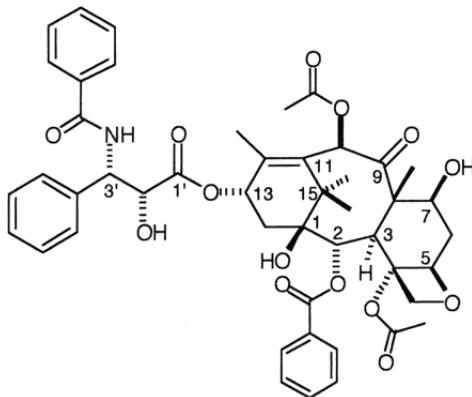


Figure 1.8: Structure of paclitaxel. Image from *Gupta et al.* (2003).

Paclitaxel is a microtubule-binding drug isolated from the Pacific yew tree and is used to treat lung, ovarian, and breast cancers (Rowinsky *et al.*, 1992). It binds polymerized tubulin with high affinity ($K_D = 10^{-7}$ M, Buey *et al.* (2004)) at the taxoid binding site located in β -tubulin on the inner surface of the microtubule; however, it binds poorly to soluble tubulin. At the time of its discovery, paclitaxel was

unique in that it was found to stabilize microtubules at higher concentrations, whereas previously used chemotherapy drugs (e.g. vinca alkaloids) destabilized microtubules. Although many studies have used micromolar concentrations of the drug, investigators have found that concentrations as low as 1 nM are sufficient to arrest cells at the metaphase-anaphase transition. Typical therapeutic concentrations of 5 - 200 nM have been reported to cause mitotic arrest and eventual cell death *in vivo* (Jordan *et al.*, 1996; Torres and Horwitz, 1998; Blagosklonny and Fojo, 1999).

Peloruside A

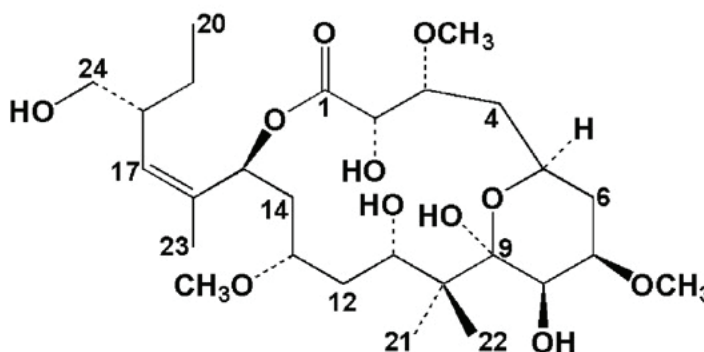


Figure 1.9: Structure of peloruside A. Image from *Hamel et al.* (2006).

Peloruside A is another microtubule stabilizer with properties similar to those of paclitaxel (Ganguly *et al.*, 2015; Begaye *et al.*, 2011). Isolated from New Zealand marine sponges, it binds tubulin at a site distinct from the taxoid binding site. Peloruside A is a relatively new discovery but shows great promise in clinical use. Compared to paclitaxel, it is more soluble in plasma, allowing for easier delivery (Hood *et al.*, 2002; Miller *et al.*, 2010), and it retains its efficacy in some cells resistant to paclitaxel, in part because of its low affinity for the P-glycoprotein drug efflux pump (Kanakkanthara *et al.*, 2011; Borst and Elferink, 2002). In addition, peloruside A has been shown to synergize with other microtubule-binding drugs (Wilmes *et al.*,

2007, 2011; *Clark et al.*, 2006; *Gapud et al.*, 2004), potentially allowing it to be used in combination with other drugs at doses below the threshold of side effect toxicity.

Vinblastine

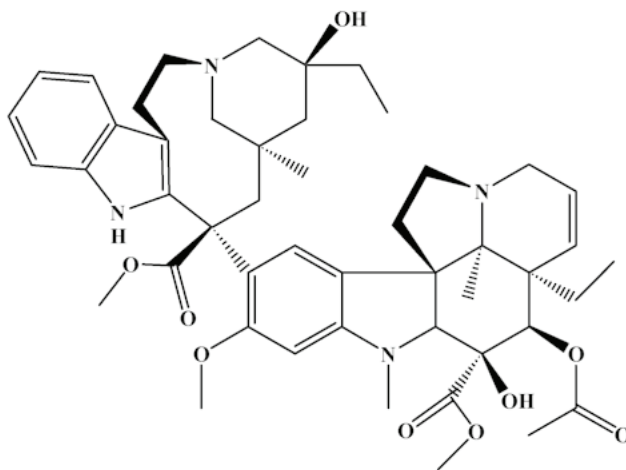


Figure 1.10: Structure of vinblastine. Image from *Mu et al.* (2012).

Vinblastine is a member of the vinca alkaloids, which are derived from the plant *Catharanthus roseus*. It binds to the vinca domain on tubulin, located on β -tubulin at the interdimer interface. Vinblastine was one of the first clinically approved antimitotic drugs used for chemotherapy, and its discovery initiated an extensive search by the National Cancer Institute for other plant-derived drugs (*Cragg and Newman*, 2005). Studies show that vinblastine binds with high affinity to microtubule ends ($K_D = 1 - 2 \mu\text{M}$), and that the binding of only one to two molecules per microtubule is enough to decrease tubulin exchange by 50%. Vinblastine also stabilizes interdimer kinks, which lead to curved protofilament conformations. Binding to secondary, low affinity sites along the microtubule surface ($K_D = 0.25 - 0.3 \text{ mM}$) causes microtubules to depolymerize via protofilament peeling, possibly due to weakening of lateral interactions between the protofilaments (*Panda et al.*, 1996; *Wilson et al.*, 1982). Effective vinblastine concentrations range from approximately 0.5 nM *in vivo* (IC_{50}) to approximately 100 nM *in vitro* (*Ngan et al.*, 2001; *Jordan et al.*, 1991).

Colchicine

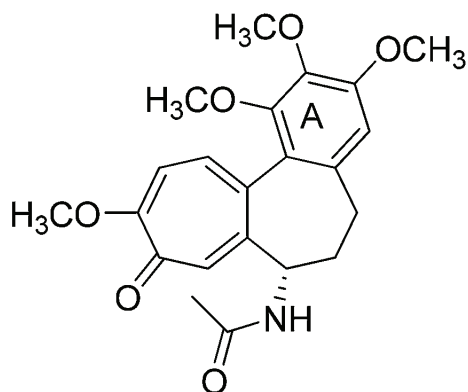


Figure 1.11: Structure of colchicine. Image from *Shen et al.* (2015).

Colchicine is microtubule destabilizing agent that binds to the colchicine domain on tubulin, which is located near the $\alpha\beta$ intradimer interface and is distinct from the aforementioned binding sites. It is another natural, plant-derived toxin (*Colchicum autumnale*) used clinically for treatment of gout, and similar to vinblastine, colchicine works by kinetically capping microtubule ends. However, unlike vinblastine, colchicine first forms a complex with soluble tubulin, which then binds to microtubule ends with an affinity ($K_d = 0.3 \mu\text{M}$) similar to that of non-complex tubulin. Binding of colchicine to tubulin sterically precludes the straight tubulin conformation, resulting in a kinked tubulin-colchicine complex, which, once bound to microtubule ends, blocks further polymerization (*Margolis and Wilson, 1977; Vandecandelaere et al., 1997*).

1.4.1 Drug Toxicity, Resistance, and Synergy

The use of microtubule-targeting drugs in medicine presents major issues, one of which is extreme toxicity, which can precipitate a number of diseases. The toxic effects of these drugs most prominently affect tissues with rapid cell turnover, often causing diseases such as neutropenia (low white blood cell count), which increases

a patient's risk of infection; mucositis (gastrointestinal inflammation and ulceration); neuropathy, which affects the autonomic and central nervous systems; and hypersensitivity. Furthermore, the excipients used to aid in the clinical delivery of some microtubule-targeting drugs (e.g. Cremophor EL, used to improve the aqueous solubility of paclitaxel) can lead to additional reactions. Each of these diseases is associated with a number of debilitating side effects, and therefore, the toxic effects of microtubule-binding drugs are dose-limiting (*Rowinsky et al.*, 1990).

Drug resistance is another issue that arises from the use of many chemotherapeutic agents, via mechanisms ranging from protein mutations to activation of various survival pathways. Research suggests that the development of taxane-refractory cancers may be due to an overexpression of the β -III tubulin isotype, which forms microtubules that are more than twice as dynamic as microtubules composed of purified β -II or β -IV tubulin, but also less stable than β -II- or β -I-derived microtubules (*Panda et al.*, 1994). Notwithstanding, in experiments where the less dynamic β -II isotype was spiked with β -III tubulin, the dynamicity was further *reduced*. Numerous other studies have documented the effects of α - and β -tubulin isotype fractions on microtubule dynamics and drug resistance both *in vitro* and *in vivo* (*Derry et al.*, 1997; *Banerjee et al.*, 1990; *Lu and Luduena*, 1993; *Kavallaris et al.*, 1997; *Ranganathan et al.*, 1998).

Drug efflux is another common mechanism of resistance that is mediated by the overexpression of proteins such as permeability glycoprotein (Pgp) and multidrug resistance (MDR) protein. While some long-used drugs like paclitaxel have a high affinity for Pgp, and thus are subject to high levels of cellular resistance, novel drug candidates that are poor Pgp substrates are currently being investigated. For example, peloruside A binds poorly to Pgp and shows effectiveness against paclitaxel-resistant cells (*Kanakkanthara et al.*, 2011). Moreover, studies have found that point mutations in tubulin can disrupt paclitaxel binding, or can decrease microtubule stability,

possibly as a compensatory action. In some cases this leads to an increased sensitivity to microtubule destabilizers such as vinblastine and colchicine, and surprisingly, retained sensitivity to epothilone B and the paclitaxel derivative 2-*m*-azido-benzoyl-Taxol (*Orr et al.*, 2003).

Because tubulin has a number of sites that bind various microtubule drugs, multiple drugs can be administered simultaneously at lower-than-normal concentrations to mitigate side effects. While one might expect the effects of multiple drugs to be additive, investigators have found that the effects may also be synergistic, or even antagonistic. For example, multiple studies have shown that when combined, paclitaxel and peloruside A synergistically reduce cell proliferation. Synergism was also found between paclitaxel and laulimalide, between epothilone A and peloruside A, and also between other drug combinations (*Miller et al.*, 2006; *Gapud et al.*, 2004; *Wilmes et al.*, 2011).

Whether two drugs interact synergistically or antagonistically can depend on the ratio of the drug concentrations and the particular test used to measure efficacy (*Chou et al.*, 1994). Interestingly, one study detected significant synergy between paclitaxel and epothilone A *in vivo*, despite the fact that no such interaction was reported in similar *in vitro* studies (*Hamel et al.*, 2006; *Gapud et al.*, 2004). Another report studying breast cancer cells indicated synergistic activity between paclitaxel and docetaxel, but only in cells overexpressing the Pgp efflux pump. In the same study the two drugs acted antagonistically in the parental cell line, and additively in a cell line that lacks the MDR protein (*Budman and Calabro*, 2002). Taken together, this indicates that two drugs with the same target site on tubulin may be able to interact, if not directly then perhaps via competitive binding to a drug efflux pump or differential binding to various tubulin isotypes (*Miller et al.*, 2006).

Thus, synergy allows multiple drugs to be used simultaneously, each potentially at levels below the threshold for toxicity; however combining drugs that bind different

sites does not guarantee synergy. This underscores the need for a thorough understanding of how microtubule-targeting drugs alter native microtubule dynamics to aid in the development of novel chemotherapy drugs.

1.5 Tubulin Structure and Interactions

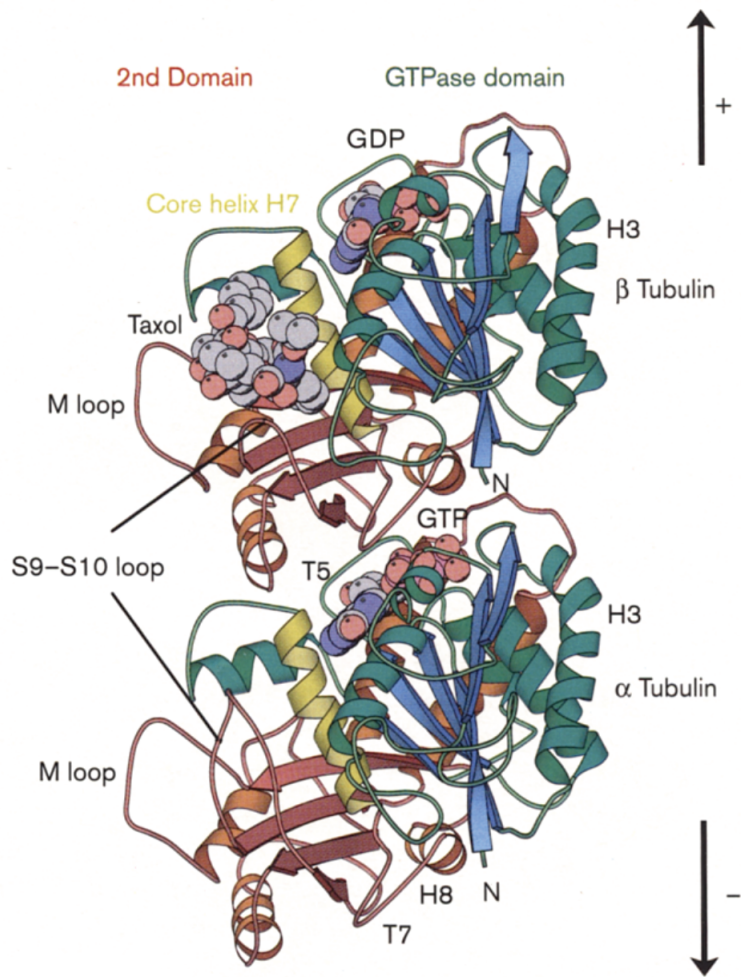


Figure 1.12: Structure of tubulin. The 3D structure of the $\alpha\beta$ -tubulin heterodimer was solved by *Nogales et al.* (1998) at a resolution of 3.7-Å using electron crystallography of zinc-induced tubulin sheets. The image shows the microtubule-binding drug paclitaxel (Taxol) and GDP bound to β -tubulin and GTP bound to α -tubulin. Image by *Amos and Löwe* (1999).

The tubulin heterodimer contains nearly identical α and β subunits, as can be seen in the ribbon diagram in Figure 1.12. The tubulin structure is composed of two

β -sheets containing 6 and 4 strands, which are surrounded by 12 α -helices (Nogales *et al.*, 1998). The monomer structure can be divided into three functional domains, which include the N-terminal, intermediate, and C-terminal domains. The N-terminal domain contains the E-site, where nucleotide binding and hydrolysis occur. During tubulin polymerization, the β -tubulin E-site becomes buried by addition of dimers at the plus end, making the nucleotide non-exchangeable, and exposing it to residues on α -tubulin which may promote hydrolysis (Nogales and Wang, 2006). The intermediate domain contains the binding sites of many microtubule-targeting drugs (Figure 1.13), which are described below. The C-terminus portion of the tubulin monomer contains the E-hook, a negatively charged series of residues that interact with molecular motors (e.g. kinesin and dynein) and many other microtubule-associated proteins (Lakämper and Meyhöfer, 2005; Brouhard *et al.*, 2008).

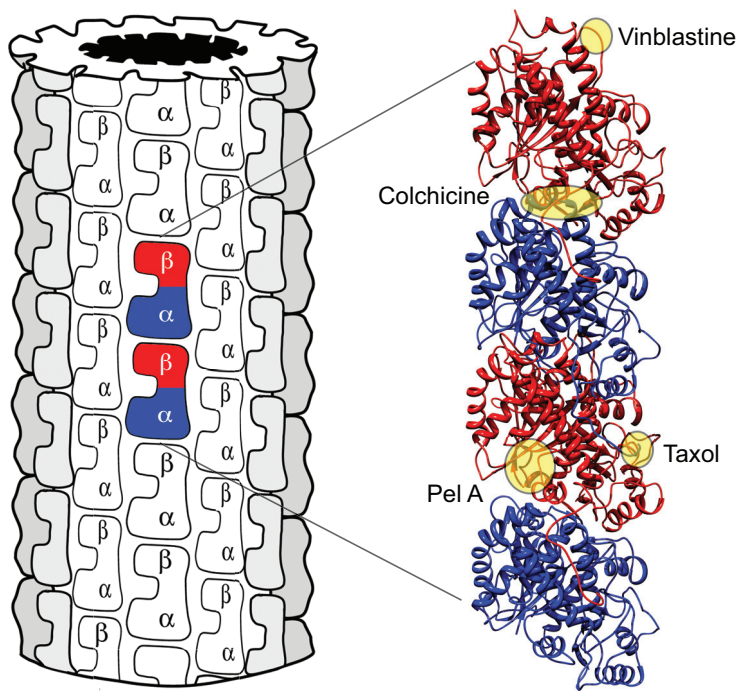


Figure 1.13: Tubulin drug binding sites. Structure of assembled $\alpha\beta$ -tubulin heterodimers, highlighting locations of the four established drug binding sites (yellow). Examples of drugs that bind to each of the sites are indicated beside each site. Illustration adapted from Sackett and Sept (2009).

1.5.1 The Taxoid Binding Site

The taxoid binding site is a hydrophobic pocket located on the luminal side of β -tubulin in the microtubule structure. The corresponding position in the α -tubulin monomer is occupied by an amino acid insertion between the S9–S10 loop, and therefore, does not bind any taxoid-site drugs. Ligands of the site include paclitaxel, the epothilones, docetaxel, zampanolide, and discodermolide, among others, all of which inhibit microtubule disassembly. Inhibition occurs via interaction with the tubulin M-loop and also, depending on the specific drug, with the S9–S10 loop, and helices H1, H6 and H7 (Figure 1.14). A number of studies have linked mutations in the M and S9–S10 loops of β -tubulin to paclitaxel, epothilone, and docetaxel resistance (Zhou, 2007; Giannakakou *et al.*, 2000), indicating the importance of these structural features in taxoid-site drug toxicity.

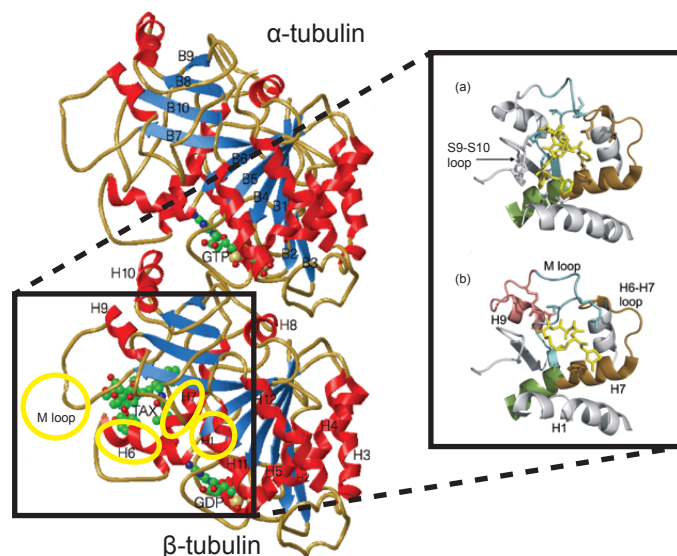


Figure 1.14: The paclitaxel binding site. Tubulin heterodimer showing bound paclitaxel (TAX) with interacting features circled in yellow (Image from *Nogales et al.* (1998)). Inset shows taxoid binding site occupied by paclitaxel (a) or epothilone A (b). Image from *Huzil et al.* (2008).

1.5.2 The Peloruside/Laulimalide Binding Site

The peloruside/laulimalide binding site was a relatively recent discovery. *Gaitanos et al.* (2004) performed competitive binding assays which revealed that the paclitaxel-like drug peloruside binds a tubulin site distinct to the paclitaxel site. They also found evidence that another drug, laulimalide, shares the same binding site. Further investigation by *Huzil et al.* (2008) and *Prota et al.* (2014) narrowed the binding site to an exterior pocket on β -tubulin, which is formed by the hydrophobic and polar residues of helices H9 and H10 and loops H9–H9' and H10–S9. In α -tubulin the H10 helix is tilted, and thus, it impedes binding to the corresponding site. Upon ligand binding

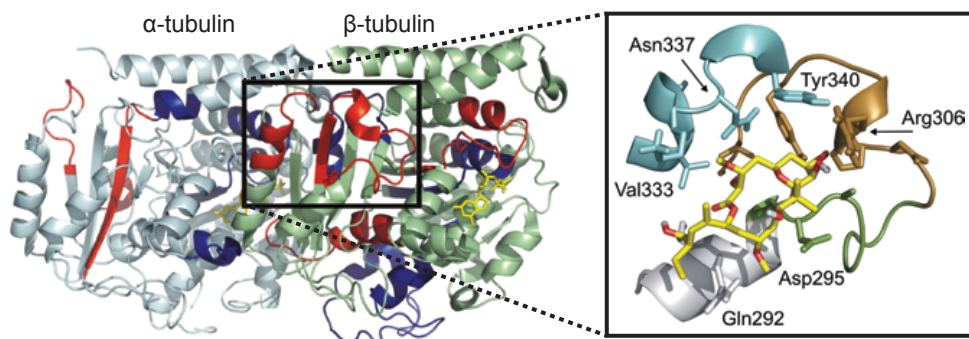


Figure 1.15: The peloruside/laulimalide binding site. *Left:* The probable location of the peloruside/laulimalide binding pocket as determined by comparative hydrogen-deuterium exchange mass spectrometry. *Right:* Detailed view of peloruside A (yellow) bound to the site. Images by *Huzil et al.* (2008).

to the peloruside/laulimalide site, the disordered M-loop is partially stabilized, which has implications for microtubule stability since the loop is directly involved in lateral tubulin–tubulin contacts between adjacent protofilaments. Furthermore, there is evidence that bound ligands may directly interact with helix H3 of β -tubulin on an adjacent protofilament.

Finally, previous work suggests that ligand binding to the peloruside/laulimalide pocket may allosterically stabilize the conformation of the taxoid pocket (*Khrapunovich-Baine et al.* 2011; see Figure 1.16). In support of this finding, multiple experimental studies have detected synergy between paclitaxel and peloruside/laulimalide (*Wilmes*

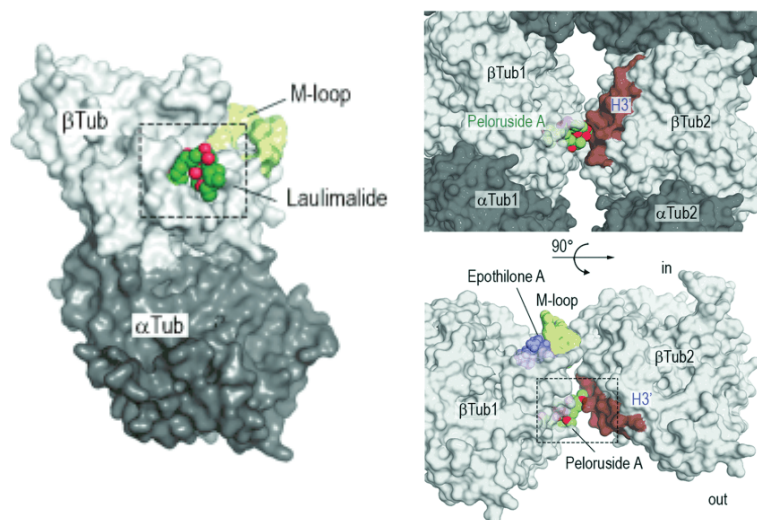


Figure 1.16: Peloruside/laulimalide intradimer interactions. Models predict that ligands bound to the peloruside/laulimalide pocket stabilize the M-loop and interact with helix of adjacent tubulin dimers. Allosteric stability of the paclitaxel pocket may also occur. Images from *Prota et al.* (2014)

et al., 2007, 2011; *Clark et al.*, 2006; *Gapud et al.*, 2004).

1.5.3 The Colchicine Binding Site

The colchicine binding site was determined by X-ray crystallography of tubulin in complex with colchicine and RB3 stathmin-like domain (RB3-SLD). The complex (T2R) comprises two head-to-tail tubulin dimers with colchicine bound to the β -tubulin subunits at the intradimer interface, and RB3-SLD, which is used to stabilize tubulin for crystallization. The colchicine site lies within the intermediate domain of β -tubulin and is flanked by strands S8 and S9, helices H7 and H8, and loop T7 (see inset of Figure 1.17). A number of drugs bind to the colchicine site including colchicine, combretastatins, podophyllotoxin, nocodazole, Curacin A, and 2-Methoxyestradiol (*Ravelli et al.*, 2004; *Lu et al.*, 2012).

The drug colchicine tightly binds to soluble tubulin, forming a tubulin-colchicine complex (TC). Once bound, colchicine sterically precludes the tubulin dimer from assuming a straight conformation. Binding also results in the displacement of the

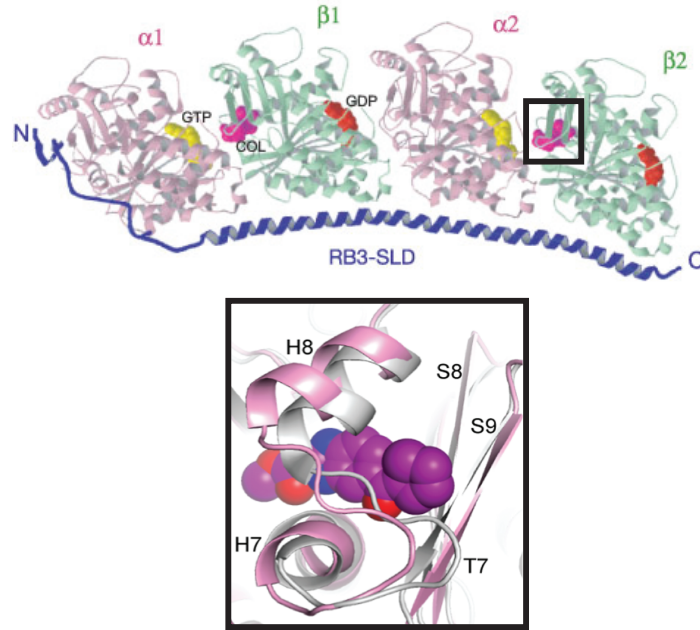


Figure 1.17: The colchicine binding site. *Upper:* Tubulin–colchicine:RB3–SLD complex used to determine the colchicine binding site. Colchicine is shown in magenta and bound nucleotides are shown on α - and β -tubulin in yellow and orange, respectively. *Lower:* Detailed view shows nocodazole bound to the colchicine site. Images by *Ravelli et al.* (2004) and *Wang et al.* (2016).

tubulin M-loop, which mediates lateral interactions between adjacent protofilaments that are necessary for microtubule stability. Thus, binding of the TC complex to the microtubule end effectively caps the polymer and prevents further polymerization (*Peng et al.*, 2014).

1.5.4 The Vinca Domain

The tubulin vinca domain is known to bind a diverse range of ligands (*Hamel*, 1992), including those derived from vinca plants (e.g. vinblastine, vincristine, vinorelbine, and vinflunine), marine species (e.g. dolastatin, halichondrins, hemiasterlins, and cryptophycins), and fungi (e.g. phomopsin and rhizoxin). Despite clinical use of vinca alkaloids for many decades, the exact binding site location was not determined until 2004 (*Mitra and Sept*, 2004), when the crystal structure of vinblastine bound to tubulin was finally solved (see Figure 1.18). The vinca domain is located at the interdimer

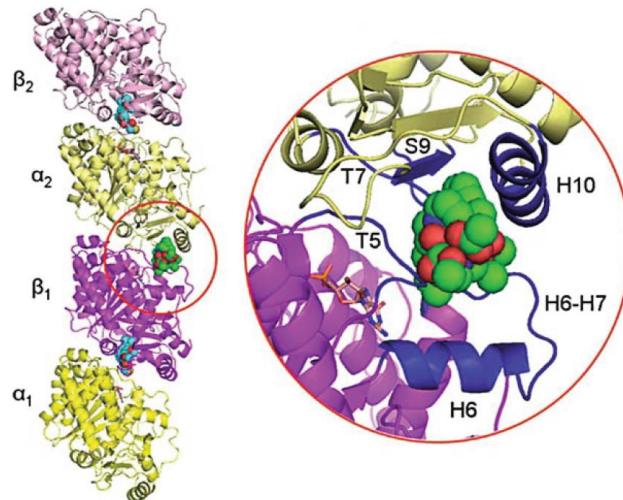


Figure 1.18: The vinca domain. *Left:* Vinblastine (green spheres) is shown bound to the vinca domain between two $\alpha\beta$ -tubulin heterodimers. In contrast to the colchicine ligands, which bind at the *intradimer* interface, vinblastine binds at the *interdimer* interface. *Right:* Detailed view of the vinca domain showing key secondary structures. Image by *Carlomagno* (2009).

interface, defined by helix H6 and loops T5 and H6–H7 in β -tubulin and by T7, H10, and S9 in α -tubulin of the longitudinally-adjacent subunit (*Carlomagno*, 2009).

Upon binding of drugs to the vinca domain, GTP hydrolysis and nucleotide exchange are inhibited, which is perhaps not surprising given the domain’s close proximity to the E-site. Binding also sterically prevents tubulin subunits from assembling in a straight configuration, which introduces protofilament curvature. This leads to the formation of spirals (in the case of vinblastine) or complete rings (phomopsin A or dolastatin 10), as the tubulin longitudinal bonds are stabilized in the curved configuration (*Cormier et al.*, 2008).

CHAPTER II

Studies of Microtubule Growth in the Presence of the Chemotherapeutic Agent Paclitaxel

Microtubules are dynamic polymers that are essential for cell structure, intracellular transport, and mitosis. They have been the subject of decades of research, since many effective chemotherapy drugs have been found to target these filaments. Even with wide clinical use of anti-microtubule drugs, research in the field is still highly active. Currently prescribed chemotherapy drugs cause a host of undesirable side effects, and therefore, novel alternatives with lower toxicities are sought. In the process of screening new drugs, it is essential that we study the characteristics of known drugs to understand why they are effective, and also how they are toxic.

2.1 Effects of Paclitaxel on Microtubule Growth Determined Using DIC and TIRF Microscopy

Paclitaxel is chemotherapy drug that was approved in the early 1990s that has been successfully used to treat lung, ovarian, and breast cancers (*Rowinsky et al.*, 1992). Unlike any of the drugs in use before its discovery, paclitaxel was found to promote microtubule stability and increase polymer mass, as opposed to the early anti-mitotics, which drive microtubules toward disassembly when used at higher con-

centrations. However, even now, more than 50 years after it was first discovered for its potential chemotherapeutic effects, and more than 20 years since it was approved for clinical use, little is known about the mechanistic details of how paclitaxel alters microtubule assembly. To understand why paclitaxel is an effective chemotherapy drug, I examined its effect on microtubules using various microscopy techniques. I conducted preliminary studies using differential interference contrast (DIC) microscopy to determine suitable paclitaxel and tubulin concentrations. Then I performed additional experiments using total internal reflection fluorescence (TIRF) microscopy to characterize microtubule polymerization in the presence of clinically relevant, nanomolar concentrations of paclitaxel. Such studies were performed to address, for example, whether transient shortening events during periods of net growth—also referred to as “growth-phase shortening”—are inhibited at low paclitaxel concentrations, and to what extent paclitaxel inhibits the off-rate of tubulin, versus increasing the on-rate. I hypothesized that low concentrations of paclitaxel would suppress the tubulin off-rate and reduce the frequency of transient shortening events.

2.1.1 Determination of Relevant Paclitaxel Concentrations Using DIC Microscopy

As a first step in understanding how substoichiometric paclitaxel concentrations alter native microtubule dynamics, I referenced paclitaxel studies by *Derry et al.* (1995), who investigated the effects of paclitaxel on *in vitro* microtubules at concentrations ranging from 10 nM to 1 μ M. In their studies, microtubules were elongated from axoneme seeds at 30 °C using 17 μ M purified tubulin with 1 mM GTP in buffer. The microtubule-tubulin solution was incubated for approximately 30 minutes to allow the system to equilibrate, and then paclitaxel dissolved in methanol ($\leq 1\%$ v/v) was added, followed by an additional incubation period of 25 minutes. Images were captured in real time and recorded onto VHS cassette tape, and length data was col-

lected at 15 seconds intervals with a spatial resolution of $0.2 \mu\text{m}$. *Derry et al.* found that concentrations of paclitaxel under 100 nM had a negligible effect on the plus end growth rate, however, concentrations as low as 10 nM were sufficient to significantly reduce the average shortening rate. At 100 nM the average growth rate was reduced by 31%, from 83 to 57 dimers/s (51 to 35 nm/s), and 1 μM reduced the growth rate by 63% down to 31 dimers/s (19 nm/s). At concentrations of paclitaxel ≥ 100 nM microtubule plus and minus ends became indistinguishable. No effects on catastrophe and rescue frequencies were detected at concentrations ≤ 500 nM, above which both became extremely rare.

I performed experiments similar to *Derry et al.*, but with several key differences. First, I collected data during steady-state microtubule growth, that is, immediately after addition of tubulin to the experimental slide. *Derry et al.* and many others who have studied *in vitro* microtubule dynamics did so after allowing tubulin monomer and polymer to equilibrate prior to data collection. This means that mass action effects would have shifted the free tubulin concentration to the tubulin critical concentration, where the on and off rates of tubulin to and from the microtubule are at equilibrium. By studying microtubules at steady-state, I was able to examine the simultaneous effects of adjusting both the tubulin and drug concentrations. Second, I collected data at 30 Hz, and employed frame averaging to yield 0.5 Hz processed data, which is somewhat faster than the temporal resolution of 0.07 Hz used by *Derry et al.* A higher temporal resolution was necessary for detecting growth-phase shortening events (*Schek et al.*, 2007) which help to describe the intrinsic variability in microtubule growth. Furthermore, a modest degree of frame averaging improved spatial resolution while still maintaining a relatively high temporal resolution. Lastly, I performed post processing in Matlab using cross-correlation of video frames to aid in objectively tracking the microtubule tip position.

For my study, video-enhanced differential interference contrast (DIC) microscopy

was used to image microtubules. DIC is a microscopy technique used to provide contrast and generate pseudo-three dimensionality to optically transparent samples. Unpolarized light is passed through a polarizing filter before entering a modified Wollaston prism, which splits the polarized light into two perpendicular components. These two beams emerge from the prism traveling in slightly different directions. The divergent beams pass through a condenser and exit as parallel beams, though now separated by a small shear distance. Lateral shearing of the beam is less than the diameter of the Airy disk (that is, below the diffraction limit), which prevents the appearance of double images. Because of the shearing and differences in polarization angle, the beams do not interfere with one another. As they pass through the sample, the beam paths are altered by the varying refractive indices and features of the specimen. Light collected by the objective lens is then recombined by a second modified Wollaston prism, which removes the shearing and path differences introduced by the first prism. However, because the beams have traversed the sample, their resulting path lengths differ. The two beams pass through a second polarizer and emerge at a single polarization angle, allowing them to combine. Differences in specimen features manifest as contrast gradients, or shadows, along the specimen's edges (*Allen et al.*, 1981).

Video-enhanced DIC microscopy improves the utility of conventional DIC microscopy by using digital image processing to display enhanced images in real time. Image processing for the first portion of my data collection was performed by a Hamamatsu Argus camera controller, which provided background subtraction, frame averaging, and contrast improvement. Such enhancements allowed visualization of features that could not be easily seen by eye in raw frames. Imaging microtubules using conventional DIC microscopy was challenging because cover slip debris was often of much higher contrast than microtubules. With background subtraction, growing microtubules were clearly visible since they were the only objects in the frame that

changed over time.

Shortly after beginning paclitaxel experiments, the Hamamatsu Argus controller failed, making data collection extremely difficult and inefficient. Without the enhanced video feed, it often required several minutes to locate the cover slip surface and find a suitable arrangement of bound microtubules. By then there was limited time to collect data before the microtubules had grown too long to image. Since the Argus controller was legacy hardware, and because newer systems were either incompatible or prohibitively expensive, we determined that our best course of action was to programmatically emulate the Argus controller. To do this, I set up a dedicated image processing computer and created Matlab software to process the raw image stream.

Matlab has a powerful image processing toolbox well-suited for image enhancement; however, there was a challenge not in replicating all of the processing features of the Hamamatsu Argus, but doing so in real-time, at a rate of around 10 Hz or faster. Significant issues hindered progress, including problems with video card compatibility, memory leaks, and other discovered Matlab bugs. For example, when simply capturing raw images for display, Matlab would consume increasing amounts of memory, and within minutes the entire operating system would crash. I was able to fix this problem by adding code to continuously flush the video data buffer. I experienced another issue when attempting to display the enhanced image while simultaneously logging raw data; the solution in this case was to launch a second, headless instance of Matlab to handle the task. Other problems were solved by using built-in functions in unconventional ways, and also through many phone conversations with Matlab technical support. Eventually, I was able to replicate all of the features of the Argus controller while also implementing a number of other useful functions. This was accomplished while achieving stable frame rates of 7–15 Hz, depending on the features used.

Once the image processing software was operational, I collected growth data using 5 and 12 μM tubulin with paclitaxel concentrations ranging from 0 – 100 nM. Microtubules were elongated in flow cells from biotinylated GMPCPP-stabilized seeds. Because of its hydrophobicity, paclitaxel was dissolved in methanol and prepared as 100 μM stock. The final methanol concentration in paclitaxel experiments was fixed at 1% (v/v) by serial diluting the 100 μM stock in a variable amount of methanol and then further diluting by 100 \times into the experimental solution to achieve the desired concentration. Microtubule studies by *Derry et al.* indicate that methanol concentrations of $\leq 1\%$ do not detectably affect microtubule dynamics. All data was captured within 20 minutes of slide preparation.

Prior to data collection a background image was captured for the current field of view, and then unprocessed microtubule growth data was captured at 30 Hz. For data analysis, background subtraction was applied to the raw frames (using the previously captured background image), which were then temporally averaged using 60-frame independent windows. Next, the images were contrast-enhanced, upsampled by 10 \times (without interpolation), drift corrected, and used to generate kymograph images. Microtubule growth rates were obtained by applying a linear fit to the first and last time points of growth phases on the kymographs. Plus and minus ends were distinguished based on the growth rates for each microtubule, with the faster growing end presumed to be the plus end.

Unfortunately, most of the data resulting from these experiments was lost; a backup hard drive was damaged and the original data acquisition computer, retired years ago, is missing its hard drive. However, hard copy documentation has preserved some of the quantitative and qualitative results. I found that at 5 μM tubulin the mean growth rates for the plus and minus ends were 88 ± 5 and 21 ± 3 nm/s, respectively. Addition of 50 nM paclitaxel reduced the plus end growth rate 30% (62 ± 5 nm/s) but did not significantly affect the minus end rate (19 ± 3 nm/s).

100 nM paclitaxel lowered the plus end rate by 44% (49 ± 6 nm/s) from control and reduced the minus end rate by 47% (11 ± 3 nm/s). These results indicate that paclitaxel strongly suppresses the growth rates at both microtubule ends at nanomolar concentrations.

However, I also observed, qualitatively, that the growth rate of paclitaxel microtubules slowed significantly within 5 minutes after slide preparation. Furthermore, within 15 minutes all microtubules had stopped growing and most had depolymerized back to the stabilized seed. Interestingly, I did not observe these effects at 12 μ M tubulin, nor did *Derry et al.* at 17 μ M (30 °C). In fact, *Derry et al.* observed only modest changes in the plus end growth rates for the same range of paclitaxel concentrations (0 – 100 nM). From a literature review I found that methanol has cytotoxic effects and is a common cytological fixative (*Kumarasinghe et al.*, 1997; *Berrueta et al.*, 1998), though for fixation purposes it is often used at much higher concentrations. To determine whether methanol was affecting microtubule growth, I performed control growth experiments without methanol. I found that without methanol the microtubules grew normally, undergoing multiple rounds of polymerization and depolymerization. I also performed a control experiment using 0.1% methanol to find out if use of a lower methanol concentration would eliminate its toxic effects. I found that at 0.1% the effects were mitigated but still apparent.

From these results it was clear that methanol affects microtubule polymerization at concentrations as low as 0.1%. What was not immediately clear was why depolymerization was not observed at 12 μ M tubulin. It is possible that with higher free tubulin concentrations, there is more tubulin to react with and neutralize the methanol, of which there is a fixed concentration. It may also be that a higher net growth rate, driven by a higher free tubulin concentration, somehow mitigates the apparent effects of methanol. Whatever the cause, my findings indicate that results from studies of microtubules containing any amount of methanol should be viewed

with skepticism.

2.1.2 Resolution Improvements using TIRF Microscopy

Analysis of microtubule growth using DIC microscopy had proven difficult in part because the orientation of the high contrast edges depends on the angle of the microtubules relative to the DIC optical components. If the maximum contrast gradient is orthogonal to the microtubule axis, then shadows highlight the lattice in great detail and allow microtubules to be easily identified. However, at this orientation the contrast at the tip in the direction of the microtubule axis is at a minimum. This presents an issue for automated tip tracking, which is ideally used for objective analysis and higher data throughput. While a computer algorithm can easily identify long, high-contrast microtubule filaments, locating the exact position of a low-contrast tip is difficult. Conversely, high contrast along the microtubule axis would present the tip in great detail, however, the first action of locating the microtubule itself would become challenging. Moreover, selecting microtubules at particular orientations greatly reduces the number that can be used for analysis in a particular field of view.

To overcome these challenges, a new data set was collected using a dual-color total internal reflection fluorescence (TIRF) microscope, which was part of a multi-use facility designed and built by colleague Aghapi Mordovanakis. TIRF illumination produces a shallow excitation field with a characteristic decay length of several hundred nanometers into the sample. This type of illumination profile eliminates more than 99% of background fluorescence for 100 μm deep flow cells, allowing microtubules in the evanescent field to fluoresce brightly with minimal background contamination by free tubulin subunits.

Furthermore, published studies have documented reliable methods for semi-automated tip tracking with sub-pixel resolution (*Demchouk et al.*, 2011; *Bicek et al.*, 2007). In short, because optical microscopy is diffraction-limited, resolution is limited to ap-

proximately 200 nm. Image data represents the convolution of the specimen with the point spread function (PSF) of the microscope. However, with a known PSF, the image can be deconvolved to localize positions of fluorescent structures with high precision. This can be accomplished if the pixel size of captured images is smaller than the width of the PSF, such that the signal for each point source is spread over multiple pixels (*Ruhnow et al.*, 2011). The pixel size of the TIRF microscope is approximately 90 nm, so sub-pixel tip tracking could be implemented once the PSF was estimated.

The Tip Tracker software—used to analyze image data—estimates the PSF standard deviation (σ_{PSF}) using a 1D Gaussian fit to the PSF Airy disk approximation (*Zhang et al.*, 2007). PSF values are estimated for positions on an $n \times n$ mesh according to:

$$PSF(i, j) = \left[\frac{2 J_1(\alpha z)}{\alpha z} \right]^2 \quad (2.1)$$

where J_1 is a first order Bessel function of the first kind, $i = [1, n]$ and $j = [1, n]$ are mesh coordinates, α is the Airy disk parameter

$$\alpha = \frac{2\pi NA}{\lambda} \quad (2.2)$$

where NA is the objective lens numerical aperture and λ is the fluorophore emission wavelength, and

$$z = p \sqrt{\left(i - \left(\frac{n}{2}\right)^2\right) + \left(j - \left(\frac{n}{2}\right)^2\right)} \quad (2.3)$$

where p is the pixel size. σ_{PSF} is estimated by fitting the 1D Gaussian function to a line scan the of PSF values at $i = n/2$:

$$f(x) = \beta_1 e^{-(x-\mu)^2/(2\sigma_{PSF}^2)} + \beta_2 \quad (2.4)$$

where μ is the mean of x and β_1 and β_2 additional fitting parameters. Employing

PSF deconvolution with TIRF microscopy tip tracking yields an expected tracking resolution of ~ 36 nm (*Demchouk et al.*, 2011) or as low as 11 nm for densely-labeled microtubules (*Gardner et al.*, 2011a).

To perform microtubule polymerization experiments using TIRF microscopy, it was necessary to modify my flow cell protocol to minimize tubulin surface accumulation, which could (1) reduce the microtubule signal to noise ratio (SNR) and (2) potentially reduce the free tubulin concentration. To determine if surface binding by tubulin would significantly affect the free concentration, I estimated the reduction in free tubulin concentration for the case of complete surface saturation. For a 15 μL flow cell with typical channel dimensions of 22 x 7 x 0.1 mm, I estimated that when using 5.6 μM tubulin complete surface saturation would only reduce the free tubulin concentration by less than 0.3%, assuming that tubulin binds the surface at its end (approx. 4 x 4 nm) (*Dowben and Shay*, 2013). This calculation indicated that tubulin surface binding would negligibly effect the free subunit concentration. However, it was still necessary to limit surface adsorption to achieve a high SNR necessary for high resolution tip tracking.

To mitigate surface binding at the imaging plane, I prepared cover slips using a previously documented method by (*Gell et al.*, 2010). Cover slips were first acid washed to remove auto-fluorescent debris and then treated with dichlorodimethylsilane (DDS) to render the surface hydrophobic. During sample preparation surface passivation by Pluronic F127 completed the blocking system. In contrast to the documented protocol, which suggested liquid-phase silanization, I initially used gas-phase adsorption of DDS to the cover slips. The same methods document was used for adhering biotinylated GMPCPP-stabilized seeds to the cover slip surface.

GMPCPP-stabilized microtubule seeds were prepared using 25% Cy3.5 tubulin, and seed extensions were grown using HiLyte Fluor 488 tubulin purchased from Cytoskeleton Inc. (Denver, CO, USA). The TIRF microscope used for this data set

contained two excitation lasers (491 and 561 nm) and a corresponding filter set suitable for simultaneously imaging both fluorophore types. Images for each color channel were captured on separate halves of a Hamamatsu C9100-13 EMCCD camera and combined in Matlab software for further analysis.

Because of the aforementioned issues with using methanol in microtubule assays, I first performed control experiments to compare microtubules grown at 5.6 μM tubulin with and without 1% DMSO to confirm its suitability as an inert paclitaxel solvent. Microtubules tip positions were tracked using modified Tip Tracker software (see Methods chapter) provided by the David Odde Lab (University of Minnesota), and growth parameters were determined using a biased diffusion (diffusion-with-drift) analysis, as described in Chapter 1. The diffusion-with-drift model assumes that the mean squared growth increments ($\langle \Delta L^2 \rangle$), measured over increasing time intervals (Δt), are equal to the sum of (1) a drift term, $v_g^2 \Delta t^2$, the coefficient of which is the square of the average growth rate; (2) a diffusion term, $2D_p \Delta t$, which describes the variability in the growth rate; and (3) a constant, σ^2 , representing the measurement noise (Equation 2.5).

$$\langle \Delta L^2 \rangle = v_g^2 \Delta t^2 + 2D_p \Delta t + \sigma^2 \quad (2.5)$$

My results showed that the growth rates (v_g) and diffusion terms (D_p) for control ($v_g = 0.425 \pm 0.027 \mu\text{m}/\text{min}$; $D_p = 1.16 \times 10^{-4} \pm 1.8 \times 10^{-5} \mu\text{m}^2/\text{s}$; $n = 46$) and 1% DMSO microtubules ($v_g = 0.417 \pm 0.020 \mu\text{m}/\text{min}$; $D_p = 0.90 \times 10^{-4} \pm 1.2 \times 10^{-5} \mu\text{m}^2/\text{s}$; $n = 37$) are equivalent, and thus, 1% DMSO did not affect microtubule growth.

Next, I prepared aliquots of paclitaxel in DMSO for use in TIRF experiments. Paclitaxel is extremely hydrophobic and can form crystals when exposed to aqueous solution (*Foss et al.*, 2008). When this happens, the actual concentration of paclitaxel interacting with microtubules can be greatly reduced, as paclitaxel may effectively sequester itself. While there is only a small likelihood of crystal formation

at nanomolar paclitaxel concentrations, I further minimized this risk by pre-diluting paclitaxel stock by 1000 \times in buffer before further dilution into the experimental solution. For the initial dilution, 1 μ L of paclitaxel in DMSO was added into the cap of an Eppendorf centrifuge tube containing 999 μ L of buffer and then vortexed for 10 seconds. This procedure ensured that the paclitaxel stock did not contact the buffer until vortexing began. Serial dilution further reduced the final DMSO concentration to less than 0.1%.

I grew microtubules at 5.6 μ M tubulin with paclitaxel concentrations ranging from 0 – 480 nM and tracked microtubule length changes using Tip Tracker. Figure 2.1 shows sample length traces for control and paclitaxel microtubules, as well as sample kymographs of image data. In post tracking analysis microtubule growth phases were selected from length versus time plots. Data with noise excessive noise—determined according to a threshold value of a running standard deviation—was removed by examining length plots while simultaneously reviewing the growth videos. Video frames were overlaid with markers designating the seed ends and tracked tip position, and length plots contained an overlaid marker to designate the current video frame. In nearly all cases, noise in the length data could be clearly attributed to events such as diffusing fluorescent debris, shifting microtubules, focus drift, or diffusion of the microtubule tip out of the evanescent field.

Length data was then analyzed using diffusion-with drift analysis (Equation 2.5) as described by *Gardner et al.* (2011a). Because the number of mean squared displacement (MSD) data points decreases as the analyzed time interval (Δt) increases, the plot of MSD versus Δt deviates from the expected quadratic trend at large values of Δt . Therefore, the last 25% of MSD data points was removed before continuing the analysis.

Growth rate data was analyzed by ANOVA and multiple comparisons analysis. Results from this preliminary data set (Figure 2.2) indicate that the mean growth

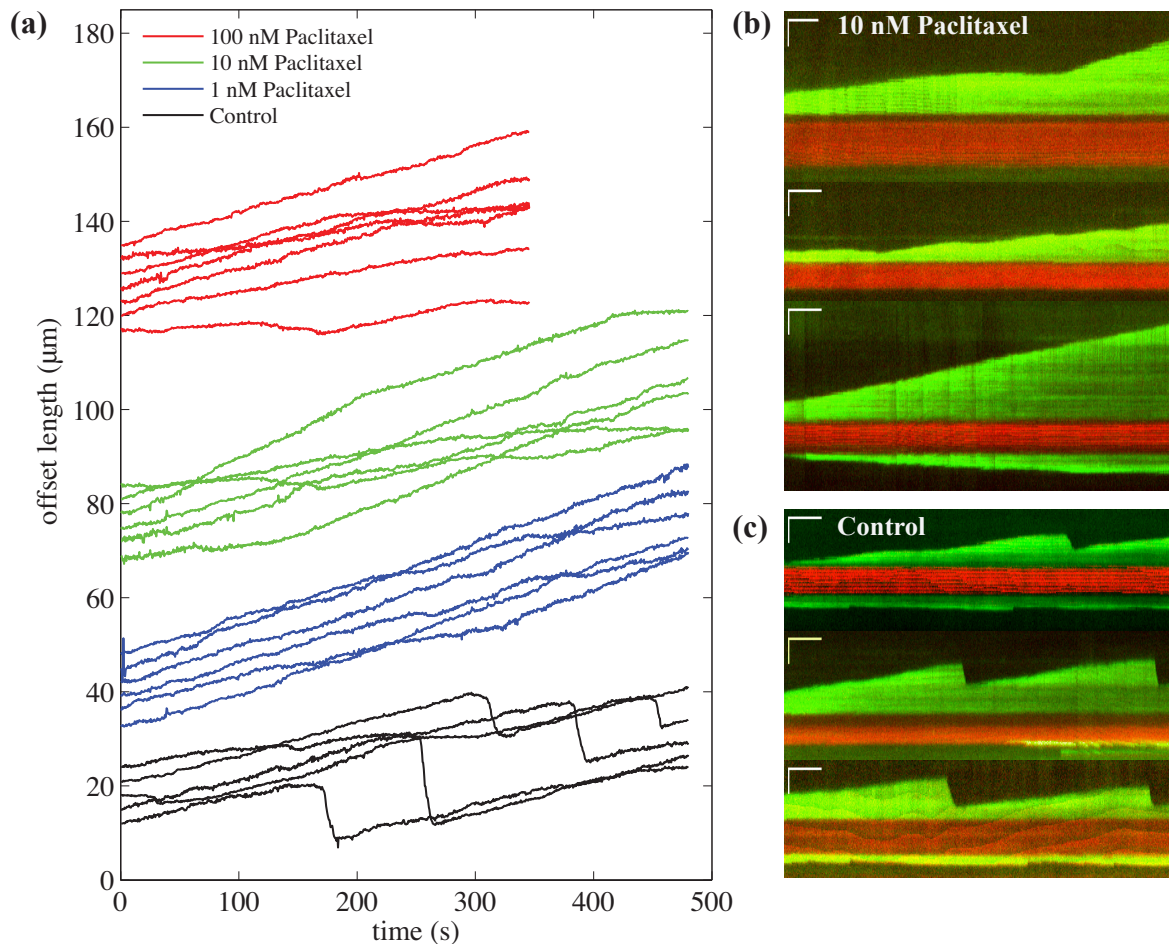


Figure 2.1: Sample microtubule length traces and kymographs. (a) Sample microtubule length traces from tip track output. Images were captured using 120-ms exposures, which were averaged to 480-ms prior to tracking. Length data is shifted vertically both within and between groups for clarity. (b) Sample kymographs showing growth of 55% HiLyte 488 tubulin extensions (green) from GMPCPP stabilized Cy3.5 seeds (red) for microtubules grown with $5.6 \mu\text{M}$ tubulin and 10 nM paclitaxel. Shortening events were completely suppressed and in some cases the net growth rate changed abruptly (green and red length traces). Vertical and horizontal scale bars are $2 \mu\text{m}$ and 60 seconds, respectively, for all images. (c) Kymographs for control microtubules grown with $5.6 \mu\text{M}$ tubulin. In this data set many shortening events rescued and did so at similar locations along respective microtubules.

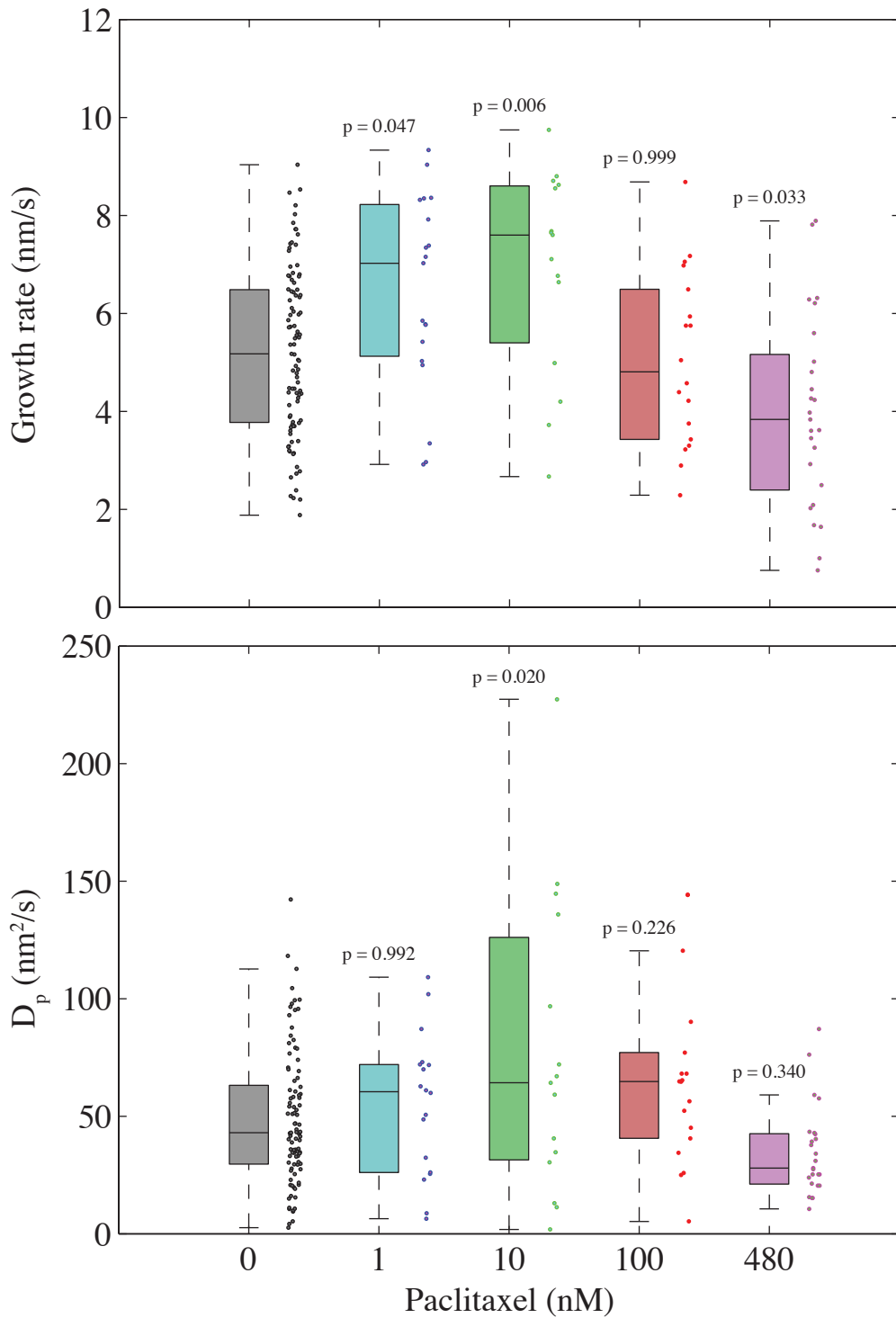


Figure 2.2: Box plots of microtubule growth parameters. Box plots showing growth rate and diffusion coefficient data for microtubules grown with 5.6 μ M tubulin and 0 – 480 nM paclitaxel. P-values indicate significance levels with respect to [paclitaxel] = 0.

rate is unaffected by all tested paclitaxel concentrations with the exception of 10 nM, which showed a significant increase ($p = 0.006$) of 34% from control (Table 2.1). Similarly, the effective diffusion coefficient showed no significant change for any paclitaxel concentration. Mean values of growth rates and diffusion coefficients (Table 2.1) suggest that lower concentrations of paclitaxel (≤ 10 nM) may enhance the growth rate and diffusion coefficient (and thus, $k_{on,MT}^*$ and $k_{off,MT}$), while higher concentrations (≥ 100 nM) may cause a reduction in those parameters; however, because of limited sample size at each paclitaxel concentration, more data is necessary to establish significant differences in microtubule behavior.

Despite paclitaxel's tenuous effect on the growth rate, low concentrations potentially affected the catastrophe frequency. Shortening events were observed for nearly every control microtubule during the 10-minute data acquisition periods, however, few were observed with 1 nM paclitaxel, and none were observed at concentrations ≥ 10 nM. Interestingly, at higher paclitaxel concentrations there were sudden changes in the net growth rate (Figure 2.1). Though earlier work has shown that the growth rate of control microtubules does vary over shorter time scales of several seconds (*Gardner et al.*, 2011a), paclitaxel microtubules exhibited distinct phases of net growth lasting on the order of 100 seconds, and in many cases the transition between these phases was abrupt. It is possible that as the paclitaxel concentration increases these transitions may become more frequent, or certain phases may persist for longer time periods. Such transitions may be precipitated by structural changes at the microtubule tip, and therefore these results warrant further analysis.

Table 2.1: Microtubule growth parameters

Paclitaxel concentration, nM	Growth rate, nm/s	Diffusion coefficient, nm ² /s	On rate, s ⁻¹	Off rate, s ⁻¹	No. of observations
0	5.16 ± 0.18	48.43 ± 2.89	132 ± 8	124 ± 8	98
1	6.43 ± 0.46	52.11 ± 7.27	143 ± 19	132 ± 19	19
10	6.90 ± 0.54	76.50 ± 16.35	207 ± 43	196 ± 43	15
100	5.05 ± 0.42	66.20 ± 9.08	179 ± 24	171 ± 24	18
480	3.97 ± 0.39	34.59 ± 3.79	95 ± 10	88 ± 10	25

TIRF images were collected as 120-ms streaming exposures from microtubules grown with 5.6 μ M tubulin using a range of paclitaxel concentrations. Length data was obtained by integrating frames to 480-ms and tracking microtubule tip positions using modified Tip Tracker software. Growth phase data was analyzed using a diffusion-with-drift model. Each observation includes growth phase data traces containing at least 20 data points (9.6 seconds).

In preparation for additional experiments, I purified a new batch of bovine tubulin (see Methods chapter). At the end of the preparation, I performed two SDS-PAGE gels—one stained with Coomassie brilliant blue and the other with a more sensitive silver stain—to determine the purity of the new tubulin batch and to compare it with past tubulin preparations. I also added HiLyte 488 tubulin from Cytoskelon Inc. for comparison with a commercial tubulin source. I found my new tubulin batch to look nearly identical to the two older batches tested from my lab. The silver stain gel, which has a detection limit of 1 ng, was overloaded with 2 μ g of each tubulin source and overexposed to identify possible contaminants not visible in the Coomassie blue stain. I found each of my lab’s tubulin preparations to be free of contaminants, however, I was surprised to find that the lane with tubulin from Cytoskeleton Inc. contained a dark band around 100 kDa (Figure 2.3). Upon closer inspection, this contaminant was visible even in the Coomassie blue stained gel, which has a detection limit of about 100 ng (*Weiss et al.*, 2009). I consulted *Guidebook to the Cytoskeletal and Motor Proteins* (*Kreis and Vale*, 1993) but was unable to identify

the contaminant. To be certain that my tubulin was pure, I had it analyzed using mass spectrometry, which showed no issues.

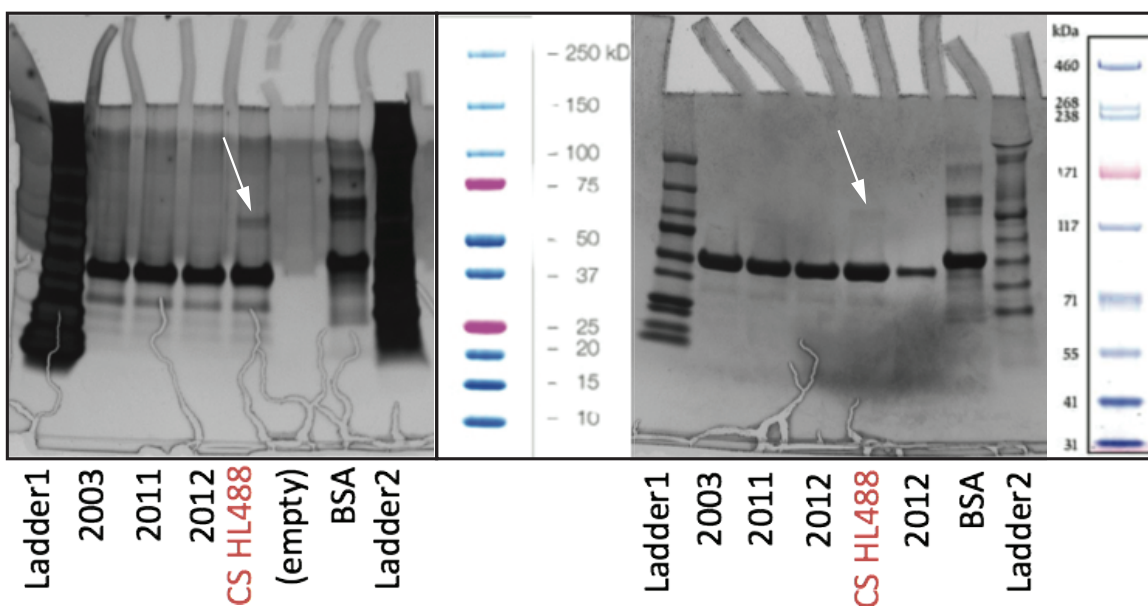


Figure 2.3: Images of tubulin SDS-PAGE gels. Tubulin SDS-PAGE gels reveal an unidentified contaminant in HiLyte 488 tubulin from Cytoskeleton Inc (CS HL488). *Left:* Silver stain gel showing contaminant marked with an arrow. *Right:* Coomassie blue stain gel.

Since the contaminant in the commercial tubulin could not be identified, I immediately stopped using it and prepared a batch of HiLyte 488 tubulin using a portion of my previously purified tubulin stock to be used for future TIRF experiments (see Methods chapter for labeling protocol).

2.2 Single-channel TIRF Microscope Design

Before starting data collection, my lab designed and built a new TIRF microscope to be used specifically for microtubule polymerization experiments. Since the original TIRF microscope was part of a multi-use facility, it was necessary to schedule around other users' reservations. Moreover, because the microscope was also used for epifluorescence microscopy, it occasionally required realignment, which was a time-consuming process since two separate beam paths required simultaneous optimization.

The dual-color setup of our original TIRF microscope required division of the camera sensor in order to capture two separate channels, which effectively halved the amount of data that could be collected at a given seed concentration. Furthermore, because of the alignment complexity encountered from using a dual-channel setup, illumination uniformity was mediocre and further reduced the usable CCD area. Considering these limitations, we designed our new TIRF microscope with a simplified optical path for single-color fluorescence experiments. Our goal was to build an optical path that would provide both uniform illumination over the entire camera sensor and easy alignment. With help from my colleague, Aghapi Mordovankis, I began by making calculations to determine the necessary optical components, given items we already had in inventory.

Working backwards from the camera sensor, we assumed that a 12 mm full width at half maximum (FWHM) Gaussian beam would provide relatively uniform illumination on our 8 mm camera CCD chip. At this expansion, the expected intensity drop off would be less than 30% from the center to edge of the sensor. Given the relationship between FWHM and the $1/e^2$ full beam width, w_D , (*Irick*, 1984):

$$w_D = \frac{\sqrt{2}}{\sqrt{\ln(2)}} \times \text{FWHM} \quad (2.6)$$

we calculated a $1/e^2$ full width of approximately 20 mm. We had already purchased a Zeiss Plan-Apochromat 100×1.46 NA objective, which meant that the illuminated area on the sample would be $200 \mu\text{m}$. The magnification from the sample plane to the incoming, collimated beam is equal to the ratio of the focal lengths of the condenser and objective lenses, which are 125 mm and approximately 1.65 mm, respectively, giving a ratio of about 76. Thus, the collimated TIRF beam should have a $1/e^2$ diameter of $200 \mu\text{m} \times 76 \approx 15000 \mu\text{m}$, or 15 mm.

The Gaussian beam equation describes the intensity of a beam at some radius, r ,

from the beam center (*Newport*, 2016)

$$I(r) = I_0 e^{(-2r^2/\omega_0^2)} \quad (2.7)$$

where I_0 is the intensity at $r = 0$ and ω_0 is the radius at which the intensity has decreased to $1/e^2$. Using this equation, it can be shown that the $1/e^2$ radius (r_{e^2}) is related to the 1/100 radius (r_{100} , where the intensity drops to 1/100 of the maximum) by

$$r_{100} = -\frac{\ln(0.01)}{2} r_{e^2} \quad (2.8)$$

indicating that the 1/100 diameter of the collimated TIRF beam should be approximately 23 mm, which should fit within a standard 1" optical path. Finally, the focal length, f , of an appropriate collimating lens was determined from the definition of numerical aperture (NA):

$$\text{NA} = n \sin \theta \quad (2.9)$$

where n is the index of refraction of the medium in which the beam is traveling ($n = 1$ for air) and θ is the half-angle of the beam cone, the edge of which is defined by a drop to 1/100 of the peak intensity for single mode fibers. Given that $\text{NA} = 0.12$ for our fiber, we used the small-angle approximation to estimate that $\theta \approx 0.12$, and similarly, that $\tan \theta \approx 0.12$. Since $\tan \theta$ is equal the ratio of r_{100} over f , we found that the focal length of our collimating lens should be 100 mm.

We selected excitation and emission filters for use with a Cobalt Calypso 491 nm excitation laser and HiLyte Fluor 488 fluorophore, which has excitation and emission peaks at 497 and 525 nm, respectively. We used a Semrock Di02-R488 excitation filter with a cutoff at 496 nm and a Chroma ET535/70m emission (bandpass) filter which passes 499 to 568 nm. At first we had selected a Di01-R488 excitation filter but found that it produced a dark horizontal band that could not be explained by my testing nor by Semrock technicians. Fortunately, the Di02 version remedied the

issue.

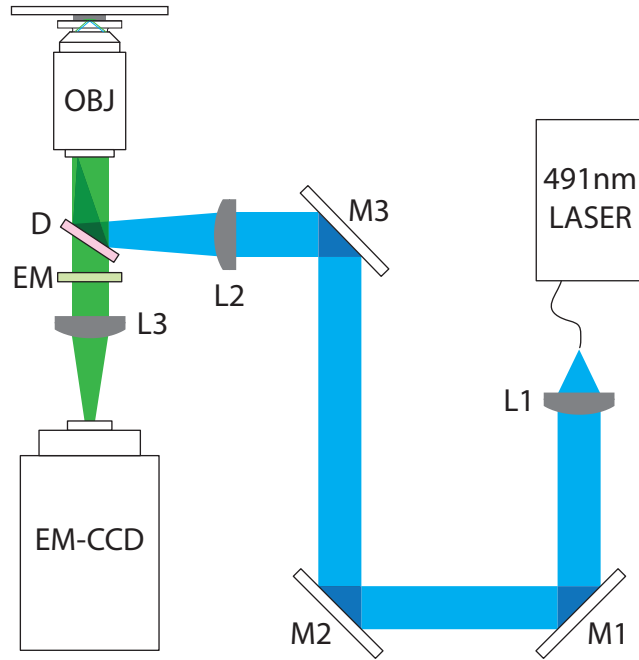


Figure 2.4: Single-color TIRF microscope design. *Components:* The beam from a 491 nm continuous wave laser is collimated by lens L1 (100 mm) and focused at the back focal plane of a 100 \times , 1.46 NA objective (OBJ) by condenser lens L2 (125 mm). A dichroic mirror (D) reflects the excitation beam into the objective, while passing emission light from the sample toward the EM-CCD camera. The emission filter (EM) passes the fluorescent signal while blocking excitation wavelengths. Optovar lens L3 provides an additional 1.6 \times magnification of the signal, which is projected onto a Hamamatsu C9100-13 EM-CCD camera. The final magnification is 101 nm/pixel. *Alignment:* Beginning in epi-fluorescence mode, TIRF is achieved by adjusting mirrors M2 and M3 simultaneously to steer the beam beyond a critical angle necessary to achieve TIRF illumination at the sample plane.

A schematic for the single-channel TIRF microscope is shown in Figure 2.4. The microscope was first aligned in epi-fluorescence mode, and then mirrors M2 and M3 were adjusted simultaneously to steer the excitation beam beyond the critical angle. One mirror was used to steer the beam while a second was used to shift the beam to prevent clipping on internal apertures or other components. To help with beam alignment, some obstructions were removed from the beam path, including an unused, internal shutter in front of the condenser lens. A 1.6 \times optovar lens was used to further

magnify the TIRF images, resulting in a final magnification of 101 nanometers per pixel, as measured by a stage micrometer.

2.3 Collection of Additional Growth Data Using Prepared Tubulin

I performed a new set of experiments using $5.6 \mu\text{M}$ of tubulin (purified and labeled in-lab) and paclitaxel concentrations ranging from 0 to 100 nM. For this data set images were captured using streaming 30-ms exposures. Frames were captured at 30-ms resolution so that fast microtubule dynamics could be measured, while still allowing for frame integration to longer intervals, if necessary. Prior to data analysis, I used a control data set to compute the growth increment variance over increasing degrees of frame integration. At low values of frame integration (e.g. 30-ms) measurement noise dominates the image signal. By employing a small amount of frame-averaging, spatial tracking resolution improves significantly; however, at long frame integration times (e.g. >2 seconds), there is additional variance from microtubule length changes. Thus, the optimal frame integration time is the amount that minimizes the increment variance (Figure 2.5). I found that variance was minimized at an integration time of ~ 1 s; however since data from collaborators indicated a lower time of 200-ms, I chose to use 480-ms intervals be sure that all dynamics would be captured.

During data collection I found that as microtubules grew longer, their tips would often diffuse in and out of the shallow evanescent field, and thus, their fluorescence would fluctuate. This would make accurate tracking impossible. Therefore, slides containing microtubules that had grown beyond $\sim 5 \mu\text{m}$, on average, were placed in a refrigerator at 4°C for about 1 minute to cold depolymerize microtubules back to the stabilized seeds. Using this technique, each slide was used for multiple rounds of polymerization for up to 45 minutes, while ensuring that growing tips were not affected

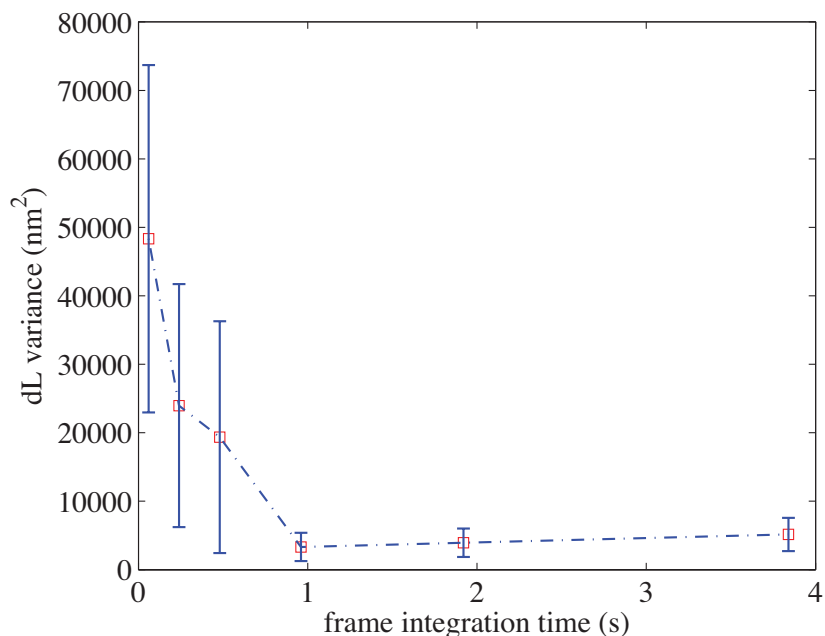


Figure 2.5: Increment variance versus frame integration time. Variance of increments dL is plotted against for increasing degrees of frame integration. Variance is minimized at ~ 1 s.

by excessive diffusion. I found that with 5 nM paclitaxel a fraction of microtubules did not depolymerize after exposure to cold temperatures, and with 10 nM paclitaxel few, if any, microtubules depolymerized after cold exposure. While these observations were not quantified, the results were consistent for all slide preparations.

Figure 2.6 shows sample length traces and kymographs from the data set. Tip tracked length data was again analyzed using a diffusion-with-drift model, and growth parameter distributions were compared for each paclitaxel condition (Figure 2.7). A multiple comparisons analysis showed that neither 5 nor 10 nM paclitaxel significantly affected the growth rate ($p = 0.22$ and 0.65 , respectively), however, 100 nM paclitaxel reduced the growth rate by 30% ($p = 2 \times 10^{-4}$). As seen in Figure 2.6 and Table 2.2 the growth rates were less variable in the present data set than in earlier studies. This was likely due, in part, to the shorter periods of data collection, which were ~ 3 minutes, compared to ~ 10 minutes for earlier studies. Since paclitaxel exhibited

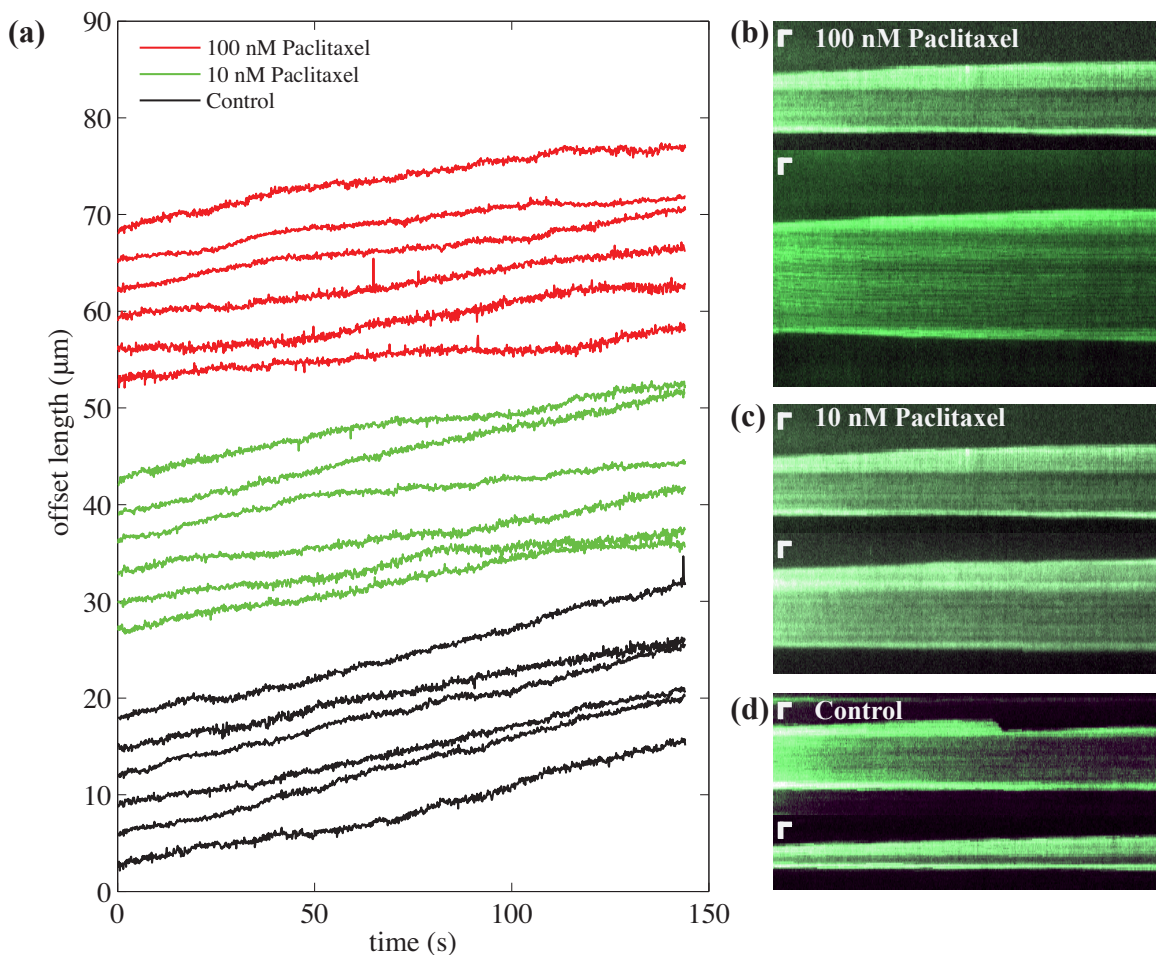


Figure 2.6: Sample microtubule length traces and kymographs from new data set. (a) Sample microtubule length traces from tip track output. Images were captured using 30-ms exposures, which were averaged to 480-ms prior to tracking. Length data is shifted vertically both within and between groups for clarity. (b-d) Sample kymographs showing growth of 20% HiLyte 488 tubulin extensions (bright green) from GMPCPP stabilized HiLyte 488 (10%) seeds (dim green) for microtubules grown with $5.6 \mu\text{M}$ tubulin and 100, 10, and 0 nM paclitaxel, respectively. No shortening events were observed during the 3-minute data acquisition time for paclitaxel microtubules, and few were observed for control microtubules. Vertical and horizontal scale bars are $1 \mu\text{m}$ and 30 seconds, respectively, for all images.

growth phases that lasted on the order of 100 seconds, these data traces may not be long enough to capture the longer term growth variability observed earlier. Still, with the large sample size in this data set, it seems likely that any differences caused by paclitaxel would be apparent. It is also possible that the tubulin contaminant found in the earlier data set may have interacted with tubulin and paclitaxel and altered the growth rate.

These new results, together with observations of paclitaxel’s ability to cold-stabilize microtubules, suggests that paclitaxel stabilizes microtubules at concentrations as low as 10 nM, but higher concentrations are necessary to reduce the growth rate. This is consistent with studies by *Derry et al.*, who found that the growth rate was unaffected by paclitaxel concentrations below 100 nM.

Table 2.2: Microtubule growth parameters using HiLyte 488 tubulin, labeled in-lab

Paclitaxel concentration, nM	Growth rate, nm/s	Diffusion coefficient, nm ² /s	On rate, s ⁻¹	Off rate, s ⁻¹	No. of observations
0	6.25 ± 0.07	58.56 ± 1.16	160 ± 3	150 ± 3	981
5	6.03 ± 0.09	60.17 ± 1.61	163 ± 4	154 ± 4	513
10	6.12 ± 0.09	55.32 ± 1.44	151 ± 4	141 ± 4	528
100	4.43 ± 0.41	40.84 ± 4.46	111 ± 12	104 ± 12	23

TIRF images were collected as 30-ms streaming exposures from microtubules grown with 5.6 μM tubulin using 0–100 nM paclitaxel. Length data was obtained by integrating frames to 480-ms and tracking microtubule tip positions using modified TipTracker code. Growth phase data was analyzed using a diffusion-with-drift model. Each observation includes growth phase data traces containing at least 20 data points (9.6 seconds).

Next, I looked at how the effective diffusion coefficient, D_p , was affected by paclitaxel. I predicted that, since low concentrations of paclitaxel render microtubules cold-stable yet do not affect the growth rate, paclitaxel must affect the subunit on and off rates ($k_{on,MT}^*$ and $k_{off,MT}$, respectively). If $k_{on,MT}^*$ and $k_{off,MT}$ were lowered

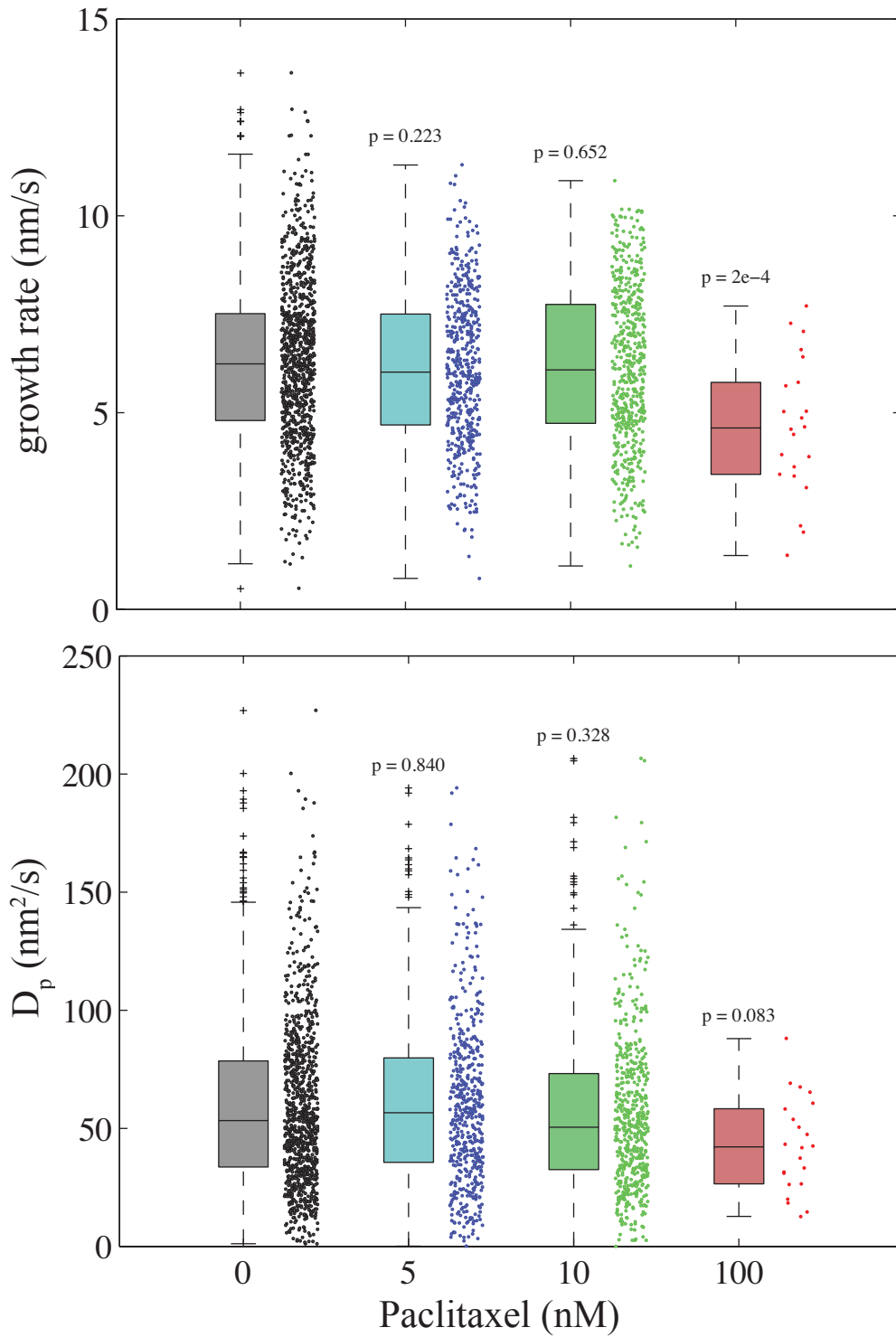


Figure 2.7: Box plots of microtubule growth parameters. Box plots showing growth rate and diffusion coefficient data for microtubules grown with $5.6 \mu\text{M}$ tubulin and 0 – 100 nM paclitaxel. P-values indicate significance levels with respect to [paclitaxel] = 0.

equally (in absolute units), then the difference between them—and v_g —would remain the same. My results show that none of the tested paclitaxel concentrations significantly affect D_p ($p = 0.84, 0.33,$ and 0.08 for $5, 10,$ and 100 nM, respectively). This result was surprising given paclitaxel’s potent inhibition of rapid shortening. Moreover, at 100 nM I expected paclitaxel’s effect on D_p to be commensurate to its effect on v_g , since the microtubule diffusion coefficient is proportional to the underlying kinetic rates. However, because of the small number of observations at 100 nM, it is possible that additional data would establish significance.

2.4 Discussion

In this chapter I have detailed several important findings related to microtubules and their interaction with the microtubule-targeting drug paclitaxel. First, because of paclitaxel’s poor aqueous solubility, stock solution must be prepared in a compatible solvent, such as DMSO or methanol. However, my results show that methanol should be avoided due to its affect on microtubule growth at concentrations as low as 0.1% , even though studies by *Derry et al.* (1995) and others (*Howarth et al.*, 1999; *Yvon et al.*, 1999) indicate that concentrations of 0.1 – 1% have no effect. Interestingly, *Yvon et al.* (1999) used methanol to prepare paclitaxel stock, and in the same study they used methanol for cell fixation, though they did not specify what concentrations were used. My controls using DMSO show that a concentration of 1% has no effect on microtubule dynamics, and thus, it is a safe alternative to methanol.

Paclitaxel was found to potently stabilize microtubules against depolymerization at low, substoichiometric concentrations. At 10 nM, microtubule dynamic instability was completely eliminated, and microtubules were cold stable at 4 °C for at least several minutes. The average growth rate and growth variance, however, were unaffected. There is some evidence that paclitaxel causes the microtubule growth rate to vary over longer time scales (Figure 2.1), though these results were obtained using a

contaminated tubulin source and may not reflect the effects of paclitaxel alone. Still, others have observed similar phases of growth attenuation (*Derry et al.*, 1995; *Yvon et al.*, 1999; *Jordan et al.*, 1993; *Madari et al.*, 2003).

Since paclitaxel stabilizes microtubules without altering the growth rate or on/off rates, then it likely causes energetic changes that affect the interaction between tubulin dimers. More work is needed to understand how this occurs, but it may be that paclitaxel slows the rate of GTP hydrolysis, which would create a perpetually stable GTP-cap. It may also strength tubulin longitudinal or lateral bonds, or may straighten the conformation of GDP-tubulin. Any of these changes could stabilize the microtubule without affecting the growth rate or kinetic rates.

CHAPTER III

Effects of Microtubule-targeting drugs on Microtubule Dynamics

Microtubules are structurally complex polymers formed by the assembly of $\alpha\beta$ -tubulin heterodimers. They are the target of a growing number of drugs used primarily to treat cancer. These microtubule-targeting drugs work by interacting with tubulin at one of four binding sites, leading to suppression of fundamental growth properties necessary for proper microtubule function. While each drug can be classified as a microtubule stabilizer or destabilizer—by promoting growth or disassembly, respectively, at higher concentrations—they all function similarly at low nanomolar concentrations by suppressing dynamic instability (*Jordan and Wilson, 2004; Dumontet and Jordan, 2010*). While this has been known for some time, the mechanistic details of how each drug affects the microtubule kinetic rates in the context of more recent work remain unknown.

Studies by *Gardner et al. (2011a)* found that microtubule growth is more variable than previously thought, and that the long-established 1D growth model (*Oosawa, 1970*) is flawed in its application to microtubule growth. Their studies are in agreement with work by *Schek et al. (2007)*, who recorded microtubule growth using optical tweezers with previously unprecedented resolution. Relevant to the current study, *Gardner et al. (2011a)* developed a diffusion-with-drift model, whereby the mi-

microtubule kinetic rates of assembly and disassembly can be estimated. They showed that microtubule growth results from the difference in large, competitive tubulin on and off rates, and that increasing tubulin concentrations lead to higher rates, and thus, higher growth variance. They also documented how fluorescence image data can be used to estimate the microtubule mean protofilament length.

In this work I aimed to use total internal reflection fluorescence (TIRF) microscopy to elucidate the mechanisms of action of four important microtubule-targeting drugs, using methods established by *Gardner et al.* (2011a). I have chosen to study therapeutic concentrations of drugs that bind to each of the four known tubulin binding sites: (1) *Paclitaxel*, which binds at the taxoid site, has been used since the early 1990s to treat lung, ovarian, and breast cancers, though treated cells are highly susceptible to P-glycoprotein-mediated resistance (*Blagosklonny and Fojo, 1999; Horwitz et al., 1992*); (2) *Peloruside A*, which binds a recently discovered tubulin site shared by laulimalide, shows promise as a paclitaxel-alternative. It remains potent in paclitaxel-resistant cells and does not require toxic solubilizing agents for clinical delivery (*Ganguly et al., 2015; Wilmes et al., 2007*); (3) *Colchicine*, which binds the colchicine site, is used in the treatment of gout and is unique in that it forms a complex with soluble tubulin dimers before adding to microtubules (*Ravelli et al., 2004*); and (4) *Vinblastine*, which binds at the vinca domain, belongs to the vinca alkaloid family of drugs, the earliest clinically used tubulin-binding chemotherapeutic agents (*Dumontet and Sikic, 1999*).

I explored how the microtubule kinetic rates were affected by clinically-relevant concentrations of each drug, and also determined how any effects are related to changes in tip structure. Results from these studies are especially relevant to clinical research, where drugs are used at the lowest efficacious doses to limit undesirable side effects.

3.1 Results

I compared the effects of individual microtubule-binding drugs on the microtubule kinetic rates, mean protofilament length, growth variance, and polymer rigidity. I also tested for synergistic effects when using peloruside A and paclitaxel in combination, as previously reported (*Wilmes et al.*, 2011; *Hamel et al.*, 2006). Microtubules were elongated from biotinylated, GMPCPP-stabilized seeds labeled with 10% HiLyte 488 tubulin at 37° C, using a range of tubulin concentrations and drug conditions. The free tubulin concentrations used in this study ranged from 3 to 14 μM , with smaller sub-ranges used for each drug. The sub-ranges were chosen such that growth was detectable, but was slow enough that several minutes of data could be recorded before microtubule ends underwent significant diffusion. All tubulin concentrations were below the threshold for spontaneous nucleation, ensuring that microtubule growth was initiated only from seed ends. Seeds were added to flow cells at low concentrations, with a final target of 20–30 bound seeds per field of view. As such, the free tubulin concentration did not significantly change over the duration of experiments, which was limited to 45 minutes. Steady-state microtubules were imaged using TIRF microscopy, and image data was captured as 240-ms streaming frames. Prior to data analysis, frames were averaged to 1.92 s in order to minimize increment variance (see Figure 3.1). Microtubules were then tracked with TipTracker software in Matlab to yield microtubule coordinates and tip displacement data.

3.1.1 Microtubule Growth Rate Model

To understand how the microtubule growth rate is affected by microtubule-binding drugs and to make predictions for guiding future experiments, I developed a microtubule growth model to relate the growth rate to tubulin concentration and drug conditions. The basis of the model is the Michaelis-Menten equation, which relates

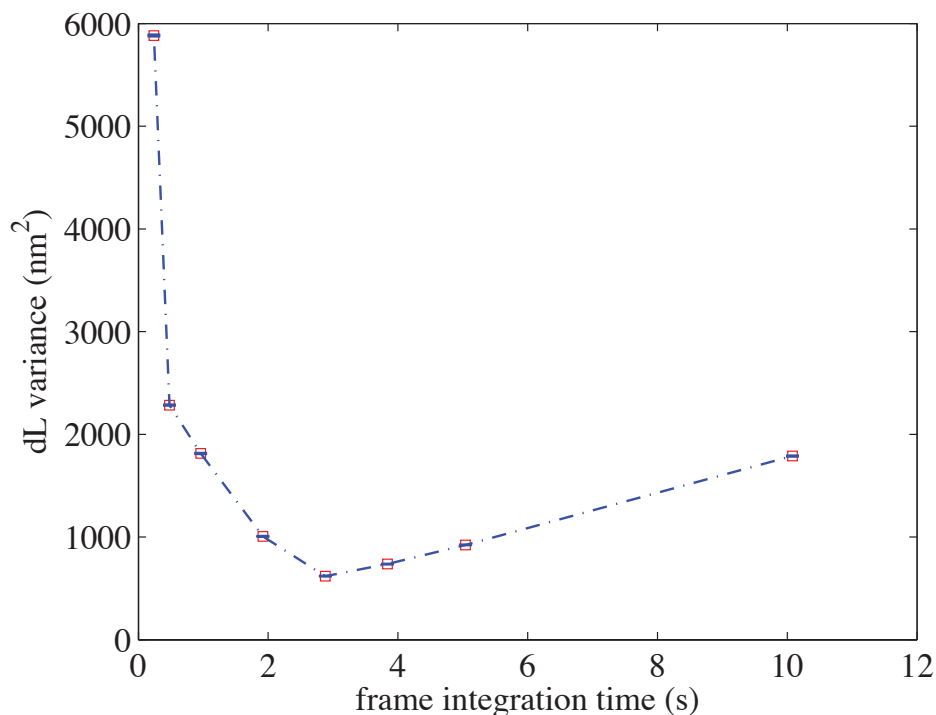


Figure 3.1: Microtubule increment variance versus time interval. Variance of microtubule growth increments (dL) plotted against frame integration time, using data from 44 control microtubules grown with $5.6 \mu\text{M}$ tubulin. Microtubule image data was integrated to 1.92 s to reduce noise and increase tracking resolution. At short integration times measurement noise dominates, and at long integration times microtubule length changes lead to additional variance. An optimal frame integration time is that which yields a minimum increment variance. This maximizes tracking performance without averaging over resolvable microtubule length changes. Error bars represent standard error.

an enzymatic reaction rate to the substrate concentration:

$$v = \frac{V_{max} [S]}{K_M + [S]} \quad (3.1)$$

where v is the reaction rate, V_{max} is the maximum reaction rate achieved at saturating substrate concentrations, and the Michaelis constant, K_M , is the substrate concentration yielding a reaction rate of $v = V_{max}/2$. *Zanic et al.* (2013) modified the Michaelis-Menten equation to describe the effects of microtubule-associated proteins EB1 and XMAP215 on microtubule polymerization. Here, the model is adapted

to describe the individual and synergistic effects of microtubule-targeting drugs on the growth rate. The numerator in Equation 3.1 describes the linear relationship between v and $[S]$ for $[S] \ll K_M$, and the denominator causes v to saturate when $[S] \gg K_M$. For each drug I added a term to the numerator to account for its effect on the growth rate, and also added an accompanying term to the denominator to describe the saturation of effects by each drug:

$$v = \frac{\frac{\alpha}{K_T}[T] \left(1 + \frac{\beta_1}{K_X}[X] + \frac{\beta_2}{K_P}[P] + \frac{\beta_3}{K_C}[C] + \frac{\beta_4}{K_V}[V] \right)}{1 + \frac{1}{K_X}[X] + \frac{1}{K_P}[P] + \frac{1}{K_C}[C] + \frac{1}{K_V}[V]} \quad (3.2)$$

where $[T]$, $[X]$, $[P]$, $[C]$, and $[V]$ are the concentrations of tubulin, paclitaxel, peloruside A, colchicine, and vinblastine, respectively; $\frac{\alpha}{K_T}$ is equivalent to V_{max} for tubulin alone; K values are the corresponding Michealis constants for each drug; and β values are additional scaling parameters. Lastly, I added similar terms to describe the interaction between drugs when used in combination with one another. In this study, the only drug interaction tested was that between paclitaxel and peloruside A. Therefore, for clarity only relevant drug interaction terms are shown:

$$v = \frac{\frac{\alpha}{K_T}[T] \left(1 + \frac{\beta_1}{K_X}[X] + \frac{\beta_2}{K_P}[P] + \frac{\beta_3}{K_C}[C] + \frac{\beta_4}{K_V}[V] + \frac{\gamma_1}{K_X K_P}[X][P] \right)}{1 + \frac{1}{K_X}[X] + \frac{1}{K_P}[P] + \frac{1}{K_C}[C] + \frac{1}{K_V}[V] + \frac{\gamma_2}{K_X K_P}[X][P]} \quad (3.3)$$

where γ_1 and γ_2 are scaling constants.

Model parameters in Equation 3.3 were fit using experimental data. Since tubulin-binding drugs can affect both the microtubule growth rate and the tubulin critical concentration (the minimum concentration necessary for polymerization), data sets were shifted such that critical concentrations aligned at 0 μM . This was done first by performing linear regressions to find the slopes and y-intercepts of growth rate versus [tubulin] for each data set (a data set is one drug condition across multiple tubulin concentrations). Then, the tubulin critical concentration (the x-intercept)

was calculated, and data sets were shifted along the [tubulin] axis to x-intercepts of 0 μM . In this way, data sets are “normalized” by their respective critical concentrations, so that growth rate concentration dependence could be directly compared.

The shifted data sets were then imported into Matlab and all data was simultaneously fit using the “*nlinfit*” function, and 95% confidence intervals were obtained using the function “*nlparci*” (Table 3.1). All parameters were significantly different from zero at the 95% confidence level except for γ_1 , γ_2 , and β_1 . A lack of significance in γ_1 and γ_2 indicates that no growth rate synergy was detected between paclitaxel and peloruside A, and β_1 showed no significance due to a lack of paclitaxel concentration dependence between 10 and 100 nM. Figure 3.2 shows the model predictions (lines) overlaid with experimental data (points) at corresponding drug conditions.

Table 3.1: Growth Model Parameters

Parameter	Value
α/K_T	1.50 ± 0.03 [nm/s]
β_1	0.74 ± 0.10
β_2	$(5.4 \pm 0.0) \times 10^8$
β_3	$(-6.7 \pm 0.4) \times 10^6$
β_4	0.19 ± 0.02
K_X	0.04 ± 4.18 [nM]
K_P	$(1.1 \pm 0.1) \times 10^{12}$ [nM]
K_C	$(6.5 \pm 0.0) \times 10^9$ [nM]
K_V	43 ± 0 [nM]

Parameter estimates for the growth rate model (Equation 3.3) fit using the “*nlinfit*” function in Matlab. Errors are 95% confidence intervals.

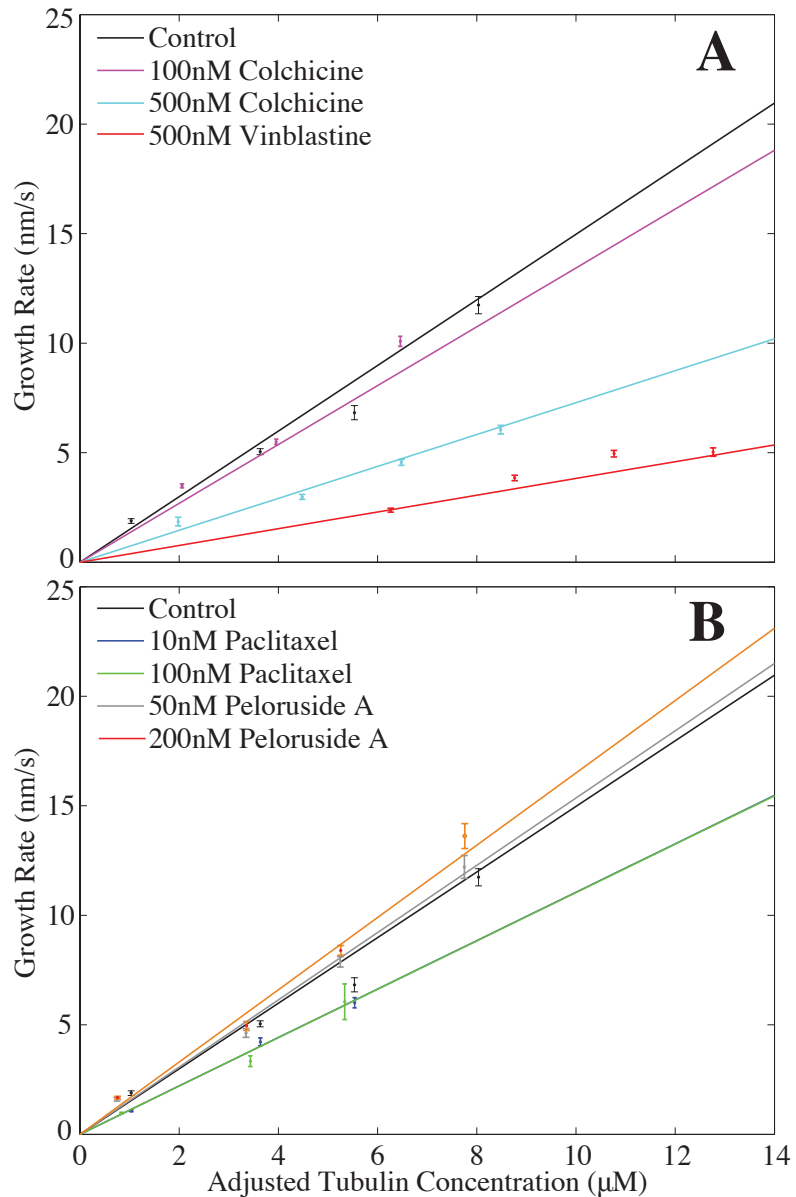


Figure 3.2: Microtubule growth rate model predictions. Tubulin concentrations for each data set were adjusted by determining the tubulin critical concentrations (x-intercepts) and shifting data to critical concentrations of $0 \mu\text{M}$. Model parameters were then fit using data from all conditions at once. Colored lines represent the model predictions for the indicated drug conditions, and points represent experimentally-determined rates. Plots are separated, for clarity, by drugs classically defined as microtubule destabilizers (A) and stabilizers (B). Note that both paclitaxel curves are coincident.

3.1.2 Colchicine and Vinblastine Stabilize Microtubules by Suppressing the Kinetic Rate Constants

To find out how assembly- and disassembly-promoting microtubule-targeting drugs affect the kinetic rates of tubulin association and dissociation, I first examined the microtubule destabilizing drugs colchicine and vinblastine at nanomolar concentrations by comparing the net growth rate (v_g) over a range of tubulin concentrations. In the case of 1D polymerization, the kinetics rates can be determined from the slope and intercept of v_g versus [tubulin] (*Oosawa*, 1970), however, as discussed earlier, the 1D model cannot be applied to microtubule polymerization due to the interdependence of growth rates between adjacent protofilaments (*VanBuren et al.*, 2002; *Gardner et al.*, 2011a). Despite this, the slope of v_g versus tubulin concentration still provides useful information about the relative dependence of growth rate on the tubulin concentration. For example, a steep slope would indicate a strong dependence of v_g on the tubulin concentration and, based on previous work, would also suggest large subunit on and off rates. Conversely, a shallow slope would indicate a lower dependence on [tubulin] and smaller rate constants.

Figure 3.3A shows sample length traces of microtubules growth using 7.5 μM tubulin with colchicine and vinblastine. (*Note that since all microtubule-targeting drugs were tested at an overlapping tubulin concentration of 7.5 μM , I use that as a representative concentration for reporting my results, though the observed trends extend to other tubulin concentrations.*) While 100 nM colchicine had little effect on the growth rate, addition of 500 nM colchicine or vinblastine led to a powerful suppression of the growth rate. Catastrophe events were still detected, though length changes during rapid shortening events were much smaller, and phases of growth and shortening became largely indistinguishable. At 7.5 μM tubulin with 500 nM of either drug, microtubules would often grow less than a micron off of the stabilized seed before completely depolymerizing. At higher tubulin concentrations (not shown)

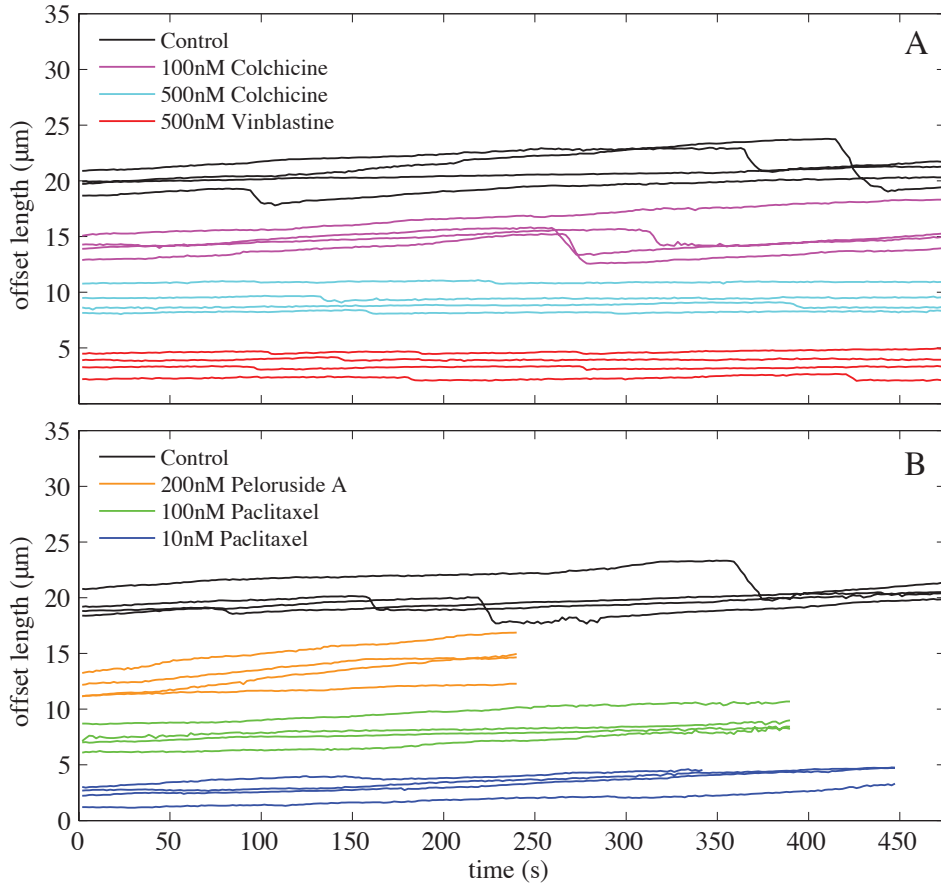


Figure 3.3: Sample length traces for microtubules grown with $7.5 \mu\text{M}$ tubulin and various drugs. All drugs suppressed microtubule dynamics at nanomolar concentrations. *Panel A:* 500 nM of colchicine or vinblastine reduced the net growth rate and appeared to increase the catastrophe frequency. *Panel B:* Paclitaxel and peloruside A marginally decreased and increased the growth rate, respectively, and completely suppressed detectable shortening events over the duration of experiments. Note that length traces are shifted along the length axis for clarity. Most catastrophe events resulted in shortening back to the stabilized seed.

microtubules grew longer before shortening.

I compared the slope of v_g versus [tubulin] for microtubules grown in the absence and presence of either colchicine or vinblastine at 500 nM and found that both strongly reduced the slope, and thus, reduced the underlying rates of tubulin addition and loss (Figure 3.2). 100 nM colchicine was also tested but did not significantly alter the slope. Since colchicine first forms a complex with tubulin before binding microtubules (*Ravelli et al.*, 2004), this indicates that the binding constant for colchicine to tubulin may be in the range of 100–500 nM. While 100 nM colchicine had little effect on the slope, 500 nM colchicine reduced the slope by nearly 50%, and an equal concentration of vinblastine reduced the slope by 70%.

To estimate the kinetic rates of tubulin association and dissociation ($k_{on,MT}^*$ and $k_{off,MT}$, respectively) I used a diffusion-with-drift model, which relates the mean squared growth increments to growth parameters v_g and D_p (Equation 3.4; see Chapter 1). Once v_g and D_p are determined from the model fit, Equations 3.5 and 3.6 can be used to calculate the tubulin association and dissociation rates:

$$\langle \Delta L^2 \rangle = v_g^2 \Delta t^2 + 2D_p \Delta t + \sigma^2 \quad (3.4)$$

$$k_{on,MT}^* = \frac{D_p}{\alpha_{MT}^2} + \frac{v_g}{2\alpha_{MT}} \quad (3.5)$$

$$k_{off,MT} = \frac{D_p}{\alpha_{MT}^2} - \frac{v_g}{2\alpha_{MT}} \quad (3.6)$$

I calculated the tubulin on and off rates for control microtubules and compared them with values from microtubules grown with colchicine and vinblastine. Because of unequal variances, statistics were performed on square-root transformed data. I found that colchicine and vinblastine both potently suppressed $k_{on,MT}^*$ and $k_{off,MT}$ at 500 nM, nearly eliminating microtubule dynamics (Figure 3.4). 500 nM colchicine reduced the tubulin on and off rates by $\sim 85\%$ ($p = 1 \times 10^{-8}$), and 500 nM vinblastine

reduced the rates by $\sim 60\%$ ($p = 2 \times 10^{-3}$). The microtubule growth rates were also fit using the model, and interestingly, even though colchicine had a more potent effect on the kinetic rates compared to vinblastine, it had less of an effect on the growth rate. 500 nM colchicine and vinblastine reduced the growth rate by 68% ($p = 1 \times 10^{-8}$) and 75% ($p = 1 \times 10^{-8}$), respectively (see Table 3.2).

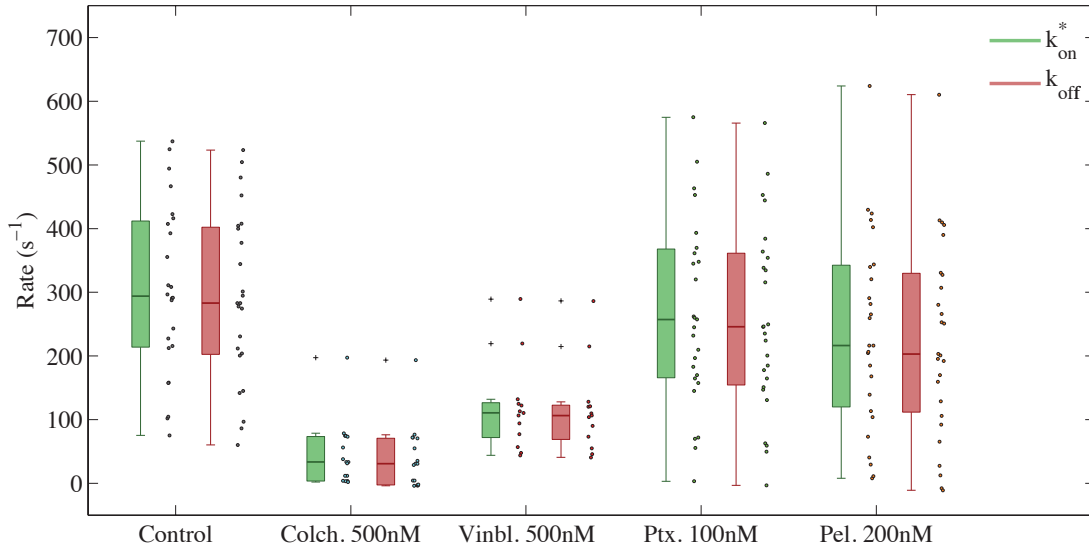


Figure 3.4: Effects of microtubule-targeting drugs on the tubulin on and off rates. Microtubule growth increments were fit using a diffusion-with-drift model, from which on and off rates were estimated. Colchicine and vinblastine potently suppress the kinetic rates, while paclitaxel and peloruside A have no significant effect.

Table 3.2: Model estimates of microtubule growth parameters

Drug condition	Growth rate, nm/s	p-value	On rate, s^{-1}	Off rate, s^{-1}	p-value
Control	8.0 ± 0.5	–	304 ± 27	291 ± 27	–
500nM Colch.	2.6 ± 0.3	1×10^{-8}	43 ± 12	39 ± 12	1×10^{-8}
500nM Vinbl.	2.0 ± 0.2	1×10^{-8}	118 ± 19	115 ± 19	2×10^{-3}
100nM Ptx.	6.2 ± 0.4	0.02	281 ± 33	271 ± 33	0.93
200nM Pel.	8.0 ± 0.5	1.0	257 ± 36	244 ± 36	0.53

Microtubule growth rates and tubulin on and off rates were estimated using a diffusion-with-drift model. Statistics were performed on square-root transformed data, collected using $7.5 \mu\text{M}$ tubulin.

3.1.3 Paclitaxel and Peloruside A Stabilize Microtubules without Altering the Kinetic Rates

I performed a similar analysis of the assembly-promoting microtubule-binding drugs paclitaxel and peloruside A, which, in contrast to vinblastine and colchicine, have been shown to increase polymer mass at higher concentrations (*Dumontet and Jordan, 2010*). Because of the difference in their mechanism of action at high concentrations, I expected to see a difference in their effects on the growth and kinetic rates, compared to the microtubule destabilizing drugs colchicine and vinblastine. As shown in Figure 3.3B, catastrophe events and shortening were completely suppressed by low concentrations of paclitaxel and peloruside A. The paclitaxel results are consistent with my previous findings, though somewhat surprising given that a recent *in vitro* study by *Mohan et al. (2013)* detected a number of shortening events when using 50 nM paclitaxel.

I found that neither of the tested concentrations of peloruside A significantly affected the slope of v_g versus [tubulin]. However, addition of 10 and 100 nM paclitaxel led to a modest decrease in the slope (see Figure 3.2B). The overlap in growth rate data for 10 and 100 nM paclitaxel suggests that growth rate effects by the drug are saturated by 10–100 nM. However, studies have shown that paclitaxel’s effect on microtubule growth is complicated and may change at super-micromolar concentrations (*Derry et al., 1995*), though such levels are beyond the realm of clinical significance.

I next analyzed growth data using a diffusion-with-drift model to estimate $k_{on,MT}^*$, $k_{off,MT}$, and v_g . Results from the analysis are summarized in Figure 3.4 and Table 3.2. Neither 100 nM paclitaxel nor 200 nM Peloruside A significantly affected the growth rate or subunit kinetic rates ($p > 0.01$). Despite their modest effects on the growth rate and kinetics rates, I observed that 10 nM paclitaxel and 50 nM peloruside A eliminated dynamic instability and rendered microtubules stable against cold-induced depolymerization at 4 °C. These results suggest that stabilization may

occur via changes in the lateral or longitudinal bond energies, or in the hydrolysis-coupled $\alpha\beta$ subunit strain energy (*VanBuren et al.*, 2002; *Castle and Odde*, 2013) in such a way that the rates of subunit assembly and disassembly are preserved.

I wanted to understand how paclitaxel and peloruside A could stabilize microtubules against depolymerization without significantly altering the microtubule rate constants. To further investigate their effects I compared the variance in microtubule growth increments ($\text{var}\{\Delta L\}$) for different drug conditions.

If $\langle\Delta L\rangle = 0$, then $\langle(\Delta L)^2\rangle \equiv \text{var}\{\Delta L\}$; that is, if the mean of increment displacements is zero, then the variance of those increments is equal to their mean square displacement. Therefore, $\text{var}\{\Delta L\} = 2D\Delta t$ (*Gillespie and Seitaridou*, 2012). Microtubule length displacements, however, are biased via the net growth rate. If the slope of the net growth rate is subtracted from respective length versus time traces, then values of ΔL can be computed such that $\langle\Delta L\rangle = 0$, allowing the effective diffusion coefficient, D_p , to be calculated. Theoretically, this method should result in the same fit of D_p as the diffusion-with-drift analysis.

I used this increment variance method to directly calculate the effective diffusion coefficients for various drug conditions. I first performed linear regressions for each microtubule growth trace to find average growth rates (v_g) and then subtracted v_g values from respective length traces. Next, I calculated the variance of growth increments (ΔL), measured over increasing time intervals (Δt). The slope of increment variance versus time interval is equal to $2D_p$, and therefore provides an estimate of D_p .

Table 3.3 shows values of the subunit on and off rates, which were calculated using Equations 3.5 and 3.6, using increment variance estimates of D_p , and linear regression estimates of v_g . Estimates of growth rates match values determined from the diffusion-with-drift model; however, the estimates of subunit on and off rates are 20–50% higher than those fit by the diffusion-with-drift model. Interestingly,

Table 3.3: Microtubule growth parameters estimated from increment variance

Drug condition	Growth rate, nm/s	On rate, s ⁻¹	Off rate, s ⁻¹
Control	8.0 ± 0.3	363 ± 5	349 ± 5
100nM Ptx.	6.7 ± 0.4	357 ± 7	346 ± 7
200nM Pel.	8.1 ± 0.3	387 ± 7	373 ± 7

Microtubule growth rates and subunit on and off rates calculated from unbiased microtubule growth increments.

results using the increment variance method show that peloruside A increases the tubulin kinetic rates, whereas the diffusion-with-drift model indicates that the rates are lowered by peloruside A.

To compare both analysis methods directly, I generated synthetic growth data using defined values for variance and assembly and disassembly rates. Each simulated microtubule started at a length of zero, and assembly rates k_{on}^s and k_{off}^s were defined as

$$k_{on}^s = R(\sigma^2)^{1/2} + k_{on}^* \quad (3.7)$$

$$k_{off}^s = R(\sigma^2)^{1/2} + k_{off} \quad (3.8)$$

where R is a uniformly distributed random number between 0 and 1, σ^2 is the defined variance, and k_{on}^* and k_{off} are the defined rates of subunit assembly and disassembly, respectively.

I simulated populations of microtubules and incremented either k_{on}^* and k_{off} or σ^2 . Since the growth rates for microtubules grown in the presence of paclitaxel or peloruside A are similar to controls, the difference of $k_{on}^* - k_{off}$ was maintained at a constant value. Using both the diffusion-with-drift and increment variance methods to analyze the data, I found that each method produced identical values of k_{on}^* , k_{off} , and v_g , a result that matches theoretical expectations. I believe that the discrepancy in results when applying these methods to experimental data arises from the difficulty

in fitting the diffusion-with-drift equation. The contribution from the diffusion term to the full quadratic model equation is very small except at low Δt . For longer data traces, improving the fit of the quadratic seems to favor the drift term (v_g), possibly at the expense of the diffusion term D_p . Thus, small changes in v_g can significantly affect estimates of the on/off rates. Additional simulations comparing both methods may provide clarity.

3.1.4 Microtubule Protofilament Taper Lengths Are Gamma-distributed

Prior analysis of microtubule tip structure using cryo-electron microscopy has shown that the protofilament taper length increases at higher tubulin concentrations (*Chrétien et al.*, 1995). More recent work has demonstrated that the taper lengths can be estimated using fluorescence microscopy by measuring the standard deviation in the fit of the microtubule tip position (*Gardner et al.*, 2011a). A large standard deviation value (σ_{tip}) corresponds to a highly tapered protofilament structure, while a smaller σ_{tip} indicates a blunt tip with protofilaments of similar length. I wanted to know if microtubule-binding drugs affect tip structure, and whether any effects are correlated with a drug's classification as a stabilizer or destabilizer. I analyzed protofilament length data for various drug conditions at a constant tubulin concentration of 7.5 μM . My results show that microtubule destabilizers colchicine and vinblastine lower the mean of σ_{tip} . At 500 nM, colchicine reduced the average σ_{tip} from 177 ± 2 to 85 ± 28 nm, and equal concentration of vinblastine reduced σ_{tip} to 90 ± 1 nm. The effects from microtubule stabilizers paclitaxel and peloruside A, however, were more subtle (see Figure 3.5).

Despite some differences in the mean tip taper lengths of microtubules, it was difficult to make comparisons between conditions since the distributions are not normal (see data in scatter plots of Figure 3.5). After trying several methods, including various data transformations, I found that the data was best fit with a gamma distri-

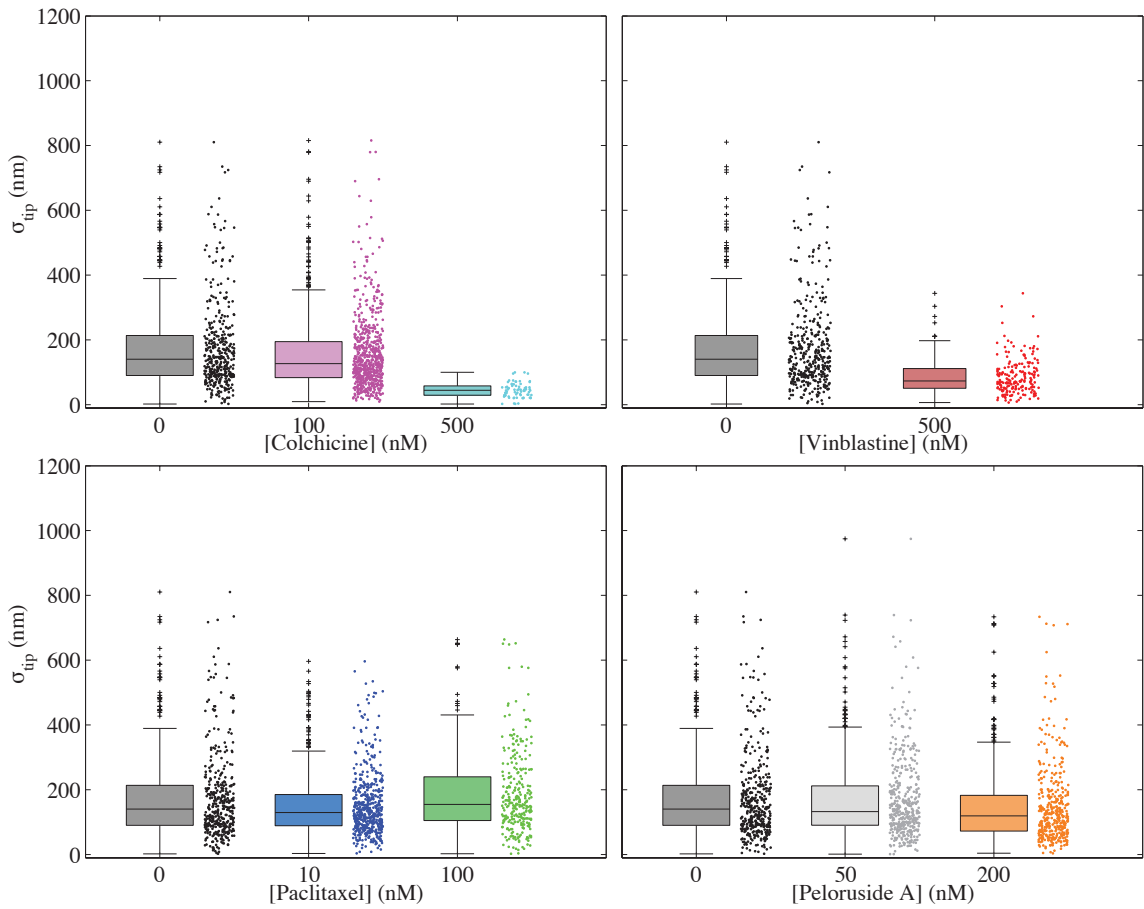


Figure 3.5: Box plots of microtubule protofilament lengths. Data is shown for microtubules grown using $7.5 \mu\text{M}$ tubulin and various drug conditions.

bution. This is interesting since recent work by *Gardner et al.* (2011b) showed that microtubule catastrophe times are also described by a gamma distribution (see also *Odde et al.* (1995)). It had previously been assumed that catastrophe was a single step process, where the catastrophe frequency is independent of microtubule age (*Howard et al.*, 2001); however, data from *Gardner et al.* (2011b) showed a non-linearity in the cumulative distribution of catastrophe events. Upon fitting gamma distribution parameters using catastrophe time data, they found that the step parameter (k) was >1 over a range of tubulin concentrations, indicating that catastrophe is a multi-step process. The definition of these steps is somewhat ambiguous, but they could be the number of accumulated defects in the microtubule lattice or at the tip.

I performed a similar analysis of my σ_{tip} values to determine the equivalent gamma distribution parameters for each drug condition. The probability density function of the gamma distribution is given by:

$$\frac{1}{\Gamma(k)\theta^k} x^{k-1} e^{-x/\theta} \quad (3.9)$$

with mean and variance defined by:

$$\begin{aligned} E[X] &= k\theta \\ \text{Var}[X] &= k\theta^2 \end{aligned} \quad (3.10)$$

for a random variable x , where k is the step parameter, and θ is the scale parameter, which is the inverse of the rate parameter used by *Gardner et al.* (2011b). Parameters were estimated by bootstrapping σ_{tip} distributions and using Equations 3.10 to determine parameters k and θ . Bootstrap sample sizes were chosen based on an estimate of the number of independent observations, which was determined from the autocorrelation time of a σ_{tip} time series. Resulting parameter estimates are shown in Figure 3.6.

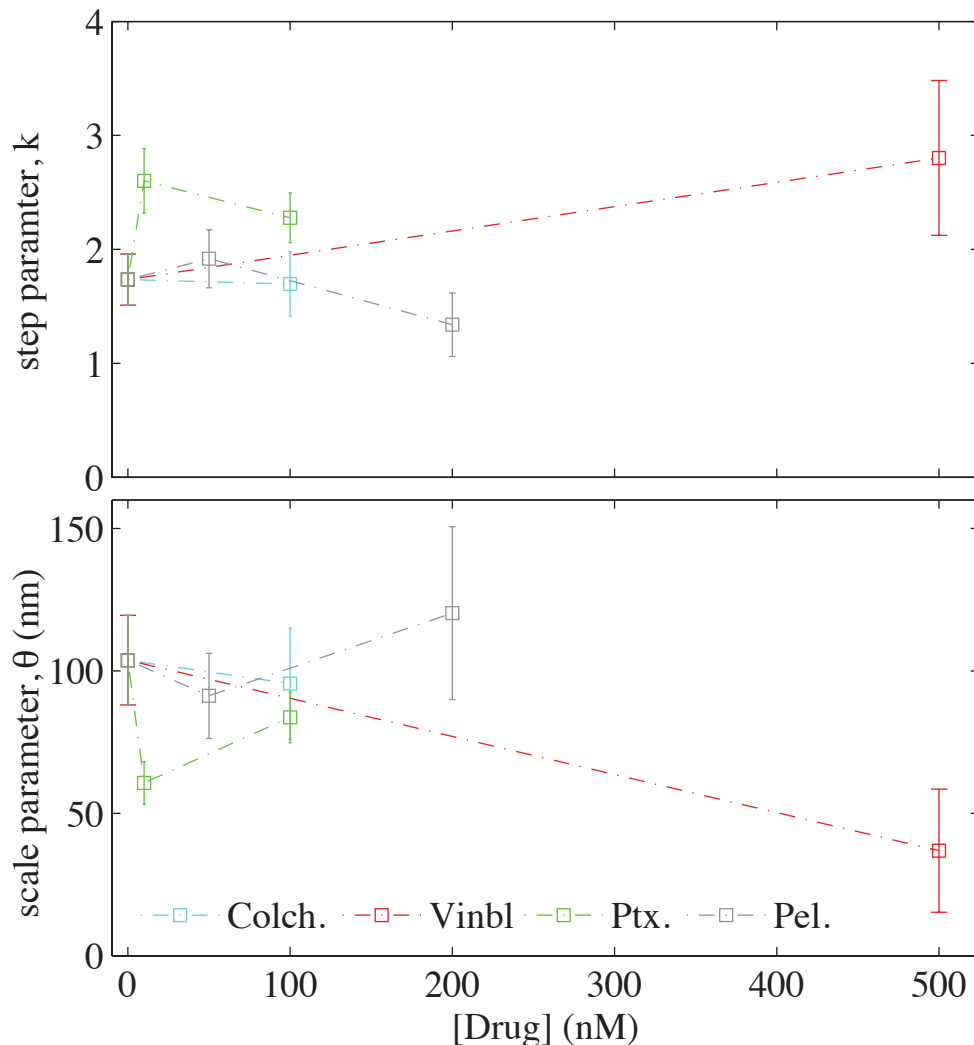


Figure 3.6: Estimates of gamma distribution step and scale parameters using microtubule tip structure data. Step (k) and scale (θ) parameters were calculated by bootstrapping σ_{tip} distributions, using a sample size corresponding to the number of independent observations, which was determined from the autocorrelation time of a σ_{tip} time series. Bootstrapped distributions were used to calculate k and θ using Equations 3.10. 500 nM colchicine data did not fit well to a gamma distribution—likely due to a small sample size—and was therefore excluded from analysis. Error bars represent standard error of the bootstrap distribution.

Statistical analysis indicates neither the step nor the scale parameters were significantly affected by changes in drug concentration ($p > 0.01$). Interestingly, though, values for both parameters fall within the range of those determined by *Gardner et al.* (2011b), which may suggest a link between tip structure and catastrophe times. Since catastrophe events are rare in the first few minutes of microtubule growth, it's possible that an accrual of defects at the microtubule tip causes the tip structure to slowly evolve in a way that increases the probability of catastrophe. A combination of further experimental studies and related modeling (e.g. *Bowne-Anderson et al.* (2013)) will be necessary to understand the link between changes in tip structure and catastrophe.

3.1.5 Microtubule Rigidity

Paclitaxel is known to affect microtubule rigidity with a majority of studies indicating that it reduces flexibility (*Gittes et al.*, 1993; *Pampaloni et al.*, 2006). Previous work has quantified microtubule rigidity using a variety of methods, including analysis of bending due to hydrodynamic flow, thermal fluctuations, and exertion of force by optical tweezers (*Hawkins et al.*, 2010). I wondered if changes in rigidity were associated with a drug's classification as a stabilizer or destabilizer, or whether the rigidity could be a measure for selecting efficacious chemotherapy drugs. To investigate the effect of microtubule-targeting drugs on microtubule rigidity, I used microtubule backbone data from tip tracking analysis, which provides microtubule lattice coordinates for each video frame. By adjusting the tip tracking code to output coordinates of freely fluctuating microtubule ends—the portions extending off of cover slip-bound seeds—I was able to capture backbone data for growing microtubules with one end clamped at the GMPCPP-stabilized seed and one free end undergoing thermal fluctuations.

Janson and Dogterom (2004) analyzed thermally-driven, growing microtubules that were clamped at one end by modifying a previously developed bending mode analysis (*Wiggins et al.*, 1998). The microtubule shape was described using a function of sines and cosines as:

$$W_n(\alpha) = \frac{-\cosh q_n - \cos q_n}{\sin q_n + \sinh q_n} (\sin q_n \alpha - \sinh q_n \alpha) + \cos q_n \alpha - \cosh q_n \alpha \quad (3.11)$$

where solutions to parameters q_n are given by

$$\cos q_n \cosh q_n = -1 \quad (3.12)$$

and $\alpha = s/L$, where s is the path length along the microtubule beginning at the end of the cover slip-bound seed ($s = 0$) and L is the full microtubule length from $s = 0$ (see Figure 3.7).



Figure 3.7: Microtubule bending mode analysis coordinate system. Image from *Janson and Dogterom* (2004).

The amplitudes of each bending mode are calculated by

$$\tilde{a}_n = \sqrt{\frac{1}{\tilde{L}}} \int_{s=0}^{\tilde{L}} y(s) W_n\left(\frac{s}{\tilde{L}}\right) ds \quad (3.13)$$

where \tilde{L} signifies that analysis of the growing microtubule is performed out to a fixed distance $s = \tilde{L}$, termed the “analyzed length” ($\tilde{L} < L$ for all frames). The variances

of the mode amplitudes, $\tilde{\sigma}_n^2$, are then calculated by

$$\tilde{\sigma}_n^2 = \frac{1}{L_p} \left(\frac{\tilde{L}}{q_n} \right)^4 \quad (3.14)$$

where L_p , the persistence length, is a measure of microtubule rigidity. If Equation 3.14 is rearranged as follows:

$$\tilde{L}^{-4} \tilde{\sigma}_n^2 = L_p^{-1} q_n^{-4} \quad (3.15)$$

then plotting $\tilde{L}^{-4} \tilde{\sigma}_n^2$ against q_n on a log-log scale will yield data with a slope of -4 and an intercept of L_p^{-1} at $q_n = 1$.

I used this bending mode analysis to estimate the persistence length of microtubules grown in the presence and absence of microtubule-binding drugs. In general, microtubule tips in my assays could only be tracked reliably out to 3–4 microns from the seed end. Beyond this range, thermal fluctuations caused significant bending of the microtubule tip away from the cover glass surface and out of the shallow evanescent excitation field. Despite testing a variety of data sets, and using a range of analysis lengths, I was unable to reproduce the 4th power dependence of $\tilde{L}^{-4} \tilde{\sigma}_n^2$ on q_n^{-4} as described in Equation 3.15. My data consistently yielded a slope of -1, which is four times smaller than the theoretical expectation and indicated that my microtubules were three order of magnitude stiffer than expected.

To understand this discrepancy, I used the model with published values of microtubule persistence lengths to generate synthetic microtubule backbone data. Upon comparing the simulated data to my experimental data, I found that simulated microtubules of similar length underwent a larger range of tip deflections. I then overlaid the bending mode fit onto my experimental data and noticed that the model seemed to fit noise within relatively straight sections of microtubules.

It's possible that these issues were due to differences in experimental methods. For example, *Janson and Dogterom* (2004) constrained microtubules from diffusing

in the z -direction (into the sample along the optical axis) by creating sample chambers of 1 μm depth, compared to my flow cells, which were $\sim 100 \mu\text{m}$ deep. Because of the shallow excitation depth in TIRF microscopy, diffusion of microtubules in the z -direction could have caused increased measurement noise, due to them fluctuating out of the evanescent region. Moreover, I used a different backbone tracking algorithm, which may not be suitable for use with a bending mode analysis.

3.2 Discussion

Results from this study show that the microtubule-destabilizing drugs colchicine and vinblastine strongly reduce the microtubule growth rate by lowering the underlying kinetics rates of subunit assembly and disassembly. Growth rates were suppressed to such an extent that the tubulin concentration must be roughly doubled to achieve rates similar to control. In contrast, the microtubule-stabilizing drugs paclitaxel and peloruside A caused only modest changes to the growth rate and subunit assembly rates. Further studies are necessary to completely understand how paclitaxel and peloruside A are able to powerfully stabilize microtubules at concentrations as low as 10 nM while minimally affecting other growth parameters.

Simulations performed by the David Odde lab (University of Minnesota), together with results presented in this study, suggest that microtubule-targeting drugs kinetically stabilize microtubules in two distinct ways. The first suggested mechanism is true-kinetic-stabilization, where the subunit on and off rates are suppressed. This leads to lower growth rates and a loss of dynamic instability. True kinetic stabilization is characteristic of microtubule-destabilizers, such as colchicine and vinblastine.

The second proposed mechanism of stabilization is pseudo-kinetic-stabilization, characterized by a thermodynamic convergence of the GTP-tubulin and GDP-tubulin states. Simulations, *in vivo*, and *in vitro* data suggest that drugs like paclitaxel may facilitate this energetic convergence. An expanded study of other microtubule

stabilizers and destabilizers will be necessary to build a robust model.

Lastly, though this study found no detectable synergy between paclitaxel and peloruside A, it is important to note that many, if not all, published studies indicating synergy were performed *in vivo*. Thus, additional variables, such as tubulin mass action or interaction with microtubule-associated proteins, may affect drug behavior. More likely, however, is that paclitaxel and peloruside may synergistically shift the tubulin critical concentration, leading to spontaneous nucleation. Since my work was performed well below the threshold for nucleation—even with added drugs—no synergy could have been detected. Additional studies closer to the critical concentration may provide insight into drug interactions.

CHAPTER IV

Estimation of Flutax-2 Kinetics Using TIRF-FRAP

Paclitaxel is a potent chemotherapy drug that has seen wide clinical use for decades. While effective against certain cancers, its use is often limited by toxicity in noncancerous tissues, which leads to many undesirable side effects. Furthermore, paclitaxel's solubilizing delivery vehicle, Cremophor EL, causes additional adverse effects in patients, and drug resistance is common (*Kanakkanthara et al.*, 2011; *Rowinsky et al.*, 1990). Because of these issues, significant research efforts have focused on the development of similar drugs that are effective against cancerous cells while having milder side effects.

In pursuit of this goal, it is necessary to identify novel drug candidates and their tubulin binding sites, so that they can be further screened for desirable properties. For example, the epothilones, which display paclitaxel-like activity, bind to the paclitaxel site and were found to be 30 times more water soluble than paclitaxel, eliminating the need for harmful solubilizing agents (*Julien and Shah*, 2002). Furthermore, epothilones retain efficacy in cells that express P-glycoprotein-mediated paclitaxel resistance. Similarly, the drug candidate discodermolide is predicted to be 100-fold more water soluble than paclitaxel and a poor substrate for P-glycoprotein (*Balachandran et al.*, 1998; *Martello et al.*, 2000).

To determine whether tubulin-binding drugs bind at the paclitaxel site, many studies have used the fluorescent paclitaxel derivatives Flutax-1 and Flutax-2 in competitive binding assays, typically using anisotropy measurements (*Díaz et al.*, 2000; *Buey et al.*, 2004; *Díaz et al.*, 2003). *Buey et al.* (2004) prepared crosslinked microtubules and measured the displacement of Flutax-2 by various paclitaxel-site ligands. By measuring changes in Flutax-2 anisotropy they were able to estimate equilibrium constants for competing ligands.

Díaz et al. (2003) also used competitive binding assays to measure the kinetics of Flutax-1, Flutax-2, and paclitaxel binding to crosslinked microtubules. The authors used a stopped flow device with a fluorescence detection system to measure small changes in the fluorescence intensity of solution due to the binding and unbinding of Flutax from a known number of paclitaxel sites. Using these and additional fluorescence polarization measurements, they estimated equilibrium constants for each of the ligands. Exchange kinetics were also measured from the displacement of Flutax-2 by docetaxel from PtK2 cell cytoskeletons using epifluorescence microscopy.

Krouglova et al. (2004) used fluorescence correlation spectroscopy to measure the diffusion coefficients of Flutax-2 and tubulin-Flutax-2 complex in solution. To study tubulin-Flutax-2 interaction, 13 nM Flutax-2 was added to increasing concentrations of unlabeled tubulin, and then the diffusion coefficient of the complex was measured. Their results show an initially sharp drop in the diffusion coefficient as tubulin is added, indicating that Flutax-2 has a relatively high affinity for soluble tubulin, compared to paclitaxel, and that Flutax-2 induces the formation of tubulin oligomers. The diffusion coefficients for pure Flutax-2 and tubulin-Flutax2 complex were determined to be $(2.2 \pm 0.2) \times 10^{-10}$ and $(4.1 \pm 0.2) \times 10^{-11}$ m²/s, respectively.

4.1 Total Internal Reflection Fluorescence Recovery After Photobleaching (TIR-FRAP)

Fluorescence recovery after photobleaching (FRAP) is a method by which the diffusion and reaction kinetics of a fluorescent species can be studied (Figure 4.1). A small region of a fluorescent specimen—for example, a portion of a cell membrane—is photobleached by a high intensity excitation pulse. This irreversibly inactivates fluorophore emission from particles in the FRAP region. The subsequent diffusion of mobile, non-photobleached particles into the FRAP region—measured as fluorescence recovery—can be used to estimate the diffusion coefficient and kinetics (if reactions occur) of the fluorescent species (*Carrero et al.*, 2003). FRAP can also be used to observe and quantify whether a fluorescently-labeled species is mobile. In the case of microtubules assembled from fluorescent tubulin, a FRAP recovery would demonstrate that the soluble tubulin signal (background fluorescence) quickly recovers via diffusion, however, tubulin buried within the microtubule lattice does not.

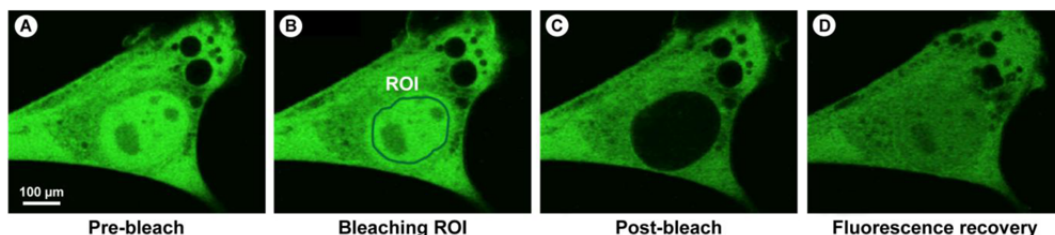


Figure 4.1: Fluorescence recovery after photobleaching. In fluorescence recovery after photobleaching (FRAP), a region of interest (B) of a fluorescent specimen is photobleached (C) using high excitation power. The recovery of unbleached particles into the bleached region (D) is then measured to estimate the diffusion coefficient of the fluorescent species, as well as its kinetics if reactions occur. Image from *Ishikawa-Ankerhold et al.* (2012).

Depending on the optical setup used for FRAP experiments, it can often be assumed that the extent of photobleaching is much greater in the z dimension (into the sample) than in the x and y (lateral) dimensions. By photobleaching a tall column of fluorophores, recovery in the FRAP region will occur primarily from the lateral flux

of unbleached particles, with a negligible flux in the axial (z) dimension. In these cases FRAP analysis of a Gaussian photobleach profile can be simplified to a 1D problem (*Hammond et al.*, 2009; *Goehring et al.*, 2010).

A variant of conventional FRAP is TIR-FRAP, where samples are photobleached using a TIRF excitation profile. TIRF-FRAP is a convenient method for performing FRAP studies while using TIRF microscopy, as it eliminates the need for an additional FRAP excitation source. In contrast to conventional FRAP, TIR-FRAP bleaches only a portion of the sample that is in close proximity to the cover slip. Thus, while in conventional FRAP diffusional recovery occurs predominantly in the lateral directions, in TIR-FRAP a significant proportion of the recovery is due to diffusion along the z - (optical) axis, toward the imaging plane. The multidimensional recovery profile of TIR-FRAP complicates analysis; while the lateral profile can be approximated as Gaussian, the photobleach profile in the z dimension is proportional to $e^{-z/d}$ (see Equation 4.1). Therefore, a TIR-FRAP model must be used in tandem with experimental recovery data to fully understand the fluorophore kinetics.

4.2 Microtubule-Flutax-2 Exchange Kinetics

In the present work, my goal was to characterize the diffusion of Flutax-2 particles in solution and to estimate the Flutax-2 kinetic rates using single-molecule studies of live microtubules *in vitro*, which has not yet been done. Although previous studies have not detected any structural differences between cross-linked and live microtubules (*Díaz et al.*, 2003), it is still possible that cross-linking might alter tubulin binding site energetics in subtle ways. To definitively rule out this possibility, live microtubules must be studied. Furthermore, studies of single microtubules will provide a clearer understanding of binding kinetics, since ensemble studies cannot measure the variances within a population microtubules, nor can they detect stochastic events that happen on shorter time scales.

4.2.1 Methods

Data was collected by TIRF microscopy at 37 °C, using a custom-built, single-channel microscope as described in Chapter 2. For TIR-FRAP experiments, the microscope was fitted with a Sutter Lambda 10-3 Optical Filter Changer and SmartShutter Control System, which was installed between microscope mirrors M2 and M3 (see Figure 2.4) and was controlled using Sutter software drivers and Matlab code. TIR-FRAP experiments were performed by switching between two filter wheel positions, one of which contained a 1.5 mm pinhole for sample bleaching, and the other which contained a 100x (OD 2.0) neutral density filter for imaging. Adjacent filter wheel positions were used to minimize switching times, which were ≤ 50 ms. The pinhole size was chosen such that the bleached region would be approximately half of the diameter of the EM-CCD camera field of view, so that both the bleached and non-bleach regions could be observed. This equated to a ~ 25 μm TIR-FRAP diameter within the 50×50 μm field of view. The beam reduction factor between the pinhole (located in the collimated beam region) and the sample plane is equal to the ratio of the focal lengths of the TIRF condenser (125 mm) and objective lenses (1.65 mm), which is about 76x. This indicated that a pinhole diameter of 1.9 mm was necessary to generate a 25 μm TIR-FRAP region. In the end, a pinhole diameter of 1.5 mm was used, and thus, the final TIRF-FRAP region was ~ 20 μm in diameter.

Experimental flow cells were prepared similarly to previously detailed in the Methods chapter. Biotinylated, GMPCPP-stabilized microtubule seeds, labeled with 2% HiLyte 488 tubulin, were adhered to the cover slip surface, which was coated with Neutravidin. A low labeling percentage was necessary so that the relatively dim Flutax-2 signal would not be overwhelmed by the brighter HiLyte 488 fluorophore. A solution containing buffer with 5.6 μM unlabeled tubulin, 1 mM GTP, 2 mM MgCl_2 , and Flutax-2 was added to the flow cells. Flutax-2 was serially diluted from 100 μM stock in DMSO, such that the final DMSO concentration was $\leq 0.5\%$.

Microtubules were imaged for 30 seconds using low excitation power, and then, once seed extensions had grown several microns, a region of the field of view was photobleached by increasing the excitation power by $100\times$ for 11 seconds. Recovery of the Flutax-2 signal on the seed extensions was recorded for approximately 60 seconds following the photobleach phase. Figure 4.2 (A–E) shows the time course of a TIR-FRAP experiment.

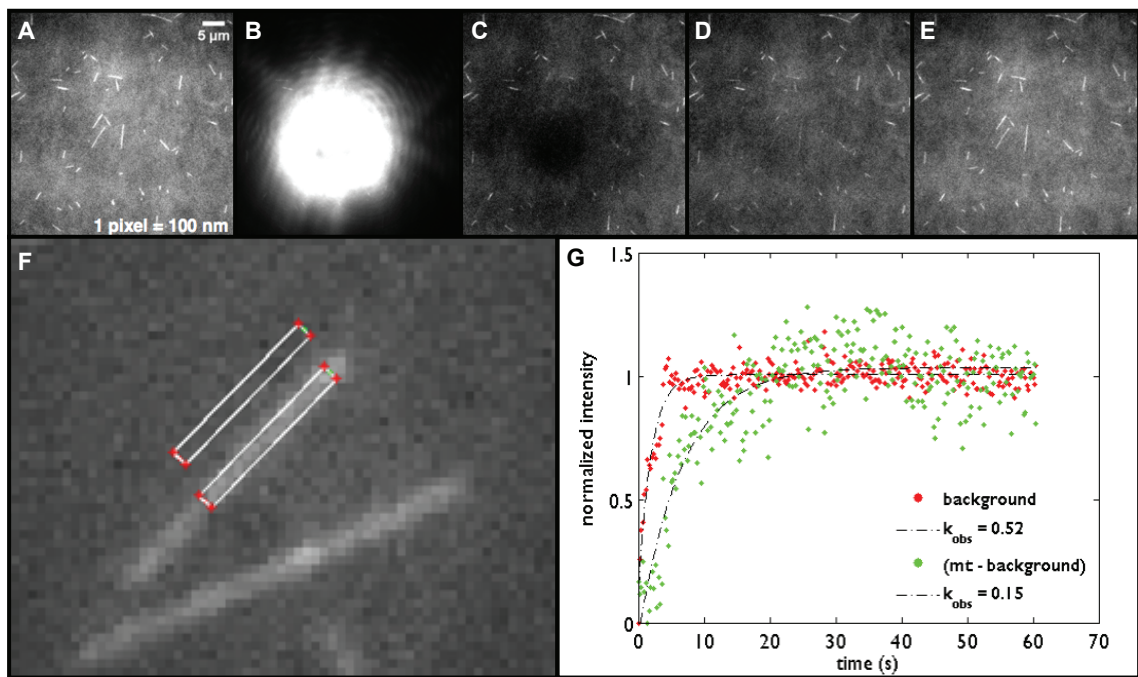


Figure 4.2: TIR-FRAP experiment and analysis. Flutax-2-labeled microtubules were centered in the TIR-FRAP region of the field of view (A). Microtubules were then photobleached for 11 seconds (B), and recovery of the Flutax-2 signal was recorded for approximately 60 seconds (C–E). The resulting data was analyzed in Matlab by calculating the average pixel intensity of Flutax-2-labeled seed extensions and subtracting off the intensity of an adjacent background region (F). Background and microtubule intensities were then plotted and fit with a single exponential to determine the observed recovery constants (G).

Video data was imported into Matlab for analysis, and microtubule intensities for each frame were recorded by averaging a region of the seed extension measuring approximately 2×20 pixels (see Figure 4.2 F). The background intensity adjacent to each microtubule was also recorded and subtracted from the microtubule intensity.

Microtubule and background recovery data were then fit using a single exponential to determine the observed recovery rates. As shown in Figure 4.2 G, background recovery rates were typically higher than the microtubule recovery rates, indicating that exchange of bleached Flutax-2 on the microtubule is slower than recovery by diffusion.

4.2.2 Results

Figure 4.3 shows the results of the microtubule TIR-FRAP experiments. For all tested Flutax-2 concentrations, recovery of the microtubule signal was slower than that of the background. There was no significant change in the microtubule recovery rate ($0.085 \pm 0.004 \text{ s}^{-1}$) between Flutax-2 concentrations of 100 and 300 nM, though at 500 nM Flutax-2, the recovery rate increased to $0.173 \pm 0.011 \text{ s}^{-1}$. Surprisingly, the background recovery rates decreased by nearly 2-fold, from $0.375 \pm 0.026 \text{ s}^{-1}$ at 100 nM Flutax-2 to $0.208 \pm 0.006 \text{ s}^{-1}$ at 500 nM Flutax-2. Since the recovery rate scales with the diffusion coefficient, these results implied that the diffusion coefficient decreased with higher concentrations of Flutax-2. However, according to Fick's law, the diffusion coefficient is independent of concentration. Thus, the TIR-FRAP results suggested that some type of reaction was occurring in solution, leading to a recovery rate concentration dependence.

To rule out the possibility that the microtubule seeds were somehow affecting local background recovery rates, I repeated Flutax-2 TIR-FRAP experiments using $5.6 \mu\text{M}$ tubulin without seeds. Nonetheless, I obtained nearly identical results across the same concentrations of Flutax-2. I then thought that Flutax-2 could be interacting with tubulin dimers, as shown in previous work (*Krouglova et al.*, 2004); however, in experiments with Flutax-2 alone the recovery rates showed a similar trend.

I knew that Flutax-2, like paclitaxel, is hydrophobic and could be aggregating in solution, which would lower the effective diffusion coefficient and slow the observed

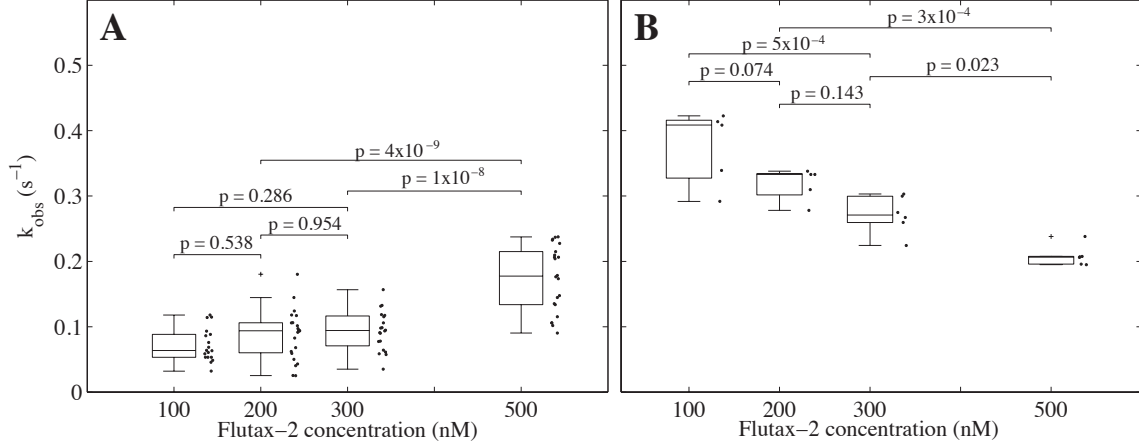


Figure 4.3: TIR-FRAP microtubule and background recovery rates. (A) Observed recovery rates of Flutax-2 on microtubule seed extensions, after subtraction of background signal. (B) Observed recovery rates of background Flutax-2 fluorescence after photobleaching.

recovery rates. I decided to investigate further by developing a TIR-FRAP diffusion model simulate the diffusion of Flutax-2.

4.3 TIR-FRAP Diffusion Model

To understand how Flutax-2 behaves in solution when used with TIR-FRAP, I developed a 2D axisymmetric diffusion model, which incorporates free diffusion of Flutax-2 and removal of Flutax-2 via spatially-dependent photobleaching:

$$\frac{\delta U}{\delta t} = D \left[\frac{1}{r} \frac{\delta U}{\delta r} + \frac{\delta^2 U}{\delta r^2} + \frac{\delta^2 U}{\delta z^2} \right] - k_B I U [1 - \tanh(r - r_b)] e^{-z/d} \quad (4.1)$$

where $U = U(r, z, t)$ is the concentration of unbleached Flutax-2 as a function of radius, depth, and time; k_B is the bleach rate (inverse time); I is the illumination intensity, r_b is the radius of the FRAP region, and d is the characteristic decay length of the TIRF evanescent field:

$$d = \frac{\lambda_0}{4\pi} [n_1^2 \sin^2 \theta - n_2^2]^{-1/2} \quad (4.2)$$

where λ_0 is the excitation wavelength in a vacuum, n_1 and n_2 are the refractive indices of the glass cover slip and sample liquid, respectively, and θ is the excitation angle, which is increased beyond the critical angle, θ_c , to achieve TIRF illumination (*Axelrod et al.*, 1984)

$$\theta_c = \sin^{-1}(n_2/n_1) \quad (4.3)$$

Figure 4.4 shows the model geometry with spatial coordinates r and z . The model domain extends out to radius $R = 2.5$ mm and depth $Z = 100$ μ m. The imaging region, which is illuminated at low intensity, is defined by a radius of $r_{im} = 25$ μ m, and the TIR-FRAP region, which is illuminated at high intensity through a pinhole aperture, is defined by a radius of $r_b = 12.5$ μ m. No flux boundary conditions are set at the flow cell boundaries $r = R$, $z = 0$, and $z = Z$, and for continuity, the boundary of the TIR-FRAP region is defined by a hyperbolic tangent function. Results from experimental data show that beyond the first 30 seconds of imaging, the average emission intensity drops by less than 1% after 10 minutes; therefore, the model does not consider any photobleaching during low-intensity imaging.

Some of the model parameters were fixed using known or estimated values. The evanescent depth, which is approximately equal to the excitation wavelength (*Axelrod*, 2001), was set to $d = 491$ nm, in agreement with values calculated using Equation 4.2, and the imaging intensity, I , was stepped between values of 1 and 100, reflecting the relative changes in power due to addition or removal of the 100x neutral density filter, respectively. The bleaching rate constant (r_B) and the diffusion coefficient (D) were fit using 100 nM Flutax-2 recovery data, and then r_B was fixed and D was left as a free parameter. In this way, I could perform simulations to determine how the diffusion coefficient was affected by increasing concentrations of Flutax-2.

The model was simulated in Comsol software by creating a 2D axisymmetric surface of dimensions r and z , the revolution of which defines the domain volume. The solution was photobleached for 11 seconds, and the model was run for an ad-

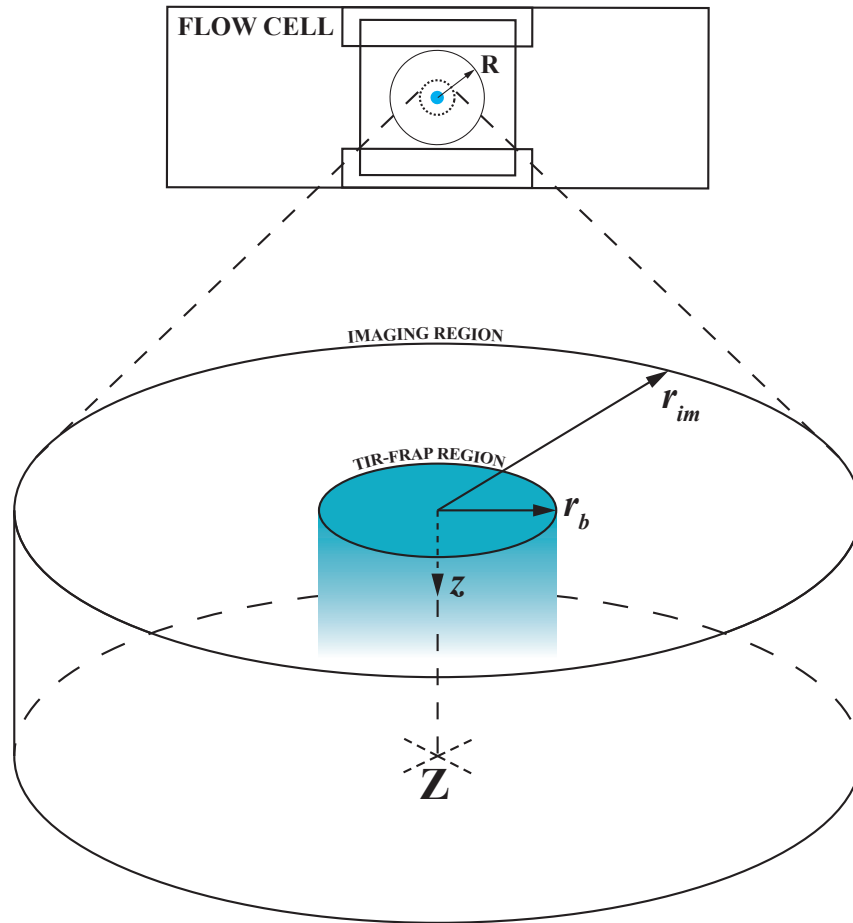


Figure 4.4: TIR-FRAP model geometry. The model uses a 2D axisymmetric domain of radius R and depth Z . During imaging, a region of radius r_{im} is illuminated at low intensity. Based on experimental controls, the photobleaching rate during imaging is considered negligible. During the photobleaching phase, excitation power is increased by $100\times$ and occurs through a pinhole aperture, resulting in an illuminated region of radius r_b . The TIRF excitation profile along the z dimension is given by $Ie^{-z/d}$.

ditional 30 seconds to capture the recovery phase. Following the simulation, which estimates $U(r, z, t)$, intensity data was calculated as the convolution of $U(r, z, t)$ with the evanescent excitation field $Ie^{-z/d}$ (Equation 4.4). This integral is proportional to the TIRF-profile intensity as seen from $z = 0$ and represents the signal that would be collected by the EMCCD camera during experimental data collection. The resulting intensity versus time data was then imported into Matlab for further analysis.

$$I_{sol} = \int \int U(r, z, t) Ie^{-z/d} dr dz \quad (4.4)$$

4.4 Model and Experimental Results

I performed TIR-FRAP experiments using a range of Flutax-2 concentrations and then used the data to fit model parameter D for each concentration. This was done by normalizing recovery data to values of 0 to 1, and then using a Levenberg-Marquardt algorithm to optimize D , as well as scaling and offset parameters, to match experimental data. The model predicted a decreasing diffusion coefficient with increasing Flutax-2 concentration, suggesting that Flutax-2 was aggregating in solution.

To test this experimentally, I repeated TIR-FRAP experiments, this time increasing the DMSO concentration to 5% to increase the solubility of Flutax-2. For the previous set of experiments the DMSO concentrations were $\leq 0.5\%$. After adjusting DMSO to 5%, k_{obs} increased from less than 0.5 s^{-1} to $\sim 3 \text{ s}^{-1}$ over the range of tested Flutax-2 concentrations and showed no concentration dependence, indicating that it was properly solubilized. This result provided further evidence of Flutax-2 aggregation at DMSO concentrations $\leq 0.5\%$.

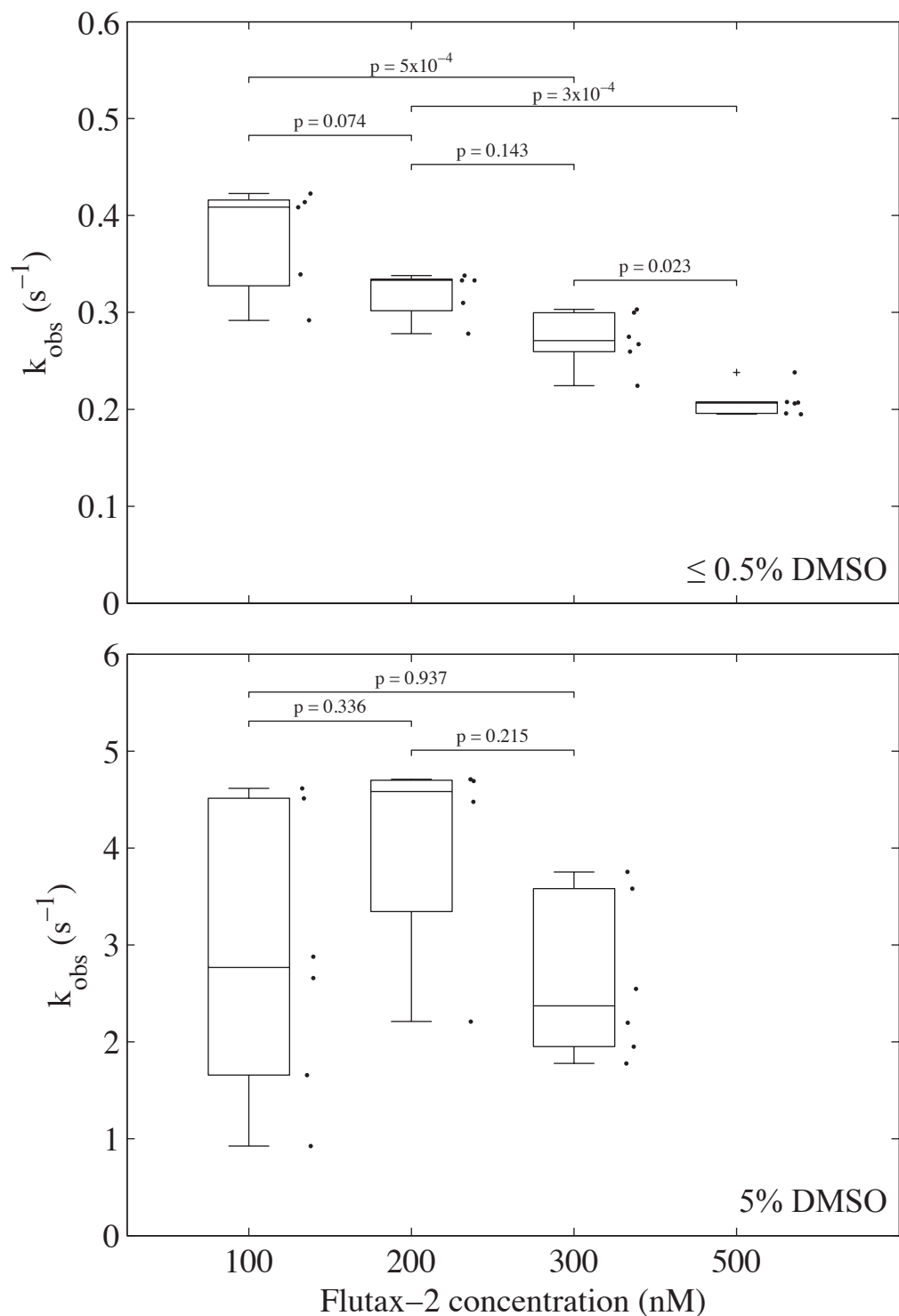


Figure 4.5: Observed TIR-FRAP recovery constants of Flutax-2 in buffer. *Upper panel:* Data from slides with $\leq 0.5\%$ DMSO. k_{obs} decreases with increasing [Flutax-2]. *Lower panel:* Data from slides with 5% DMSO. k_{obs} values are unaffected by changes in [Flutax-2] and are order of magnitude larger than values from slides with [DMSO] $\leq 0.5\%$.

4.4.1 Flutax Isodesmic Polymerization Model

To further study this phenomenon, I used an isodesmic polymerization model to describe the interaction of Flutax-2 particles. For free Flutax-2 in solution the observed rate of recovery, k_{obs} , should be proportional to the effective diffusion coefficient (D_{eff}). For a population of molecular species, D_{eff} is equal to the sum of the diffusion coefficients for each species, weighted by their relative fractions:

$$D_{eff} = \frac{[F]}{[F]_{tot}} D_1 + \frac{[F]_2}{[F]_{tot}} D_2 + \frac{[F]_3}{[F]_{tot}} D_3 + \dots + \frac{[F]_N}{[F]_{tot}} D_N \quad (4.5)$$

where $[F]$ is the concentration of Flutax-2 in monomer form, $[F]_{tot}$ is the total concentration of Flutax-2, $[F]_i$ is the concentration of Flutax-2 polymer assembled to the i th degree, D_i is the corresponding diffusion coefficient, and N is the number of Flutax-2 subunits in the longest assembled polymer. Since the diffusion coefficient is inversely proportional to the cube root of mass (*Serdyuk et al.*, 2007), equation 4.5 can be rewritten as:

$$D_{eff} = \frac{[F]}{[F]_{tot}} \frac{\beta}{1^{1/3}} + \frac{[F]_2}{[F]_{tot}} \frac{\beta}{2^{1/3}} + \frac{[F]_3}{[F]_{tot}} \frac{\beta}{3^{1/3}} + \dots + \frac{[F]_N}{[F]_{tot}} \frac{\beta}{N^{1/3}} \quad (4.6)$$

where proportionality constant β scales to the diffusion coefficient.

Next, if all polymerization steps are assumed to be kinetically equivalent, equilibrium constant K_F can be written as:

$$K_F = \frac{[F]_{i+1}}{[F][F]_i} \quad (4.7)$$

Then, beginning with dimerization

$$\begin{aligned}
[F]_2 &= K_F [F]^2 \\
[F]_3 &= K_F [F] [F]_2 = K_F^2 [F]^3 \\
&\vdots \\
[F]_i &= K_F^{i-1} [F]^i
\end{aligned} \tag{4.8}$$

By applying conservation of Flutax-2 monomer and combining with Equation 4.8 (*Oosawa et al.*, 1975):

$$[F]_{tot} = \sum i [P]_i = K_F^{i-1} \sum i [F]^i = \frac{[F]}{(1 - K_F [F])^2} \tag{4.9}$$

Equation 4.9 can then be solved to express the concentration of Flutax-2 monomer:

$$[F] = \frac{1}{K_F} + \frac{1}{2 K_F^2 [F]_{tot}} - \frac{1}{K_F} \left[\frac{1}{K_F [F]_{tot}} + \frac{1}{4 K_F^2 [F]_{tot}^2} \right]^{1/2} \tag{4.10}$$

Finally, since k_{obs} is proportional to D_{eff} , we can combine equations 4.6 and 4.10 to create an expression relating the observed recovery rate to the total Flutax-2 concentration (in monomer and polymer) for isodesmic polymerization:

$$k_{obs} = \alpha \sum_{i=1}^N \frac{K_F^{i-1} [F]^i}{i^{1/3} [F]_{tot}} \tag{4.11}$$

where α is the product of β and a proportionality constant relating k_{obs} and D .

Parameters α and K_F in equation 4.11 were fit using a Levenberg-Marquardt algorithm to minimize the sum of square residuals between the model and experimental measurements of k_{obs} . An accurate model fit required values of k_{obs} at low Flutax-2 concentrations; however, the Flutax-2 signal is difficult to measure at concentrations below 100 nM. Since 5% DMSO appears to eliminate the k_{obs} concentration dependence, k_{obs} at $[Flutax-2] = 0$ for the low $[DMSO]$ data set was estimated as the mean

of pooled k_{obs} values from the $[DMSO] = 5\%$ data set. The model fit is shown in Figure 4.6, using optimized parameter values $\alpha = 3.08$ and $K_F = 1.45 \times 10^{-10} \text{ M}^{-1}$.

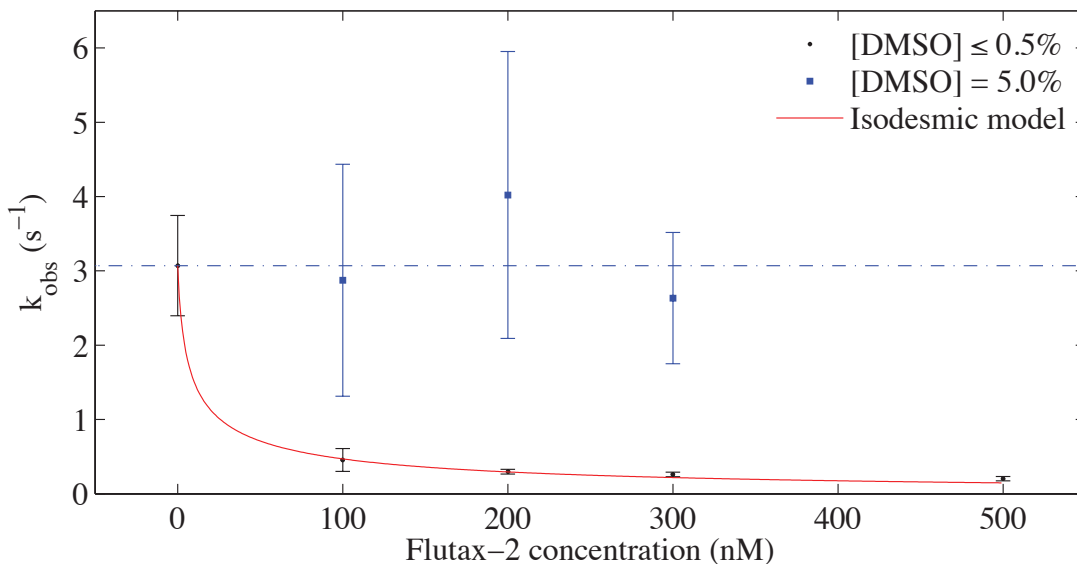


Figure 4.6: Flutax-2 isodesmic model. Observed recovery rate constants from experimental data sets using $[DMSO] \leq 0.5\%$ and $[DMSO] = 5\%$. k_{obs} at $[Flutax-2] = 0$ for the $[DMSO] \leq 0.5\%$ data set was estimated as the mean of pooled values from the $[DMSO] = 5\%$ data set. Model parameters α and K_F in Equation 4.11 were optimized using a Levenberg-Marquardt algorithm and found to be 3.08 and $1.45 \times 10^{-10} \text{ M}^{-1}$, respectively. Error bars represent 95% confidence intervals.

Equation 4.10 can be plotted to show how the Flutax-2 monomer concentration, or fraction of Flutax-2 in monomer form, changes with the total Flutax-2 concentration (Figure 4.7). The model predictions show that the fraction of Flutax-2 in monomer form decreases as more Flutax-2 is added to solution. For 100 nM of added Flutax-2, only about 5.3% (5.3 nM) remains in monomer form, and at 500 nM the monomer fraction drops to approximately 1.2% (6 nM). In fact, the model predicts that increasing concentrations of Flutax-2 have a diminishing effect on the monomer concentration, which plateaus around 6 nM. At these concentrations the average degrees of polymerization, given by:

$$\langle i \rangle = \frac{[F]_{tot}}{\sum [P_i]} = \frac{\sum i [P_i]}{\sum [P_i]}, \quad (4.12)$$

are 4.3 and 9.0 Flutax-2 subunits, respectively. Given the size of these aggregates, it is unlikely that they are able to bind to the paclitaxel site.

These findings have significant implications for previous work that has used Flutax-2 to study microtubules and microtubule-targeting drugs. The substantial reduction in the binding-competent, monomeric fraction of Flutax-2 may confound interpretation of these studies. For example, disparities in the observed potency of Flutax-2 and paclitaxel (*Abal et al.*, 2001) may be explained not only by true differences in binding affinity, but also by a reduction in the active concentration of Flutax-2. Furthermore, an apparent affinity of Flutax-2 for soluble tubulin, estimated by measuring changes in the diffusion coefficient (*Krouglova et al.*, 2004), may be due to coaggregation of Flutax-2 polymers and tubulin dimers. It is also important to consider that these results could affect studies of paclitaxel, which may aggregate similarly at low nanomolar concentrations.

4.4.2 Characterization of Flutax-2 Surface Binding

Because the addition of 5% DMSO largely eliminated Flutax-2 aggregation, I planned to include this concentration in future experiments. However, upon closer inspection of my previous Flutax-2 data with 5% DMSO, I noticed that the background signal during photobleaching increased with time. I attempted to study this phenomenon by performing TIR-FRAP experiments with an extended photobleaching phase using 500 nM Flutax-2 with 0.5% and 5% DMSO.

As shown in Figure 4.8, an increase in the excitation power quickly led to high fluorophore emission, which saturated the camera. The Flutax-2 solution using 5% DMSO remained saturated for the duration of the photobleaching phase, and thus, changes in intensity could not be analyzed. However, a portion of the 0.5% DMSO data was below saturating intensities. Surprising, there was a transient drop in intensity, followed by an increase back to saturating levels. This drop was likely not seen

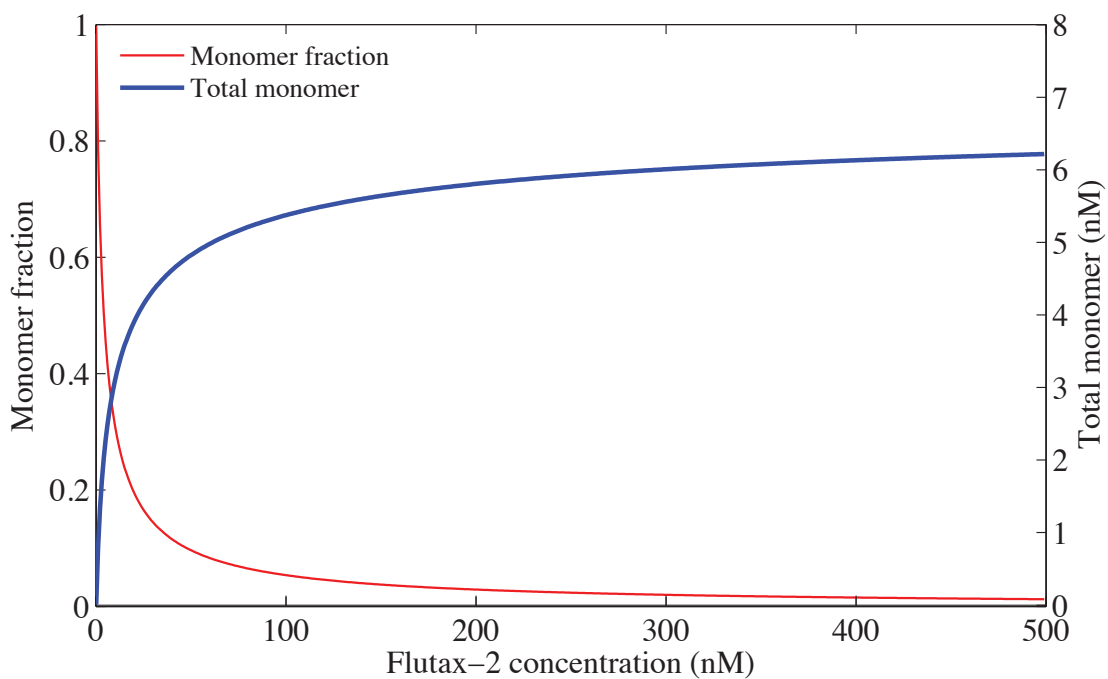


Figure 4.7: Flutax-2 monomer fraction versus Flutax-2 concentration. Predictions from the isodesmic polymerization model show that the fraction of monomeric Flutax-2 drops precipitously when low nanomolar concentrations of Flutax-2 are added to solution. At 100 nM total Flutax-2 only 5.3% (5.3 nM) remains in monomer form, and at 500 nM only 1.2% (6 nM) remains as monomer.

in the 5% DMSO data due to the faster diffusion. Higher levels of DMSO prevented Flutax-2 aggregation, resulting in a higher effective diffusion coefficient, such that the transient dip in intensity was too short to be observed. The same effect can be seen at the end of the photobleach phase, where the 5% DMSO intensity recovers more quickly than 0.5% DMSO intensity. I also found that during the recovery phase, the intensity increased, peaked, and then lowered to a stable level, rather than simply recovering and plateauing as expected. Interestingly, the peak was higher than stable pre-photobleach levels and the effect was limited to the photobleached pinhole region.

I thought these effects may have been associated with the activation of the triplet state of the fluorescent conjugate, Oregon Green 488 (OG488). I tested this by supplementing experimental solutions—in separate slides—with triplet state quenchers Trolox and β -mercaptoethanol (*Dave et al.*, 2009), however, they failed to mitigate the issue. I also performed control photobleaching experiments using Phalloidin-OG488 with 5% DMSO at an equivalent conjugate concentration (500 nM), as well as a higher concentration (1250 nM). As shown in Figure 4.9, the intensity of 500 nM Phalloidin-OG488 was much lower than that of 500 nM Flutax-2 during photobleaching, and it was nearly undetectable when illuminated with a lower intensity used for normal imaging. Moreover, there was no transient drop in signal after increasing to photobleaching intensity, nor was there a rise in signal over the duration of the photobleach. TIR-FRAP experiments using 1250 nM Phalloidin-OG488 yielded similar results, and intensities were still well below saturating levels.

This led me to believe that the fluorescence effects could be due to interaction of Flutax-2 with the cover slip surface. As detailed in the Methods chapter, cover slips are treated with dichlorodimethylsilane followed by subsequent passivation with Pluronic F127 to reduce surface binding of tubulin, which is relatively hydrophilic. Flutax-2, however, is hydrophobic and may have a higher affinity for the cover slip surface.

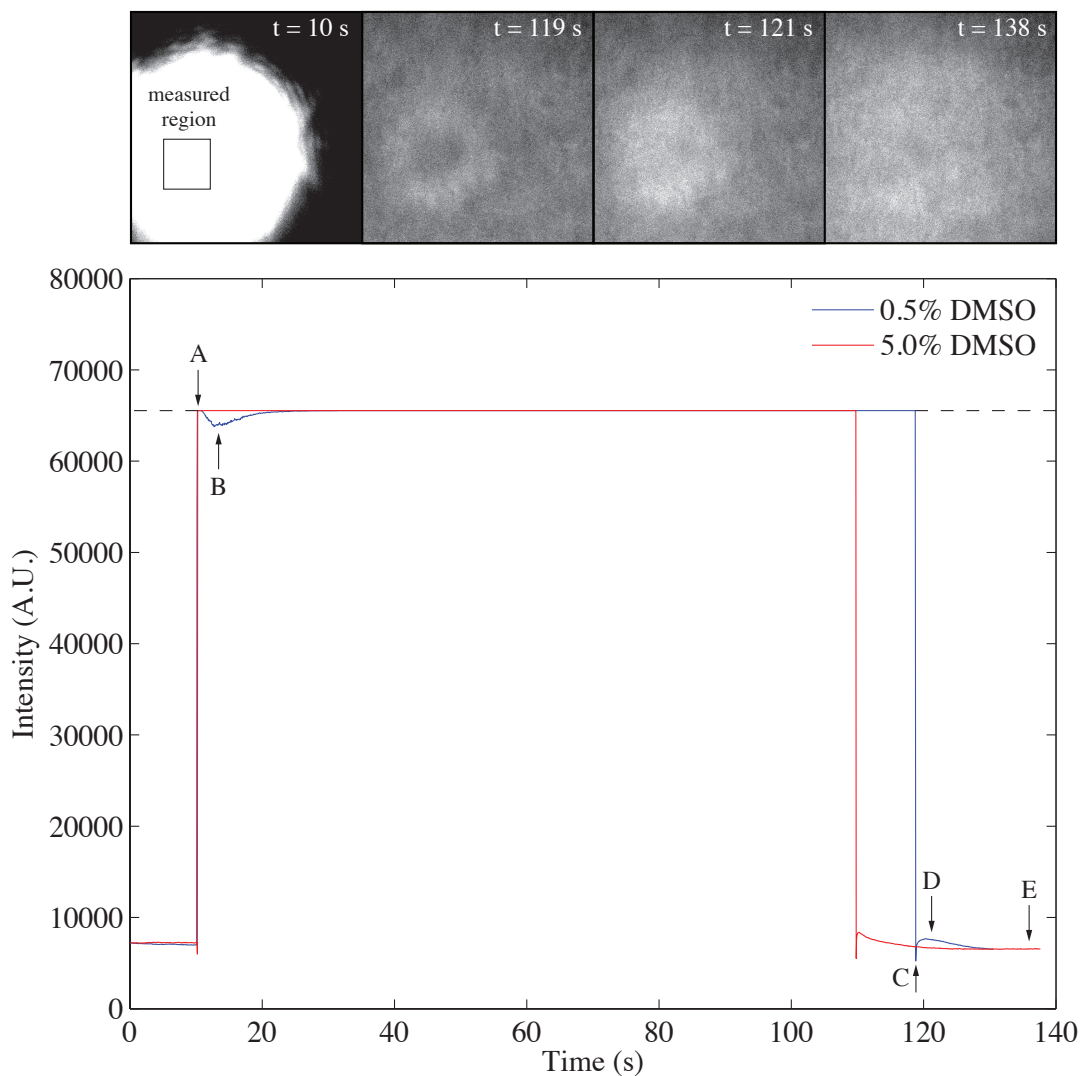


Figure 4.8: Flutax surface interactions. *Upper:* Image frames from a TIR-FRAP experiment with 500 nM Flutax-2 and 5% DMSO. During photobleaching the camera is saturated. After reducing the excitation power, the intensity momentarily overshoots pre-photobleaching levels, before lowering to an intensity that is slightly below pre-photobleach levels. *Lower:* Plot shows TIR-FRAP intensity data for 500 nM Flutax-2 with 0.5% or 5% DMSO. 5% DMSO prevents Flutax-2 aggregation and results in a higher effective diffusion coefficient, so intensity changes are fast and difficult to observe. In 0.5% DMSO data, excitation power is increased, leading to high emission intensity and camera saturation (A), followed by a period of net intensity loss due to photobleaching and subsequent rise back to saturating levels (B). Upon reduction of excitation power (C), the intensity recovers and transiently overshoots pre-photobleach levels (D) before leveling off below pre-photobleach levels (E).

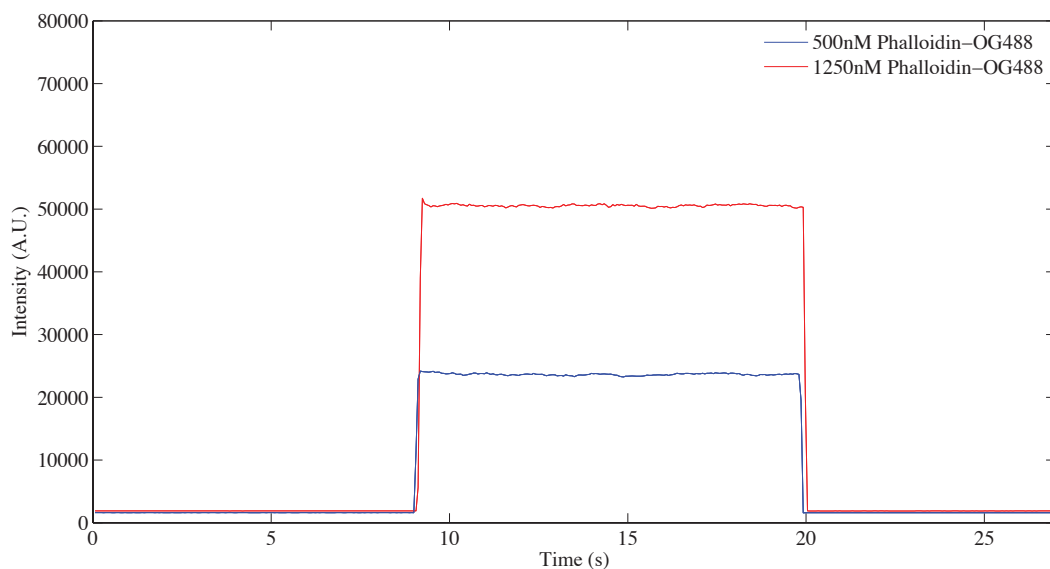


Figure 4.9: Phalloidin-OG488 TIR-FRAP control experiment. Phalloidin-OG488 displays an expected FRAP intensity profile, compared to the profile of Flutax-2, which is non-monotonic.

To test this possibility, I performed another set of control experiments using 500 nM Flutax-2 with untreated cover slips and omitted Pluronic F127 passivation. To account for the effects of added DMSO, I conducted separate experiments using 0.5% and 5% DMSO. My results showed that for both DMSO concentrations the average fluorescence intensity was greatly reduced, and there was no discernible recovery phase intensity overshoot, leading me to conclude that cover slip treatment was facilitating surface binding (see Figure 4.10). However, the photobleach-phase intensity profile still exhibited a non-monotonic behavior, indicating that some other process was occurring.

I next wanted to determine how titrating the concentration of the oxygen scavenging (antifade) system would affect the fluorescence signal. The antifade system neutralizes fluorophore-damaging free radicals that are generated by fluorophore emission. I compared the fluorescent signal during periods of extended photobleaching, as before, using antifade concentrations of 0 \times , 0.5 \times , and 1 \times with 5% DMSO and

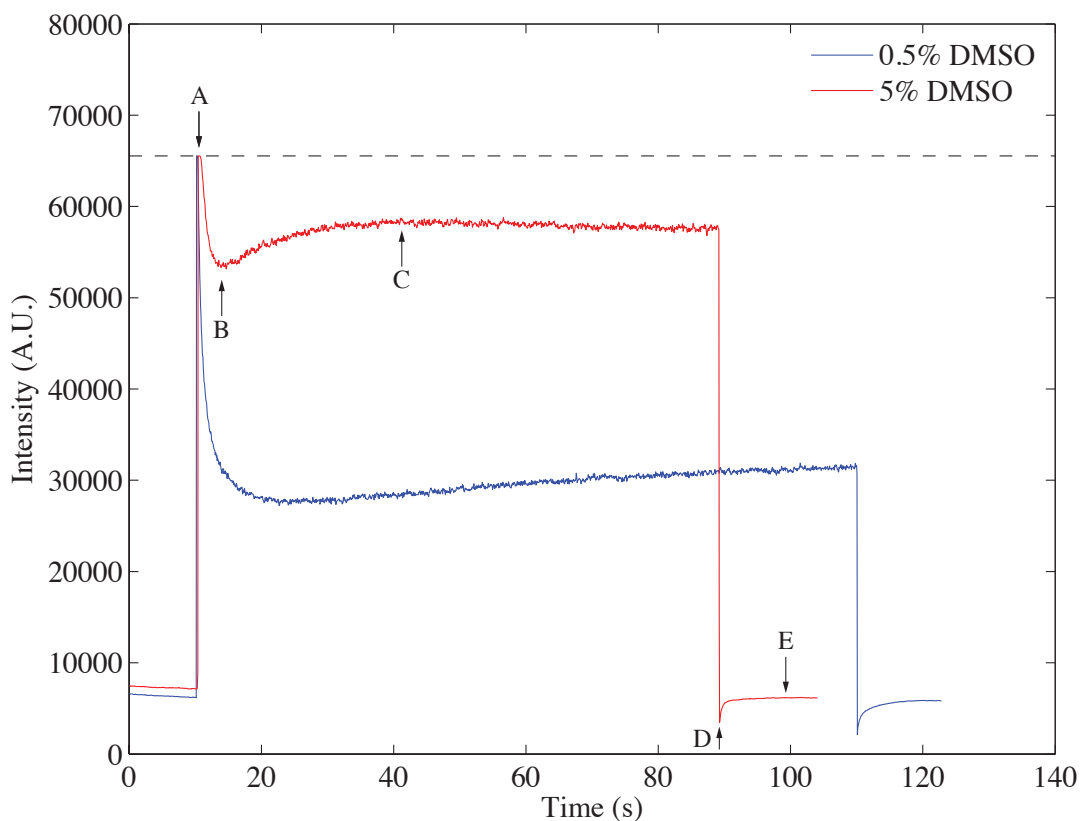


Figure 4.10: Effects of cover slip treatment on flutax surface interactions. Compared to similar data collected using treated cover slips (Figure 4.8), intensities using untreated cover slips were much lower, and there was no apparent recovery-phase overshoot. As expected, kinetics were faster with 5% DMSO, which better solubilizes Flutax-2. In the sample with 5% DMSO, intensity peaked at the onset of the photo-bleaching phase (A), then quickly decreased to a minimum (B) before slowly rising, plateauing (C), and slowly decreasing. Once the excitation power was reduced (D), the intensity recovered and plateaued with no overshoot (E). Similar results were seen in the 0.5% DMSO sample, though intensity changes occurred at a slower rate.

treated cover slips. As expected, photobleaching was more extensive at lower antifade concentrations. At $1\times$ antifade the fluorescent signal remained at saturating levels; at $0.5\times$ the signal transiently dropped before increasing and plateauing; and at $0\times$ the signal dropped and plateaued at a relatively low intensity.

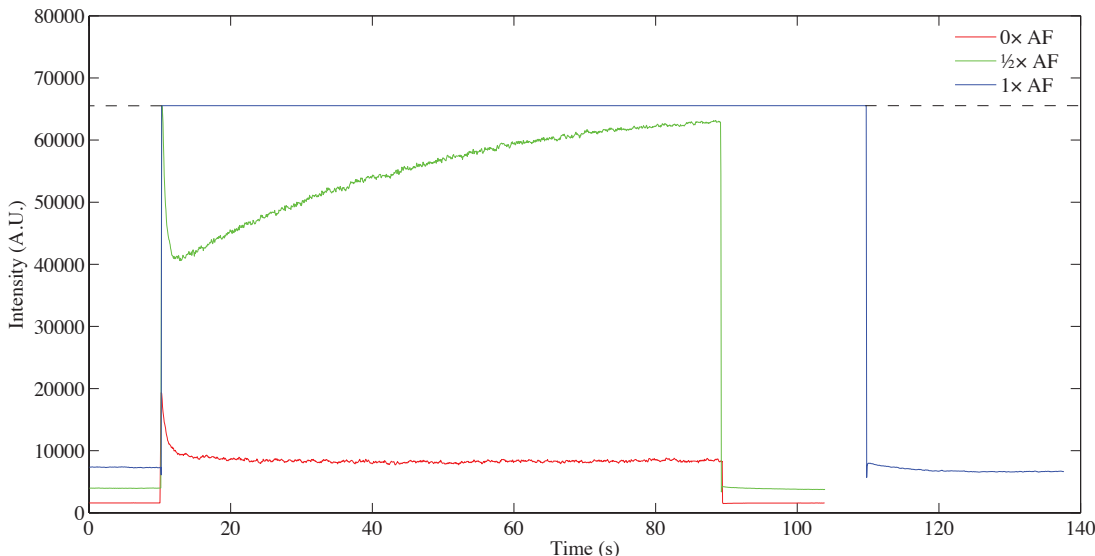


Figure 4.11: Effects of antifade concentration on Flutax-2 surface interactions. Decreasing the concentration of antifade increases the photobleaching rate.

4.4.3 Expanded TIR-FRAP Diffusion and Surface Reaction Model

Together, these control studies indicated that the observed surface effects were the result of multiple processes, which are at steady state prior to the photobleaching phase. Besides the diffusion and photobleaching of Flutax-2 particles in solution, there is also adsorption and desorption of particles—bleached and unbleached—to and from the coverslip surface. Unbleached Flutax-2 on the surface can also be bleached, but unlike particles in solution, the concentration of unbleached Flutax-2 on the surface can increase to levels where fluorophore self-quenching becomes significant. As seen in Figure 4.12, as the surface concentration of unbleached Flutax-2 increases, the overall emission increases; however, as the concentration is further increased, the density of Flutax-2 particles becomes so high that the conjugate fluorophores

interact with one another such as emitted photons are reabsorbed. This effect is known as self-quenching, which causes a drop in emission intensity at high fluorophore concentrations.

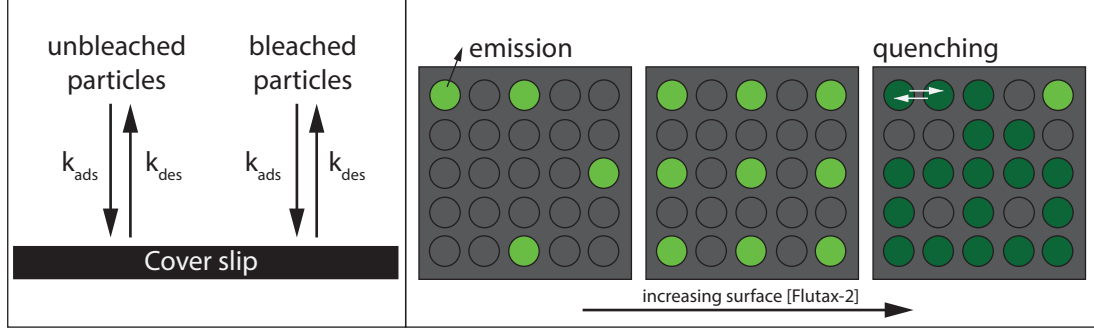


Figure 4.12: Proposed Flutax-2 surface binding and self-quenching diagram. *Left:* Bleached and unbleached Flutax-2 particles bind and unbind the surface with similar kinetics. *Right:* As the surface density of unbleached Flutax-2 particles (bright green circles) increases, the overall surface fluorescence increases. However, at very high surface densities, Flutax-2 particles interact with one another and self-quench. Emitted photons of Flutax-2 particles are immediately absorbed by adjacent Flutax-2 particles, leading to fluorescence attenuation (dark green circles).

To account for these effects in the TIR-FRAP model, I updated the model to simulate both the bleached and unbleached Flutax-2 populations and added equations to describe surface binding and fluorophore self-quenching. Since experimental results showed that Flutax-2 aggregation was insignificant when using 5% DMSO, no related adjustments were made to the model.

To track bleached and unbleached Flutax-2 particles, the model includes two diffusion equations:

$$\frac{\delta F_i}{\delta t} = D \left[\frac{1}{r} \frac{\delta F_i}{\delta r} + \frac{\delta^2 F_i}{\delta r^2} + \frac{\delta^2 F_i}{\delta z^2} \right] + R_i \quad (4.13)$$

where F_i represents either the unbleached (F_U) or bleached (F_B) Flutax-2 concentration, and R_i represents the corresponding reaction term, given by:

$$\begin{aligned} R_U &= -k_B I F_U [1 - \tanh(r - r_b)] e^{-z/d} \\ R_B &= +k_B I F_B [1 - \tanh(r - r_b)] e^{-z/d} \end{aligned} \quad (4.14)$$

As shown in Equations 4.14, photobleaching removes particles from the unbleached population and adds them to the bleached population.

The second order surface reaction terms are dependent on the concentration of available surface binding sites, as well as the concentrations of bleached and unbleached particles on the surface and in solution.

$$\begin{aligned}\frac{\delta S_U}{\delta t} &= k_{ads}F_U(S^* - S_U - S_B) - k_{des}S_U - k_BIS_U \\ \frac{\delta S_B}{\delta t} &= k_{ads}F_B(S^* - S_U - S_B) - k_{des}S_B + k_BIS_U\end{aligned}\tag{4.15}$$

where S_U and S_B are the surface concentrations of unbleached and bleached Flutax-2 particles, respectively; k_{ads} and k_{des} are the surface adsorption and desorption rates, respectively; and S^* is the total concentration of surface binding sites. The parenthetical term represents the number of available binding sites (initially equal to S^*), and the final term of each equation redistributes photobleached fluorophores from the unbleached to the bleached population.

In the Comsol model, the diffusion and surface reaction modules are related by a flux from the bulk solution to the surface at the $z = 0$:

$$\begin{aligned}\frac{\delta S_U}{\delta t} &= -k_{ads}F_U(S^* - S_U - S_B) + k_{des}S_U \\ \frac{\delta S_B}{\delta t} &= -k_{ads}F_B(S^* - S_U - S_B) + k_{des}S_B\end{aligned}\tag{4.16}$$

Self-quenching of surface-bound Flutax-2 is governed by Equation 4.17 (*Memoli et al.*, 1999):

$$I = \beta_f(1 - 10^{-\epsilon_{S_U}})e^{k_{ife} S_U}\tag{4.17}$$

where β_f is a proportionality constant, ϵ_m is the fluorophore extinction coefficient (76,000 $\text{cm}^{-1}\text{M}^{-1}$ for Oregon Green 488), and k_{ife} is a constant representing loss of fluorescence due to the inner filter effect.

The total fluorescent emission from the system is then equal to the combined

fluorescence from the bulk solution:

$$I_{sol} = \int \int F_U(r, z, t) I e^{-z/d} dr dz \quad (4.18)$$

and the surface:

$$I_{surf} = \int S_U(r, t) \beta_f (1 - 10^{-\epsilon S_U}) e^{k_{ife} S_U} dr \quad (4.19)$$

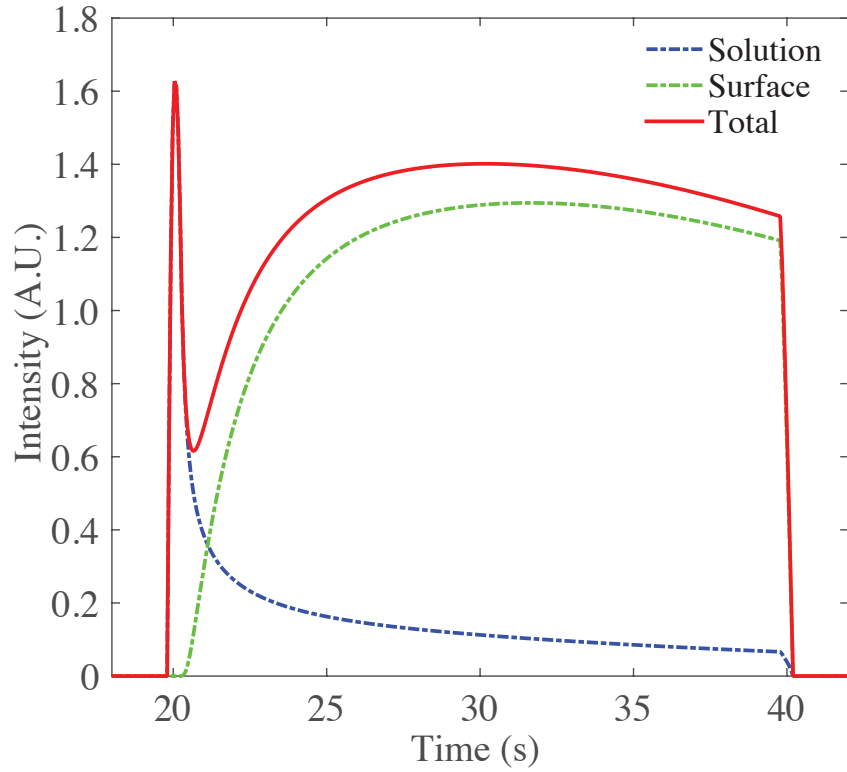


Figure 4.13: TIR-FRAP simulations with surface interactions and fluorophore self-quenching. When surface interactions and fluorophore self-quenching are added to the TIR-FRAP model, it is able to reproduce experimentally-observed fluorescence effects (red curve). Photobleaching of Flutax-2 in solution leads to a fluorescence signal that can be described by a decaying exponential (blue curve). On the surface (green curve), photobleaching, kinetics, and self-quenching are initially at equilibrium; however, an increase in excitation power lowers the density of unbleached particles via photobleaching. This relieves self-quenching effects, resulting in an increase in fluorescence emission. Eventually, as more surface particles are photobleached, self-quenching becomes negligible, and further bleaching results in a reduced number of fluorophores and concomitant loss of fluorescence.

My simulations showed that surface binding and self-quenching are able to account for the experimentally-observed non-monotonic fluorescence effects. As seen in Figure 4.13, loss of fluorescence from the bulk solution follows a decaying exponential, as Flutax-2 particles are photobleached more quickly than can be replaced via diffusion.

Fluorescence emission from the surface component is more complex; initially, the concentration of surface-bound, unbleached particles is high since the excitation power and thus, the bleaching rate, are low. Because the surface is nearly saturated with unbleached particles, fluorescence attenuation due to self-quenching is at a maximum. During the photobleaching phase, the surface concentration of unbleached particles begins to drop due to a higher bleaching rate. Self-quenching is slowly relieved, which results in an increase in net fluorescence. Eventually though, self-quenching effects are completely relieved, and further bleaching of surface particles leads to a decrease in surface fluorescence.

4.5 Future Studies of Microtubule-Flutax-2 Kinetics

Control studies have shown that 5% DMSO is sufficient to solubilize Flutax-2 in aqueous solution and prevent particle aggregation. Furthermore, the TIR-FRAP model described above can accurately predict how monomer Flutax-2 behaves in solution and on the cover slip surface. Data from future simulations and experiments performed using 5% DMSO can be analyzed together to estimate the kinetics of Flutax-2 binding to live microtubules.

CHAPTER V

Materials and Methods

5.1 Materials

All chemicals were obtained from Sigma-Aldrich Corporation (St. Louis, MI, USA) or Thermo Fisher Scientific (Waltham, MA, USA), unless otherwise stated. HiLyte 488 tubulin from Cytoskeleton, Inc. (Denver, CO, USA) was used for initial paclitaxel studies, and subsequent studies used tubulin labeled in-lab using HiLyte Fluor 488 dye from Life Technologies (Carlsbad, CA, USA). Some microtubule seeds were labeled with Cy3.5 dye, which was also purchased from Life Technologies. Optical components were purchased from Thorlabs (Newton, NJ, USA), Chroma Optics (Burlington, VT, USA), and Semrock (Rochester, NY, USA).

5.2 Buffer conditions

All experiments were performed in BRB80 buffer (80 mM PIPES, 1 mM MgCl_2 , and 1 mM EGTA, pH 6.8), and unless otherwise specified all reagents were dissolved in BRB80. Experimental solutions contain an additional 1 mM MgCl_2 (for a total of 2 mM). In fluorescence experiments the buffer was supplemented with an oxygen-scavenging (antifade) system to reduce the photobleaching rate (30 mM glucose, 0.6 mg/mL glucose oxidase, 0.12 mg/mL catalase, and 2 mM dithiothreitol (DTT)).

5.3 Tubulin purification

Tubulin was purified from bovine brain via two polymerization-depolymerization cycles using high molarity PIPES buffer, as described by *Castoldi and Popov* (2003) with slight modification. Prior to blending the brains, the brain plus depolymerization buffer (DB) volume was brought to 1.5 mM ATP, 0.25 mM GTP, 0.1% β -mercaptoethanol (BME; v/v), 4 mM DTT, and 0.1% (v/v) each of protease inhibitors (1 mg/mL leupeptin, 10 mg/mL soybean trypsin inhibitor, 2 mg/mL aprotinin, 5 mg/mL tosyl phenylalanyl chloromethyl ketone, 1 mg/mL pepstatin, 35 mg/mL phenylmethylsulfonyl fluoride, and 20 mg/mL Na-p-tosyl-L-arginine methyl ester). Following the first warm centrifugation microtubules were depolymerized in 100 mL of cold DB supplemented with 0.1 mM GTP, 4 mM DTT, 0.1% (v/v) BME, and 0.1% each of protease inhibitors. Depolymerization and resuspension of tubulin was facilitated by using a dounce tissue grinder to dissolve the pellet. After the second warm spin the microtubule pellets were dounced in less than 10 mL of cold BRB80 buffer and placed on ice for 20 minutes. After the final cold spin, the supernatant was extracted and flash frozen using liquid nitrogen in 20 μ L aliquots and stored at -80 °C. Small sample aliquots were collected at each step of the purification for subsequent analysis.

5.4 Tubulin labeling

Tubulin was labeled using a protocol by the Mitchison Lab (*Tim Mitchison Lab*, 2016) with minor changes. In the initial polymerization step, 50% volume of glycerol was added to the tubulin, and the solution was brought to 4 mM MgCl_2 and 1 mM GTP. After the first warm spin, the pellet was resuspended in 1 mL of warm labeling buffer using a 1 mL pipette with the tip cut back. Resuspensions were aided by use of a 1 mL dounce. The optimal amount of dye to add (relative to the starting

uncycled tubulin concentration) is dependent upon the particular fluorophore used. The goal is to maximize tubulin yield at a dye:dimer labeling stoichiometry close to 1:1. Suggested molar excesses of TAMRA-SE, Cy3 (mono-reactive NHS ester), Cy3.5, and HiLyte Fluor 488 dyes are 6 \times , 10 \times , 10 \times , and 4 \times , respectively. After centrifuging the labeled tubulin the labeling buffer was aspirated, and the cushion interface was rinsed with deionized water. The cushion was then aspirated, and the pellet was rinsed with warm injection buffer. The solution was resuspended in 0.2 mL cold BRB80 buffer. Subsequent spins were performed without the low pH cushion in an Airfuge, which reduces pelleting times. The final solution was converted to 1 \times BRB80 using 10 \times BRB80, flash frozen in 15 μ L aliquots, and stored at -80 $^{\circ}$ C.

5.5 GMPCPP-stabilized microtubule seeds

Guanylyl-(α,β)-methylene-diphosphonate stabilized (GMPCPP, NU-405S, Jena Bioscience, Jena, Germany), biotinylated microtubule seeds were prepared using a protocol based on a methods publication by *Gell et al.* (2010). A solution of 2 mg/mL tubulin containing 10% biotin-tubulin (Cytoskeleton, Inc., Denver, CO, USA) and up to 25% fluorescent tubulin was mixed with 1 mM GMPCPP and 1 mM MgCl₂, then briefly iced and polymerized at 37 $^{\circ}$ C for 30 minutes. The microtubules were centrifuged at 30 PSI for 5 minutes using an Airfuge (Beckman Coulter, Brea, CA), and the resulting pellet was rinsed with buffer and resuspended in a volume of buffer equal to 80% of the solution volume from the first incubation. The microtubules were then depolymerized on ice for 20 minutes, brought to 1 mM GMPCPP and 1 mM MgCl₂ (in addition to that already in the buffer), and incubated at 37 $^{\circ}$ C for 30 minutes. The re-polymerized microtubules were pelleted in the Airfuge as before, rinsed with buffer, and resuspended in a variable amount of buffer, typically 30% larger than the amount used for the first incubation. The seeds were flash frozen in small aliquots and stored at -80 $^{\circ}$ C.

5.6 Experimental sample chambers

Microtubules were grown in flow cells, which were constructed from treated cover slips (*Gell et al.*, 2010) and glass slides, separated by double-stick tape to create sample chambers of about 15 μL in volume. Vacuum grease was used to line the inner edges of the tape to prevent adhesive chemicals from contacting the sample. Samples were prepared via successive 5-minute incubations of (1) 0.01 mg/mL Neutravidin to adhere microtubule seeds to cover glass surface, (2) 0.1% Pluronic F127 to passivate the cover glass surface, (3) GMPCPP seeds, diluted 1000 \times from stock, and (4) an experimental solution containing buffer, 2 mM total MgCl_2 , 1 mM GTP, tubulin, and microtubule-binding drugs. Unlabeled and HiLyte 488 tubulin were mixed to achieve a labeling ratio of 20%. At each step several volumes of solution were flowed through the chamber, and prior to imaging the slide was sealed with VALAP (equal parts by mass of Vaseline, lanolin, and paraffin).

5.7 TIRF microscopy

Microtubule growth data was collected using total internal reflection fluorescence (TIRF) microscopy with a customized Zeiss (Carl Zeiss Microscopy, Jena, Germany) Axiovert 200M microscope. Briefly, a 491 nm excitation beam from a Cobalt (San Jose, CA, USA) Calypso laser was expanded, collimated, and ported into the epifluorescence path of the microscope using three mirrors for alignment. The beam was then focused on the back focal plane of a 100 \times 1.46 NA Zeiss Plan Apochromat objective and steered beyond the critical angle to produce shallow evanescent wave excitation of the samples. The microscope was equipped with a Semrock Di02-R488 dichroic beamsplitter and Chroma ET535/70m emission filter and was enclosed in a custom chamber that was heated to 37 $^\circ\text{C}$ using an AirTherm ATX (World Precision Instruments Inc., Sarasota, FL, USA). Experimental samples were allowed to thermally

equilibrate prior to data collection. Images were collected on a Hamamatsu (Hamamatsu Photonics K.K., Japan) C9100-13 EMCCD camera after additional $1.6\times$ optovar magnification ($160\times$ final magnification) and captured with HCImage software (Hamamatsu Photonics K.K.) using 30–240 ms exposures. Additional microscope details can be found in Chapter 2.

5.8 Growth data analysis

Microtubule end positions and backbone coordinates were estimated using TipTracker software as previously described (*Demchouk et al.*, 2011). Software was modified by adding code to allow a user to preselect microtubules and their approximate tip positions using one or more keyframes, which were interpolated to cover all frames. TipTracker code was changed to process inputs of (1) a single image frame and (2) approximate tip coordinates. In addition, the code was modified to run using Matlab's parallel processing feature, which increased the data analysis speed by approximately $8\times$ (8 parallel threads). Depending on the study, data frames were temporally averaged to 0.48–2 s prior to tip tracking.

Microtubule length versus time data for each treatment condition was processed using Matlab R2014a as follows. First, all microtubule length data was filtered using a running standard deviation window of 10 data points (20 s). Standard deviations greater than 200 nm, corresponding to inaccurate tracking of the microtubule end, were eliminated from analysis. Data removal was verified by simultaneously reviewing image data and length versus time data. Inaccurate tracking could often be attributed to diffusing fluorescent debris, poorly adhered microtubule seeds, or excessive diffusion of long microtubule tips out of the evanescent field. Then, periods of microtubule growth were manually selected and linear regression was performed on each to estimate the growth rate. At least two preparations were performed for each condition, and then the resulting growth rate values were averaged across all

microtubules for respective conditions. Diffusion-with-drift analysis was performed as described by *Gardner et al.* (2011a) and is detailed in Chapter 1.

CHAPTER VI

Conclusions and Future Work

Expanding on previously-established analysis methods, my work shows how therapeutic concentrations of tubulin-binding drugs affect microtubule dynamics. The disassembly-promoting drugs vinblastine and colchicine powerfully suppress the tubulin on and off rates, resulting in attenuation of the growth rate and dynamic instability. In contrast, the assembly-promoting drugs paclitaxel and peloruside A have only a marginal effect on the rate constants and growth rate, yet both are able to completely suppress dynamic instability at concentrations as low as 10 and 50 nM, respectively. In collaboration with the David Odde Lab (University of Minnesota), our combined data from *in vitro* and *in vivo* experiments, and from brownian dynamics simulations suggest that this occurs via an energetic convergence of the GDP-tubulin and GTP-tubulin states.

Even though studies of combined paclitaxel and peloruside failed to show any detectable synergistic effects, it is possible that they may stabilize microtubules at much lower concentrations than those tested. Because I only tested drug concentrations that would individually stabilize microtubules, it may be that much lower concentrations are sufficient to suppress dynamic instability. It is also likely that synergy between these drugs manifests as a shift in the tubulin critical concentration, which would not have been easily detectable in my experiments using pre-nucleated

microtubule seeds.

My recent results of microtubule tip structure analysis indicate that values of mean protofilament length are described by a gamma distribution with parameters similar to those found by *Gardner et al.* (2011b) for catastrophe times. My data also suggests that tip taper increases just prior to catastrophe events, which, in the context of work by *Gardner et al.* (2011a) indicates that the microtubule tip shifts to less stable configurations before undergoing rapid shortening. Further experimental studies of tip taper length and catastrophe times are needed to establish an unequivocal link.

Lastly, my experimental studies of Flutax-2 have shown that it aggregates in solution, leading to a much lower concentration of the monomeric form ($\sim 5\%$ at 100 nM total Flutax-2). This has implications for the interpretation of studies that have used Flutax-2, as it is unlikely that polymeric Flutax-2 can bind the paclitaxel site, and thus, the effective concentration is greatly reduced. Furthermore, I have shown that Flutax-2 interacts with the cover slip surface and self-quenches, leading to complex, non-monotonic fluorescence behavior. Now that these effects have been characterized, single-molecule microtubule-Flutax-2 kinetics can be accurately studied.

BIBLIOGRAPHY

BIBLIOGRAPHY

- Abal, M., A. A. Souto, F. Amat-Guerri, A. U. Acuña, J. M. Andreu, and I. Barasoain (2001), Centrosome and spindle pole microtubules are main targets of a fluorescent taxoid inducing cell death, *Cell motility and the cytoskeleton*, 49(1), 1–15.
- Al-Bassam, J., and F. Chang (2011), Regulation of microtubule dynamics by tog-domain proteins xmap215/dis1 and clasp, *Trends in cell biology*, 21(10), 604–614.
- Allen, R. D., N. S. Allen, and J. L. Travis (1981), Video-enhanced contrast, differential interference contrast (avec-dic) microscopy: A new method capable of analyzing microtubule-related motility in the reticulopodial network of *allogromia laticollaris*, *Cell motility*, 1(3), 291–302.
- Amador, M., J. Jimeno, L. Paz-Ares, H. Cortes-Funes, and M. Hidalgo (2003), Progress in the development and acquisition of anticancer agents from marine sources, *Annals of Oncology*, 14(11), 1607–1615.
- Amos, L. A., and J. Löwe (1999), How taxol® stabilises microtubule structure, *Chemistry & biology*, 6(3), R65–R69.
- Axelrod, D. (2001), Total internal reflection fluorescence microscopy in cell biology, *Traffic*, 2(11), 764–774.
- Axelrod, D., T. P. Burghardt, and N. L. Thompson (1984), Total internal reflection fluorescence, *Annual review of biophysics and bioengineering*, 13(1), 247–268.
- Balachandran, R., E. ter Haar, M. J. Welsh, S. G. Grant, and B. W. Day (1998), The potent microtubule-stabilizing agent (+)-discodermolide induces apoptosis in human breast carcinoma cells—preliminary comparisons to paclitaxel., *Anti-Cancer Drugs*, 9(1), 67–76.
- Banerjee, A., M. C. Roach, P. Trcka, and R. Luduena (1990), Increased microtubule assembly in bovine brain tubulin lacking the type iii isotype of beta-tubulin., *Journal of Biological Chemistry*, 265(3), 1794–1799.
- Bayley, P. M., M. J. Schilstra, and S. R. Martin (1990), Microtubule dynamic instability: numerical simulation of microtubule transition properties using a lateral cap model, *Journal of cell science*, 95(1), 33–48.

- Begaye, A., S. Trostel, Z. Zhao, R. E. Taylor, D. C. Schriemer, and D. L. Sackett (2011), Mutations in the β -tubulin binding site for peloruside confer resistance by targeting a cleft significant in side chain binding, *Cell Cycle*, 10(19), 3387–3396.
- Berrueta, L., S.-K. Kraeft, J. S. Tirnauer, S. C. Schuyler, L. B. Chen, D. E. Hill, D. Pellman, and B. E. Bierer (1998), The adenomatous polyposis coli-binding protein eb1 is associated with cytoplasmic and spindle microtubules, *Proceedings of the National Academy of Sciences*, 95(18), 10,596–10,601.
- Bicek, A. D., E. Tüzel, D. M. Kroll, and D. J. Odde (2007), Analysis of microtubule curvature, *Methods in cell biology*, 83, 237–268.
- Blagosklonny, M. V., and T. Fojo (1999), Molecular effects of paclitaxel: myths and reality (a critical review), *International Journal of Cancer*, 83(2), 151–156.
- Borst, P., and R. O. Elferink (2002), Mammalian abc transporters in health and disease, *Annual review of biochemistry*, 71(1), 537–592.
- Bowne-Anderson, H., M. Zanic, M. Kauer, and J. Howard (2013), Microtubule dynamic instability: a new model with coupled gtp hydrolysis and multistep catastrophe, *Bioessays*, 35(5), 452–461.
- Brouhard, G. J., J. H. Stear, T. L. Noetzel, J. Al-Bassam, K. Kinoshita, S. C. Harrison, J. Howard, and A. A. Hyman (2008), Xmap215 is a processive microtubule polymerase, *Cell*, 132(1), 79–88.
- Bruce Alberts, J. L. M. R. K. R., Alexander Johnson, and P. Walter (2002), *Molecular Biology of the Cell (4th edn)*, Garland Science.
- Budman, D. R., and A. Calabro (2002), In vitro search for synergy and antagonism: evaluation of docetaxel combinations in breast cancer cell lines, *Breast cancer research and treatment*, 74(1), 41–46.
- Buey, R. M., J. F. Diaz, J. M. Andreu, A. O’Brate, P. Giannakakou, K. Nicolaou, P. K. Sasmal, A. Ritzén, and K. Namoto (2004), Interaction of epothilone analogs with the paclitaxel binding site: relationship between binding affinity, microtubule stabilization, and cytotoxicity, *Chemistry & biology*, 11(2), 225–236.
- Caplow, M., and J. Shanks (1996), Evidence that a single monolayer tubulin-gtp cap is both necessary and sufficient to stabilize microtubules., *Molecular biology of the cell*, 7(4), 663–675.
- Carlomagno, T. (2009), *Tubulin-binding Agents: Synthetic, Structural and Mechanistic Insights*, vol. 286, Springer Science & Business Media.
- Carrero, G., D. McDonald, E. Crawford, G. de Vries, and M. J. Hendzel (2003), Using frap and mathematical modeling to determine the in vivo kinetics of nuclear proteins, *Methods*, 29(1), 14–28.

- Castle, B. T., and D. J. Odde (2013), Brownian dynamics of subunit addition-loss kinetics and thermodynamics in linear polymer self-assembly, *Biophysical journal*, *105*(11), 2528–2540.
- Castoldi, M., and A. V. Popov (2003), Purification of brain tubulin through two cycles of polymerization–depolymerization in a high-molarity buffer, *Protein expression and purification*, *32*(1), 83–88.
- Chou, T.-C., R. J. Motzer, Y. Tong, and G. J. Bosl (1994), Computerized quantitation of synergism and antagonism of taxol, topotecan, and cisplatin against human teratocarcinoma cell growth: a rational approach to clinical protocol design, *Journal of the National Cancer Institute*, *86*(20), 1517–1524.
- Chrétien, D., S. D. Fuller, and E. Karsenti (1995), Structure of growing microtubule ends: two-dimensional sheets close into tubes at variable rates., *The Journal of cell biology*, *129*(5), 1311–1328.
- Clark, E. A., P. M. Hills, B. S. Davidson, P. A. Wender, and S. L. Mooberry (2006), Laulimalide and synthetic laulimalide analogues are synergistic with paclitaxel and 2-methoxyestradiol, *Molecular pharmaceutics*, *3*(4), 457–467.
- Cooper Geoffrey, M. (2000), *The cell: A Molecular Approach*, ASM Press.
- Cormier, A., M. Marchand, R. B. Ravelli, M. Knossow, and B. Gigant (2008), Structural insight into the inhibition of tubulin by vinca domain peptide ligands, *EMBO reports*, *9*(11), 1101–1106.
- Cragg, G. M., and D. J. Newman (2005), Plants as a source of anti-cancer agents, *Journal of ethnopharmacology*, *100*(1), 72–79.
- Dave, R., D. S. Terry, J. B. Munro, and S. C. Blanchard (2009), Mitigating unwanted photophysical processes for improved single-molecule fluorescence imaging, *Biophysical journal*, *96*(6), 2371–2381.
- Demchouk, A. O., M. K. Gardner, and D. J. Odde (2011), Microtubule tip tracking and tip structures at the nanometer scale using digital fluorescence microscopy, *Cellular and molecular bioengineering*, *4*(2), 192–204.
- Derry, W. B., L. Wilson, and M. A. Jordan (1995), Substoichiometric binding of taxol suppresses microtubule dynamics, *Biochemistry*, *34*(7), 2203–2211.
- Derry, W. B., L. Wilson, I. A. Khan, R. F. Ludueña, and M. A. Jordan (1997), Taxol differentially modulates the dynamics of microtubules assembled from unfractionated and purified β -tubulin isotypes, *Biochemistry*, *36*(12), 3554–3562.
- Desai, A., and T. J. Mitchison (1997), Microtubule polymerization dynamics, *Annual review of cell and developmental biology*, *13*(1), 83–117.

- Díaz, J. F., R. Strobe, Y. Engelborghs, A. A. Souto, and J. M. Andreu (2000), Molecular recognition of taxol by microtubules kinetics and thermodynamics of binding of fluorescent taxol derivatives to an exposed site, *Journal of Biological Chemistry*, 275(34), 26,265–26,276.
- Dimitrov, A., M. Quesnoit, S. Moutel, I. Cantaloube, C. Poüs, and F. Perez (2008), Detection of gtp-tubulin conformation in vivo reveals a role for gtp remnants in microtubule rescues, *Science*, 322(5906), 1353–1356.
- Díaz, J. F., I. Barasoain, and J. M. Andreu (2003), Fast kinetics of taxol binding to microtubules effects of solution variables and microtubule-associated proteins, *Journal of Biological Chemistry*, 278(10), 8407–8419.
- Dowben, R. M., and J. W. Shay (2013), *Cell and muscle motility*, Springer Science & Business Media.
- Drechsel, D. N., and M. W. Kirschner (1994), The minimum gtp cap required to stabilize microtubules, *Current Biology*, 4(12), 1053–1061.
- Dumontet, C., and M. A. Jordan (2010), Microtubule-binding agents: a dynamic field of cancer therapeutics, *Nature reviews Drug discovery*, 9(10), 790–803.
- Dumontet, C., and B. I. Sikic (1999), Mechanisms of action of and resistance to antitubulin agents: microtubule dynamics, drug transport, and cell death, *Journal of Clinical Oncology*, 17(3), 1061–1061.
- Erickson, H. P. (1989), Co-operativity in protein-protein association: The structure and stability of the actin filament, *Journal of molecular biology*, 206(3), 465–474.
- Erickson, H. P., and E. T. O'Brien (1992), Microtubule dynamic instability and gtp hydrolysis, *Annual review of biophysics and biomolecular structure*, 21(1), 145–166.
- Foss, M., B. W. Wilcox, G. B. Alsop, and D. Zhang (2008), Taxol crystals can masquerade as stabilized microtubules, *PloS one*, 3(1), e1476.
- Gaitanos, T. N., R. M. Buey, J. F. Díaz, P. T. Northcote, P. Teesdale-Spittle, J. M. Andreu, and J. H. Miller (2004), Peloruside a does not bind to the taxoid site on β -tubulin and retains its activity in multidrug-resistant cell lines, *Cancer research*, 64(15), 5063–5067.
- Ganguly, A., F. Cabral, H. Yang, and K. D. Patel (2015), Peloruside a is a microtubule-stabilizing agent with exceptional anti-migratory properties in human endothelial cells, *Oncoscience*, 2(6), 585.
- Gapud, E. J., R. Bai, A. K. Ghosh, and E. Hamel (2004), Laulimalide and paclitaxel: a comparison of their effects on tubulin assembly and their synergistic action when present simultaneously, *Molecular pharmacology*, 66(1), 113–121.

- Gardner, M. K., B. D. Charlebois, I. M. Jánosi, J. Howard, A. J. Hunt, and D. J. Odde (2011a), Rapid microtubule self-assembly kinetics, *Cell*, *146*(4), 582–592.
- Gardner, M. K., M. Zanic, C. Gell, V. Bormuth, and J. Howard (2011b), Depolymerizing kinesins kip3 and mcak shape cellular microtubule architecture by differential control of catastrophe, *Cell*, *147*(5), 1092–1103.
- Gell, C., et al. (2010), Microtubule dynamics reconstituted in vitro and imaged by single-molecule fluorescence microscopy, *Methods in cell biology*, *95*, 221–245.
- Giannakakou, P., et al. (2000), A common pharmacophore for epothilone and taxanes: molecular basis for drug resistance conferred by tubulin mutations in human cancer cells, *Proceedings of the National Academy of Sciences*, *97*(6), 2904–2909.
- Gillespie, D. T., and E. Seitaridou (2012), *Simple Brownian diffusion: an introduction to the standard theoretical models*, OUP Oxford.
- Gittes, F., B. Mickey, J. Nettleton, and J. Howard (1993), Flexural rigidity of microtubules and actin filaments measured from thermal fluctuations in shape., *The Journal of cell biology*, *120*(4), 923–934.
- Goehring, N. W., D. Chowdhury, A. A. Hyman, and S. W. Grill (2010), Frap analysis of membrane-associated proteins: lateral diffusion and membrane-cytoplasmic exchange, *Biophysical journal*, *99*(8), 2443–2452.
- Gregoretto, I. V., G. Margolin, M. S. Alber, and H. V. Goodson (2006), Insights into cytoskeletal behavior from computational modeling of dynamic microtubules in a cell-like environment, *J Cell Sci*, *119*(22), 4781–4788.
- Gupta, M. L., C. J. Bode, G. I. Georg, and R. H. Himes (2003), Understanding tubulin–taxol interactions: mutations that impart taxol binding to yeast tubulin, *Proceedings of the National Academy of Sciences*, *100*(11), 6394–6397.
- Hamel, E. (1992), Natural products which interact with tubulin in the vinca domain: maytansine, rhizoxin, phomopsin a, dolastatins 10 and 15 and halichondrin b, *Pharmacology & therapeutics*, *55*(1), 31–51.
- Hamel, E., et al. (2006), Synergistic effects of peloruside a and laulimalide with taxoid site drugs, but not with each other, on tubulin assembly, *Molecular pharmacology*, *70*(5), 1555–1564.
- Hammond, G. R., Y. Sim, L. Lagnado, and R. F. Irvine (2009), Reversible binding and rapid diffusion of proteins in complex with inositol lipids serves to coordinate free movement with spatial information, *The Journal of cell biology*, *184*(2), 297–308.
- Hawkins, T., M. Mirigian, M. S. Yasar, and J. L. Ross (2010), Mechanics of microtubules, *Journal of biomechanics*, *43*(1), 23–30.

- Hill, T. L. (1987), Attached single-stranded polymer, in *Linear Aggregation Theory in Cell Biology*, pp. 32–77, Springer.
- Hood, K. A., L. M. West, B. Rouwé, P. T. Northcote, M. V. Berridge, J. H. Miller, et al. (2002), Peloruside a, a novel antimitotic agent with paclitaxel-like microtubule-stabilizing activity, *Cancer research*, 62(12), 3356–3360.
- Horwitz, S. B., D. Cohen, S. Rao, I. Ringel, H.-J. Shen, and C. Yang (1992), Taxol: mechanisms of action and resistance., *Journal of the National Cancer Institute. Monographs*, (15), 55–61.
- Howard, J., et al. (2001), Mechanics of motor proteins and the cytoskeleton.
- Howarth, F., S. Calaghan, M. Boyett, and E. White (1999), Effect of the microtubule polymerizing agent taxol on contraction, ca²⁺ transient and l-type ca²⁺ current in rat ventricular myocytes, *The Journal of Physiology*, 516(2), 409–419.
- Huzil, J. T., J. K. Chik, G. W. Slysz, H. Freedman, J. Tuszynski, R. E. Taylor, D. L. Sackett, and D. C. Schriemer (2008), A unique mode of microtubule stabilization induced by peloruside a, *Journal of molecular biology*, 378(5), 1016–1030.
- Hyman, A. A., S. Salser, D. Drechsel, N. Unwin, and T. J. Mitchison (1992), Role of gtp hydrolysis in microtubule dynamics: information from a slowly hydrolyzable analogue, gmpcpp., *Molecular biology of the cell*, 3(10), 1155–1167.
- Hyman, A. A., D. Chrétien, I. Arnal, and R. H. Wade (1995), Structural changes accompanying gtp hydrolysis in microtubules: information from a slowly hydrolyzable analogue guanylyl-(alpha, beta)-methylene-diphosphonate., *The Journal of cell biology*, 128(1), 117–125.
- Irick, S. C. (1984), An automated beam measurement system, in *28th Annual Technical Symposium*, pp. 204–211, International Society for Optics and Photonics.
- Ishikawa-Ankerhold, H. C., R. Ankerhold, and G. P. Drummen (2012), Advanced fluorescence microscopy techniques: frap, flip, flap, fret and flim, *Molecules*, 17(4), 4047–4132.
- Janson, M. E., and M. Dogterom (2004), A bending mode analysis for growing microtubules: evidence for a velocity-dependent rigidity, *Biophysical journal*, 87(4), 2723–2736.
- Jordan, M. A., and L. Wilson (2004), Microtubules as a target for anticancer drugs, *Nature Reviews Cancer*, 4(4), 253–265.
- Jordan, M. A., D. Thrower, and L. Wilson (1991), Mechanism of inhibition of cell proliferation by vinca alkaloids, *Cancer research*, 51(8), 2212–2222.
- Jordan, M. A., R. J. Toso, D. Thrower, and L. Wilson (1993), Mechanism of mitotic block and inhibition of cell proliferation by taxol at low concentrations, *Proceedings of the National Academy of Sciences*, 90(20), 9552–9556.

- Jordan, M. A., K. Wendell, S. Gardiner, W. B. Derry, H. Copp, and L. Wilson (1996), Mitotic block induced in hela cells by low concentrations of paclitaxel (taxol) results in abnormal mitotic exit and apoptotic cell death, *Cancer research*, 56(4), 816–825.
- Julien, B., and S. Shah (2002), Heterologous expression of epothilone biosynthetic genes in myxococcus xanthus, *Antimicrobial agents and chemotherapy*, 46(9), 2772–2778.
- Kanakkanthara, A., et al. (2011), Peloruside-and laulimalide-resistant human ovarian carcinoma cells have β i-tubulin mutations and altered expression of β ii-and β iii-tubulin isotypes, *Molecular cancer therapeutics*, 10(8), 1419–1429.
- Kavallaris, M., D. Kuo, C. A. Burkhart, D. L. Regl, M. D. Norris, M. Haber, and S. B. Horwitz (1997), Taxol-resistant epithelial ovarian tumors are associated with altered expression of specific beta-tubulin isotypes., *Journal of Clinical Investigation*, 100(5), 1282.
- Kerssemakers, J. W., E. L. Munteanu, L. Laan, T. L. Noetzel, M. E. Janson, and M. Dogterom (2006), Assembly dynamics of microtubules at molecular resolution, *Nature*, 442(7103), 709–712.
- Khrapunovich-Baine, M., V. Menon, C.-P. H. Yang, P. T. Northcote, J. H. Miller, R. H. Angeletti, A. Fiser, S. B. Horwitz, and H. Xiao (2011), Hallmarks of molecular action of microtubule stabilizing agents effects of epothilone b, ixabepilone, peloruside a, and laulimalide on microtubule conformation, *Journal of Biological Chemistry*, 286(13), 11,765–11,778.
- Kreis, T., and R. Vale (1993), Guidebook to the cytoskeletal and motor proteins.
- Krouglova, T., J. Vercaammen, and Y. Engelborghs (2004), Correct diffusion coefficients of proteins in fluorescence correlation spectroscopy. application to tubulin oligomers induced by mg 2+ and paclitaxel, *Biophysical journal*, 87(4), 2635–2646.
- Kumarasinghe, M., S. Constantine, and R. Hemamali (1997), Methanol as an alternative fixative for cytological smears., *The Malaysian journal of pathology*, 19(2), 137–140.
- Lakämper, S., and E. Meyhöfer (2005), The e-hook of tubulin interacts with kinesins head to increase processivity and speed, *Biophysical journal*, 89(5), 3223–3234.
- Lu, Q., and R. F. Luduena (1993), Removal of beta-iii isotype enhances taxol induced microtubule assembly., *Cell structure and function*, 18(3), 173–182.
- Lu, Y., J. Chen, M. Xiao, W. Li, and D. D. Miller (2012), An overview of tubulin inhibitors that interact with the colchicine binding site, *Pharmaceutical research*, 29(11), 2943–2971.

- Madari, H., D. Panda, L. Wilson, and R. S. Jacobs (2003), Dicoumarol a unique microtubule stabilizing natural product that is synergistic with taxol, *Cancer research*, *63*(6), 1214–1220.
- Mandelkow, E.-M., E. Mandelkow, and R. A. Milligan (1991), Microtubule dynamics and microtubule caps: a time-resolved cryo-electron microscopy study., *The Journal of cell biology*, *114*(5), 977–991.
- Margolis, R. L., and L. Wilson (1977), Addition of colchicine-tubulin complex to microtubule ends: the mechanism of substoichiometric colchicine poisoning, *Proceedings of the National Academy of Sciences*, *74*(8), 3466–3470.
- Martello, L. A., et al. (2000), Taxol and discodermolide represent a synergistic drug combination in human carcinoma cell lines, *Clinical Cancer Research*, *6*(5), 1978–1987.
- Martin, S., M. Schilstra, and P. Bayley (1993), Dynamic instability of microtubules: Monte carlo simulation and application to different types of microtubule lattice., *Biophysical journal*, *65*(2), 578.
- Maurer, S. P., F. J. Fourniol, G. Bohner, C. A. Moores, and T. Surrey (2012), Ebs recognize a nucleotide-dependent structural cap at growing microtubule ends, *Cell*, *149*(2), 371–382.
- May, K. M., and K. G. Hardwick (2006), The spindle checkpoint, *Journal of cell science*, *119*(20), 4139–4142.
- Memoli, A., L. G. Palermiti, V. Travagli, and F. Alhaique (1999), Effects of surfactants on the spectral behaviour of calcein (ii): a method of evaluation, *Journal of pharmaceutical and biomedical analysis*, *19*(3), 627–632.
- Miller, J. H., A. Wilmes, K. Bargh, C. Kelly, and P. T. Northcote (2006), Peloruside a and paclitaxel synergize in their cytotoxic and microtubule-stabilizing effects in cultured cancer cell lines, *Cancer Research*, *66*(8 Supplement), 907–907.
- Miller, J. H., A. J. Singh, and P. T. Northcote (2010), Microtubule-stabilizing drugs from marine sponges: focus on peloruside a and zampanolide, *Marine drugs*, *8*(4), 1059–1079.
- Mitchison, T., and M. Kirschner (1984), Dynamic instability of microtubule growth, *nature*, *312*(5991), 237–242.
- Mitra, A., and D. Sept (2004), Localization of the antimitotic peptide and depsipeptide binding site on β -tubulin, *Biochemistry*, *43*(44), 13,955–13,962.
- Mohan, R., E. A. Katrukha, H. Doodhi, I. Smal, E. Meijering, L. C. Kapitein, M. O. Steinmetz, and A. Akhmanova (2013), End-binding proteins sensitize microtubules to the action of microtubule-targeting agents, *Proceedings of the National Academy of Sciences*, *110*(22), 8900–8905.

- Mollinedo, F., and C. Gajate (2003), Microtubules, microtubule-interfering agents and apoptosis, *Apoptosis*, 8(5), 413–450.
- Mu, F., L. Yang, W. Wang, M. Luo, Y. Fu, X. Guo, and Y. Zu (2012), Negative-pressure cavitation extraction of four main vinca alkaloids from *catharanthus roseus* leaves, *Molecules*, 17(8), 8742–8752.
- Newport (2016), Gaussian beam optics.
- Ngan, V. K., K. Bellman, B. T. Hill, L. Wilson, and M. A. Jordan (2001), Mechanism of mitotic block and inhibition of cell proliferation by the semisynthetic vinca alkaloids vinorelbine and its newer derivative vinflunine, *Molecular pharmacology*, 60(1), 225–232.
- Nogales, E., and H.-W. Wang (2006), Structural intermediates in microtubule assembly and disassembly: how and why?, *Current opinion in cell biology*, 18(2), 179–184.
- Nogales, E., S. G. Wolf, and K. H. Downing (1998), Structure of the $\alpha\beta$ tubulin dimer by electron crystallography, *Nature*, 391(6663), 199–203.
- Northrup, S. H., and H. P. Erickson (1992), Kinetics of protein-protein association explained by brownian dynamics computer simulation., *Proceedings of the National Academy of Sciences*, 89(8), 3338–3342.
- Odde, D. J., L. Cassimeris, and H. M. Buettner (1995), Kinetics of microtubule catastrophe assessed by probabilistic analysis., *Biophysical journal*, 69(3), 796.
- Oosawa, F. (1970), Size distribution of protein polymers, *Journal of theoretical biology*, 27(1), 69–86.
- Oosawa, F., S. Asakura, et al. (1975), *Thermodynamics of the Polymerization of Protein*, Academic Press.
- Orr, G. A., P. Verdier-Pinard, H. McDaid, and S. B. Horwitz (2003), Mechanisms of taxol resistance related to microtubules, *Oncogene*, 22(47), 7280–7295.
- Pampaloni, F., G. Lattanzi, A. Jonáš, T. Surrey, E. Frey, and E.-L. Florin (2006), Thermal fluctuations of grafted microtubules provide evidence of a length-dependent persistence length, *Proceedings of the National Academy of Sciences*, 103(27), 10,248–10,253.
- Panda, D., H. P. Miller, A. Banerjee, R. F. Luduena, and L. Wilson (1994), Microtubule dynamics in vitro are regulated by the tubulin isotype composition, *Proceedings of the National Academy of Sciences*, 91(24), 11,358–11,362.
- Panda, D., M. A. Jordan, K. C. Chu, and L. Wilson (1996), Differential effects of vinblastine on polymerization and dynamics at opposite microtubule ends, *Journal of Biological Chemistry*, 271(47), 29,807–29,812.

- Peng, L. X., M. T. Hsu, M. Bonomi, D. A. Agard, and M. P. Jacobson (2014), The free energy profile of tubulin straight-bent conformational changes, with implications for microtubule assembly and drug discovery, *PLoS Comput Biol*, *10*(2), e1003464.
- Pollard, T. D. (1986), Rate constants for the reactions of atp-and adp-actin with the ends of actin filaments., *The Journal of cell biology*, *103*(6), 2747–2754.
- Prota, A. E., K. Bargsten, P. T. Northcote, M. Marsh, K.-H. Altmann, J. H. Miller, J. F. Díaz, and M. O. Steinmetz (2014), Structural basis of microtubule stabilization by laulimalide and peloruside a, *Angewandte Chemie International Edition*, *53*(6), 1621–1625.
- Ranganathan, S., C. Benetatos, P. Colarusso, D. Dexter, and G. Hudes (1998), Altered beta-tubulin isotype expression in paclitaxel-resistant human prostate carcinoma cells., *British journal of cancer*, *77*(4), 562.
- Ravelli, R. B., B. Gigant, P. A. Curmi, I. Jourdain, S. Lachkar, A. Sobel, and M. Knosow (2004), Insight into tubulin regulation from a complex with colchicine and a stathmin-like domain, *Nature*, *428*(6979), 198–202.
- Rowinsky, E. K., L. A. Cazenave, and R. C. Donehower (1990), Taxol: a novel investigational antimicrotubule agent, *Journal of the National Cancer Institute*, *82*(15), 1247–1259.
- Rowinsky, E. K., N. Onetto, R. M. Canetta, and S. G. Arbuck (1992), Taxol: the first of the taxanes, an important new class of antitumor agents., in *Seminars in oncology*, vol. 19, pp. 646–662.
- Ruhnow, F., D. Zwicker, and S. Diez (2011), Tracking single particles and elongated filaments with nanometer precision, *Biophysical journal*, *100*(11), 2820–2828.
- Sackett, D. L., and D. Sept (2009), Protein–protein interactions: making drug design second nature, *Nature chemistry*, *1*(8), 596–597.
- Schek, H. T., M. K. Gardner, J. Cheng, D. J. Odde, and A. J. Hunt (2007), Microtubule assembly dynamics at the nanoscale, *Current Biology*, *17*(17), 1445–1455.
- Seetapun, D., B. T. Castle, A. J. McIntyre, P. T. Tran, and D. J. Odde (2012), Estimating the microtubule gtp cap size in vivo, *Current Biology*, *22*(18), 1681–1687.
- Serdyuk, I. N., N. R. Zaccai, and J. Zaccai (2007), *Methods in molecular biophysics: structure, dynamics, function*, Cambridge University Press.
- Shen, Y.-N., L. Lin, H.-Y. Qiu, W.-Y. Zou, Y. Qian, and H.-L. Zhu (2015), The design, synthesis, in vitro biological evaluation and molecular modeling of novel benzenesulfonate derivatives bearing chalcone moieties as potent anti-microtubulin polymerization agents, *RSC Advances*, *5*(30).

- Skellam, J. G. (1945), The frequency distribution of the difference between two poisson variates belonging to different populations., *Journal of the Royal Statistical Society. Series A (General)*, 109(Pt 3), 296–296.
- Tim Mitchison Lab, H. U. (2016), Labeling tubulin and quantifying labeling stoichiometry.
- Torres, K., and S. B. Horwitz (1998), Mechanisms of taxol-induced cell death are concentration dependent, *Cancer research*, 58(16), 3620–3626.
- Tran, P., R. Walker, and E. Salmon (1997), A metastable intermediate state of microtubule dynamic instability that differs significantly between plus and minus ends, *The Journal of cell biology*, 138(1), 105–117.
- VanBuren, V., D. J. Odde, and L. Cassimeris (2002), Estimates of lateral and longitudinal bond energies within the microtubule lattice, *Proceedings of the National Academy of Sciences*, 99(9), 6035–6040.
- Vandecandelaere, A., S. R. Martin, and Y. Engelborghs (1997), Response of microtubules to the addition of colchicine and tubulin–colchicine: evaluation of models for the interaction of drugs with microtubules, *Biochemical journal*, 323(1), 189–196.
- Voter, W. A., E. T. O’Brien, and H. P. Erickson (1991), Dilution-induced disassembly of microtubules: Relation to dynamic instability and the gtp cap, *Cell motility and the cytoskeleton*, 18(1), 55–62.
- Walczak, C. E., S. Cai, and A. Khodjakov (2010), Mechanisms of chromosome behaviour during mitosis, *Nature Reviews Molecular Cell Biology*, 11(2), 91–102.
- Walker, R., E. T. O’Brien, N. Pryer, M. Soboeiro, W. Voter, H. P. Erickson, and E. D. Salmon (1988), Dynamic instability of individual microtubules analyzed by video light microscopy: rate constants and transition frequencies., *The Journal of cell biology*, 107(4), 1437–1448.
- Walker, R., S. Inoué, and E. D. Salmon (1989), Asymmetric behavior of severed microtubule ends after ultraviolet-microbeam irradiation of individual microtubules in vitro., *The Journal of cell biology*, 108(3), 931–937.
- Walker, R., N. Pryer, and E. D. Salmon (1991), Dilution of individual microtubules observed in real time in vitro: evidence that cap size is small and independent of elongation rate., *The Journal of cell biology*, 114(1), 73–81.
- Wang, Y., et al. (2016), Structures of a diverse set of colchicine binding site inhibitors in complex with tubulin provide a rationale for drug discovery, *FEBS Journal*, 283(1), 102–111.
- Weiss, W., F. Weiland, and A. Görg (2009), Protein detection and quantitation technologies for gel-based proteome analysis, in *Proteomics*, pp. 59–82, Springer.

- Wiggins, C. H., D. Riveline, A. Ott, and R. E. Goldstein (1998), Trapping and wiggling: elastohydrodynamics of driven microfilaments, *Biophysical Journal*, *74*(2), 1043–1060.
- Wilmes, A., K. Bargh, C. Kelly, P. T. Northcote, and J. H. Miller (2007), Peloruside synergizes with other microtubule stabilizing agents in cultured cancer cell lines, *Molecular pharmacology*, *4*(2), 269–280.
- Wilmes, A., D. OSullivan, A. Chan, C. Chandrasekhar, I. Paterson, P. T. Northcote, A. C. La Flamme, and J. H. Miller (2011), Synergistic interactions between peloruside and other microtubule-stabilizing and destabilizing agents in cultured human ovarian carcinoma cells and murine t cells, *Cancer chemotherapy and pharmacology*, *68*(1), 117–126.
- Wilson, L., M. Jordan, A. Morse, and R. Margolis (1982), Interaction of vinblastine with steady-state microtubules in vitro, *Journal of molecular biology*, *159*(1), 125–149.
- Yvon, A.-M. C., P. Wadsworth, and M. A. Jordan (1999), Taxol suppresses dynamics of individual microtubules in living human tumor cells, *Molecular biology of the cell*, *10*(4), 947–959.
- Zanic, M., J. H. Stear, A. A. Hyman, and J. Howard (2009), Ebf1 recognizes the nucleotide state of tubulin in the microtubule lattice, *PloS one*, *4*(10), e7585.
- Zanic, M., P. O. Widlund, A. A. Hyman, and J. Howard (2013), Synergy between xmap215 and ebf1 increases microtubule growth rates to physiological levels, *Nature cell biology*, *15*(6), 688–693.
- Zhang, B., J. Zerubia, and J.-C. Olivo-Marin (2007), Gaussian approximations of fluorescence microscope point-spread function models, *Applied Optics*, *46*(10), 1819–1829.
- Zhou, J. (2007), *Microtubule protocols*, vol. 137, Springer Science & Business Media.